UNIVERSITY OF HAMBURG
DEPARTMENT OF PHYSICS

Resonant Hard X-ray Ptychography for High-Sensitivity Imaging with Chemical Contrast

Dissertation

zur Erlangung des Doktorgrades

an der Fakultät für Mathematik, Informatik und Naturwissenschaften
Fachbereich Physik
der Universität Hamburg

vorgelegt von
JULIANE REINHARDT

aus Sondershausen

Hamburg
2017

The work described in this thesis was done at the Photon Science division of Deutsches Elektronen-Synchrotron, a Research Centre of the Helmholtz Association.

Gutachter/in der Dissertation:	Prof. Dr. C. G. Schroer Prof. Dr. A. Stierle
Gutachter/in der Disputation:	Prof. Dr. D. Pfannkuche Prof. Dr. C. G. Schroer Prof. Dr. A. Stierle Prof. Dr. W. Wurth Prof. Dr. G. Gruebel
Datum der Disputation:	03.04.2017
Dekan des Fachbereichs Physik:	Prof. Dr. H. Graener

Die Naturwissenschaft beschreibt und erklärt die Natur nicht einfach, so wie sie "an sich" ist. Sie ist vielmehr ein Teil des Wechselspiels zwischen der Natur und uns selbst.

What we observe is not nature in itself but nature exposed to our method of questioning.

Werner Heisenberg

Zusammenfassung

Um detaillierte Kenntnisse über biologische, chemische oder physikalische Prozesse zu gewinnen, sind hochauflösende Bildgebungstechniken unverzichtbar. Hierfür hat sich in den letzten Jahren die kohärente Bildgebungsmethode Ptychography mit Röntgenstrahlung etabliert. Röntgenstrahlung zeichnet sich durch eine hohe Eindringtiefe in Materie aus, was die Untersuchung verschiedenartiger Proben in chemischen Reaktoren erlaubt. Darüberhinaus ist es möglich die Röntgenptychographie mit resonanter Streuung zu kombinieren und somit Informationen über verschiedene Elemente oder sogar über verschiedene Oxidationszustände in heterogenen Proben zu erhalten.

Im Prinzip ist die erreichbare Ortsauflösung und die Detektionsempfindlichkeit der ptychographischen Bildgebung durch die höchsten Streuwinkel, in denen noch verlässlich ein Streusignal der Probe gemessen werden kann sowie durch die Stabilität des Mikroskopes limitiert. Allerdings erfordert die erfolgreiche Nutzung von resonanter Ptychographie zur quantitativen Bildgebung nicht nur eine hohe Ortsauflösung, sondern ebenfalls einen zuverlässigen Phasenrekonstruktionsalgorithmus. Durch diesen sollen konsistente und reproduzierbare Rekonstruktionen der Objektfunktion der Proben gewährleistet werden.

Beginnend mit einer stark streuenden Standardprobe, über eine schwach streuende Modellprobe bis hin zu einer realistischen Probe wurde in dieser Arbeit eine genaue Analyse der Rekonstruktionsergebnisse durchgeführt. Durch diese hierarchische Vorgehensweise wurden Unzulänglichkeiten des ptychographischen Modells erkannt und durch zusätzliche Einschränkungen und Erweiterungen des Phasenrekonstruktionsalgorithmuses behoben. Zusätzlich wurde sowohl die Detektionsempfindlichkeit für kleine Probenstrukturen als auch die Ortsauflösung durch den Einsatz eines undurchlässigen Strahlabsorbers zur Reduktion des parasitären Streuhintergrundes verbessert. Um die Richtigkeit der Rekonstruktionswerte sicherzustellen, ist eine Doppelbelichtung erforderlich.

All diese Schritte ermöglichten schlussendlich die Untersuchung der chemischen Verteilung einer Katalysatormodellprobe sowie einer Platinschicht, wie sie auch in Sauerstoffsensoren verwendet werden kann.

Abstract

For the detailed investigation of biological, chemical or physical processes on the nano scale, high-resolution imaging techniques are essential. For this purpose, the coherent imaging technique – X-ray ptychography – has been established in recent years. X-rays are particularly suitable due to their high penetration depth in matter which allows for a broad range of applications such as the investigation of samples in chemical reactors. Moreover, X-ray ptychography combined with resonant scattering provides chemical contrast to determine different elements or even different oxidation states in heterogeneous specimens.

In general, the spatial resolution and the sensitivity in ptychographic imaging are limited by the signal that is detected over noise and over background scattering in high scattering angles as well as by the stability of the microscope. However, establishing resonant hard X-ray ptychography as a tool for quantitative imaging requires not only high-resolution images but also a reliable phase retrieval process. This in turn, results in a consistent and reproducible reconstruction of the object function of the samples.

In this work, a detailed analysis of the reconstructions was accomplished, starting from a well-known and strongly scattering resolution chart to a weakly scattering model sample and finally to a real sample. With this hierarchical procedure, shortcomings of the ptychographic model were identified and compensated by setting additional constraints and extensions to the phase retrieval algorithm. Furthermore, both the sensitivity to small features as well as the spatial resolution were improved by using an opaque beamstop to suppress parasitic background scattering. In order to maintain the integrity of the values (quantitativeness) in the reconstruction, a double exposure scheme is necessary.

These steps provided the basis for the analysis of the chemical distribution of a catalyst model sample as well as of a platinum layer as it can be used in an oxygen sensor.

Contents

Introduction

Steady technological progress enjoyed in modern society stands on invention, innovation and improvement of techniques, materials and devices. These advancements demand a deep insight into the structure of nanomaterials and their function during biological, chemical and physical processes. To gain such insight, microscopy techniques have been applied to investigate all kinds of matter for many centuries, Abbe [1873]. Today, the pioneering work by Hell [2003] yields stunning results in visible light microscopy reaching a spatial resolution beyond the diffraction limit, Klar et al. [2000]. A further branch of high-resolution microscopy is electron microscopy which provides the utmost spatial resolution, Kisielowski et al. [2008]. However, this comes at the cost of extensive sample preparation and restrictions to the sample environment. From a materials science point of view, it is especially important to investigate catalysts, solar cells, batteries and many more devices that are relevant to our everyday life under realistic conditions and without destructive sample preparation. Driven by these needs, electron microscopy has been further developed and can nowadays offer environmental investigation with an image resolution on the atomic scale, Yoshida et al. [2012], Hansen and Wagner [2015]. Nevertheless, the strong electron-electron interaction leading to high contrast and outstanding high spatial resolution, at the same time limits the penetration depth and concomitantly the possibility to image bulk material above a certain thickness. In contrast, X-rays, in particular hard X-rays, seem perfectly suited for this purpose due to their high penetration depth that allows for reactor cells in ambient or high-pressure conditions as well as for minimal sample preparation, Thomas and Hernandez-Garrido [2009].

In recent years, various X-ray techniques have matured and become indispensable tools for materials science. Long-established techniques such as X-ray absorption spectroscopy (EXAFS, XANES), Lee et al. [1981], or small and wide angle scattering (SAXS and WAXS), Hura et al. [2009], provide insight into the electronic, atomic and molecular structure of matter via calculations based on the intensity changes as a function of energy or as a function of the scattering angle. Beside these techniques, dedicated imaging techniques – either in full-field or scanning mode – are becoming more and more important as individual features in sample structures play a key role and must be visualised.

With the improvement of nano-focusing X-ray optics, Snigirev et al. [1996], Jefimovs et al. [2007], Mimura et al. [2010], Huang et al. [2013], direct X-ray imaging reaches high spatial resolution on the nanometer scale and is applicable to different contrasts such as fluorescence or absorption. Since these optics are difficult to build and pose other challenges to the experimental setup, lensless diffractive imaging is on the rise.

About 20 years ago, lensless coherent diffractive imaging (CDI) achieved the first images of non-crystalline objects with a spatial resolution better than $100\,\mathrm{nm}$, Miao et al. [1999], by reconstructing the object from the intensity distribution of a diffraction pattern. Since

then, CDI has been continuously improved and applied to biology, chemistry and materials science, Barty et al. [2008], Bogan et al. [2008], Takayama and Yonekura [2016]. One drawback of single shot CDI is that the sample size is limited by the size of the illuminating beam. This issue can be solved by a scanning technique. So, some years later, a technique already known from electron microscopy and described first by Hegerl and Hoppe [1970] – ptychography – found its new application in the X-ray regime. With this, the sample size was no longer limited by the illuminating beam size. Further development of the phase retrieval algorithm also affords a reconstruction of the illuminating probe without prior knowledge or the need of constraints to the object. In the beginning of the millennium, different groups such as Faulkner and Rodenburg [2004] or Thibault et al. [2008], proposed different advanced reconstruction algorithms that can be seen as the kick-off for using ptychography in various experiments.

Since then, ptychography has been established in the synchrotron community for different applications, e.g., Giewekemeyer et al. [2010], Jones et al. [2014], Baier et al. [2016] or Donnelly et al. [2016]. High spatial resolution in the range of 50 nm to 100 nm is achieved more or less routinely. Recently, ptychography has also been combined with other techniques such as fluorescence, Deng et al. [2015], and so-called multi-modal imaging is becoming more important.

Chemical imaging using spectroscopy techniques such as XANES or fluorescence has a long history. However, in their conventional form, the spatial resolution is either limited by the effective pixel size of the detector or by the beam size, both of which are influenced by the focusing properties of X-ray optics. Today, the combination of the lensless imaging technique, ptychography, with resonant scattering tries to overcome these limits in spatial resolution. For resonant ptychography, a series of ptychograms at different energies around an absorption edge of an element of interest is recorded. In this way, the near-edge structure information in terms of absorption and phase shift can be extracted with the same high spatial resolution as seen in the ptychographic reconstruction. The first proof of principle of resonant ptychography achieving chemical contrast was published by Beckers et al. [2011] in the soft X-ray regime. Shortly after, an own contribution Hoppe et al. [2013] presented a proof of principle in the hard X-ray regime. By now, an increasing number of experiments have been performed utilizing resonant ptychography for chemical imaging, e.g., Shapiro et al. [2014], Donnelly et al. [2015].

The common use of ptychography in so many fields of research might deceive one into thinking that the technique is already fully understood and under control for all kinds of experimental conditions. However, this is only the case for some defined circumstances. Whereas a spatial resolution of less than 10 nm has been reported for strongly scattering samples, also in the hard X-ray regime Schropp et al. [2012], imaging of weak objects is still challenging, Dierolf et al. [2010]. Especially when pushing the limits, Schropp and Schroer [2010], in terms of spatial resolution and the sensitivity to weakly scattering samples, the reliability of ptychographic reconstruction is still to be carefully proven. As small features and nano structures have moved into the focus of research, the use of ptychography transforms from a merely imaging technique to a tool for complex material analysis, especially for nanomaterials. Not only high spatial resolution is required but also high sensitivity and reliable quantitative results. However, only little attention has been paid

to artefacts and the reliability of ptychographic results in terms of positioning errors Maiden et al. [2012], Zhang et al. [2013] and even less to background scattering effects.

With respect to these often disregarded artefacts, the final aim of this work is to achieve quantitative chemical contrast with high spatial resolution and with high sensitivity. The dissertation is structured into a brief theoretical part, where the basic physical processes such as the interaction of X-rays with matter are explained. In Chapter 2 and 3, the methods as well as the experimental components and procedures relevant for the later analysis are summarised. The experiments of this work were performed at the beamline P06 at the PETRA III synchrotron light source at DESY in Hamburg, Germany. The main contribution of this work lies in the detailed evaluation of the ptychographic data sets given in Chapter 4. Here, the opportunities and limitations of hard X-ray ptychography for the imaging of weakly scattering features are addressed and the reliability of the ptychographic reconstructions of different samples is critically reviewed. In a next step, the background scattering which diminishes the data quality is treated by implementing an opaque beamstop into the experimental setup. To ensure the quantitativeness of the reconstruction process, a dual-exposure scheme together with the simultaneous ptychographic reconstruction of two data sets – one with and one without beamstop – is introduced, Reinhardt et al. [2017]. Before the resonant ptychography measurements finally result in the chemical analysis of a catalyst model sample and a platinum bubble, further effort was put into the correction of positioning errors and the image alignment. In the conclusions in Chapter 5, the main findings and ideas for future work will be discussed.

1 Theory

In this thesis, the essential information about the samples was obtained from diffraction patterns collected in the far field under certain experimental conditions. The intensity distribution in these diffraction patterns originates from the interaction of partially coherent X-ray photons with matter. In order to interpret the diffraction data correctly, a broad knowledge about the interaction processes is required. Therefore, in this chapter, the mathematical and physical description of the interaction process of photons with atoms will be presented leading to the definition of the atomic form factor in Section 1.1.2 and furthermore to the complex refractive index including absorption and phase shift effects in Section 1.1.4. The description is based on the textbooks by Hecht [2002], Als-Nielsen and McMorrow [2011] and Attwood [2007].

As a coherent scattering techniques was applied, the basic principle of coherence is given in Section 1.2 together with a short introduction of incoherent scattering which is relevant for background scattering effects under real experimental conditions. In order to finally handle the actually applied imaging technique, ptychography cf. Section 2.1, a mathematical formulation of wave propagation and FOURIER space is given in Section 1.3.

1.1 Interaction of X-rays with matter

In the electromagnetic spectrum, radiation in the energy range between 100 eV and 100 keV corresponding to wavelengths of 100 Å to 0.1 Å is named X-rays. In the context of the *wave-particle dualism*, X-rays hold properties of particles – the photons – and also of waves. The probability of presence of the X-ray photons can be described by an electromagnetic wave. The wave equation can be derived from the MAXWELL equations, cf. textbook by Hecht [2002]. The result is mathematically expressed by:

$$\begin{aligned} \vec{\psi}(\vec{r},t) &= A \cdot e^{-i\phi} \\ &= A \cdot e^{-i\left(\omega t - \vec{k}\vec{r} + \phi_0\right)} \end{aligned} \tag{1.1.1}$$

where A is the wave amplitude. The phase ϕ of the wave is represented by a time-dependent term ωt with ω as the angular frequency and a space-related term $\vec{k}\vec{r}$, where $\vec{k}$ is the wave vector and $\vec{r}$ is the position vector. ϕ_0 describes a phase offset. Although the magnetic properties of X-rays are important for many applications in the field of X-ray science[10,13,71], they are not relevant to this work. Consequently, the description of the magnetic part of the wave will be neglected, here.

The physical observable that is measured by a detector is the intensity I_{det} of the X-ray beam.

$$I_{\text{det}} = |\vec{\psi}|^2 = |A|^2 \tag{1.1.2}$$

In this section, the fundamental quantities that describe the photon-electron interaction – the atomic form factor and the scattering cross section – will be derived. Since the atomic nucleus is too heavy to follow the high-frequency excitation of the X-rays, the interaction of X-ray photons with matter is dominated by the electron-photon scattering process – either elastically (THOMSON) or inelastically (COMPTON). Hence, the probability of photon scattering by the atomic nucleus is neglected. Furthermore, elastic scattering is assumed, that means the photon energy is conserved: $\omega_1 = \omega_2 = \omega$ respectively $|\vec{k}_1| = |\vec{k}_2| = \omega/c$. This assumption justifies the classical approach to describe the scattering process as a forced oscillation. In comparison to that stands the inelastic COMPTON scattering, cf. Sec. 1.2.3, where energy may be transferred between the photon and the electron demanding for the quantum mechanical description of the scattering process.

1.1.1 Interaction with Free Electrons

Based on the general expression given by Equation (1.1.1) the incoming wave $\vec{E}_{\text{in}}$ with the normal vector $\hat{e}_1$ is given by

$$\vec{E}_{\text{in}}(\vec{r},t) \quad = \quad E_{\text{in}} \cdot \; e^{-i(\omega t - \vec{k}_1 \vec{r})} \cdot \hat{e}_1 \; . \tag{1.1.3}$$

Scattering by One Single Free Electron

When the incoming photons are scattered by an electron, the electron is accelerated and radiates.

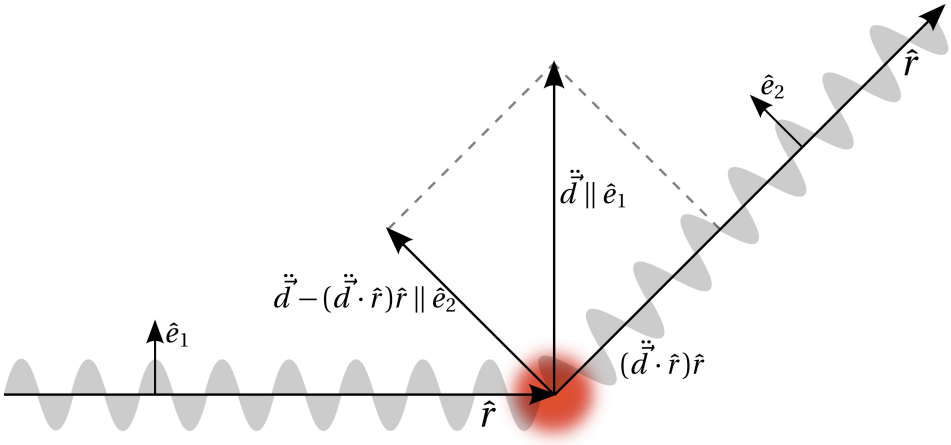

Figure 1.1.1: Scattering process of a photon by a single electron.

With the classical approach of the forced dipole oscillation this is mathematically described as:

$$e_0 \vec{E}_{\text{in}} \quad = \quad m_e \ddot{\vec{d}}, \tag{1.1.4}$$

with the charge of the electron e_0 and with the electron mass m_e. The vector $\ddot{\vec{d}}$ depicts the acceleration in the direction $\vec{d} \parallel \hat{e}_1$. After the scattering process, illustrated in Fig. 1.1.1, the outgoing (radiated) wave field $\vec{E}_{\text{rad}}$ is given by

$$\vec{E}_{\text{rad}}(\vec{r},t) \quad = \quad -\frac{1}{4\pi\epsilon_0} \cdot \frac{e_0}{c^2 r} \cdot \left[\ddot{\vec{d}} - \left(\ddot{\vec{d}}\, \hat{r} \right) \; \hat{r} \right] . \tag{1.1.5}$$

By putting Equation (1.1.3) and (1.1.4) into Equation (1.1.5) the outgoing wave is expressed by

$$\begin{aligned}\vec{E}_{\mathrm{rad}}(\vec{r},t) &= -\underbrace{\frac{1}{4\pi\epsilon_0}\cdot\frac{e_0^2}{m_e c^2}}_{\text{class. electron radius } r_0}\cdot\frac{1}{r}\cdot\underbrace{[\hat{e}_1-(\hat{e}_1\hat{r})\ \hat{r}]}_{\text{polarisation factor } p(\theta)\hat{e}_2}\cdot E_{\mathrm{in}}\cdot e^{-i(\omega t'-\vec{k}\vec{r})}\\ &= -r_0\cdot p(\theta)\hat{e}_2\cdot\frac{1}{r}\cdot E_{\mathrm{in}}\cdot e^{-i(\omega t'-\vec{k}\vec{r})}. \end{aligned} \tag{1.1.6}$$

Here, the actual scattering event is depicted by the classical electron radius times the polarisation factor $r_0\cdot p(\theta)\hat{e}_2$. With Equation (1.1.6), the entire process from the source to the detector is known at the time $t'=t-\frac{r}{c}$ that accounts for the delay due to the finite speed of light c.

In the next step, the single-electron scattering event will be expanded to a many-electron scattering process.

Scattering by Many Free Electrons

The following description of the many-electron scattering process is based on the kinematic approximation which neglects multiple scattering due to the weak electron-photon interaction which again is due to the electron radius r_0 being much smaller than the BOHR radius a_0.

$$r_0=\alpha^2 a_0 \ll a_0 \ \text{ with the SOMMERFELD constant } \alpha=\frac{1}{137}$$

The spatially extended *cloud* of electrons that are involved in the scattering process is described by the electron density $\rho(\vec{r})$ representing the probability for observing the electrons. For each electron, the scattering process is expressed by the propagation of the incoming wave along the path L_j, the actual scatter event and the propagation of the outgoing wave along the path Λ_j, cf. Fig. 1.1.2a. Thus, one scatter path $\vec{E}_j$ can be described by:

$$\vec{E}_j(\vec{r},t) = E_{\mathsf{in}}\cdot\underbrace{\frac{1}{L_j}e^{-i\omega t}}_{\text{propagation source–sample}}\cdot\underbrace{(-r_0)p_j(\theta)\hat{e}_2}_{\text{scattering}}\cdot\underbrace{\frac{1}{\Lambda_j}e^{-i\omega\left(t-\frac{\Lambda_j}{c}\right)}}_{\text{propagation sample–detector.}} \tag{1.1.7}$$

Each of these paths contributes to the total intensity measured in the detector plane $I_{\mathsf{sc}}=I_{\mathsf{det}}$, which is the modulus square of the sum over all scattering paths:

$$I_{\mathrm{det}} = |\sum_j \vec{E}_j(\vec{r},t)|^2 = |\vec{E}_{\mathsf{rad}}(\vec{r},t)|^2 \tag{1.1.8}$$

By choosing one particular scattering path, e.g., $\vec{E}_0$ and by introducing the *scattering vector* $\vec{Q}$, each scatter path $\vec{E}_j(\vec{r},t)$ can be expressed as follows:

$$\begin{aligned}\vec{E}_j(\vec{r},t) &= \vec{E}_0(t)\cdot e^{\frac{i\omega(L_j-L_0+\Lambda_j-\Lambda_0)}{c}}\\ &= \vec{E}_0(t)\cdot e^{-i(\vec{k}_2\vec{r}_j-\vec{k}_1\vec{r}_j)}\\ &= \vec{E}_0(t)\cdot e^{-i(\vec{Q}\vec{r}_j)}. \end{aligned} \tag{1.1.9}$$

Here, it is assumed that the distances L_0, L_j from the source to the sample and the distances Λ_0, Λ_j from the sample to the detector are rather large in comparison to the dimension of the atoms. The scattering vector $\vec{Q}$, also named *wave vector transfer*, is perfectly suited to describe the elastic scattering process. Fig. 1.1.2 shows the propagation paths from the source to the sample and to the detector and also that the scattering vector equals $\vec{Q} = \vec{k}_2 - \vec{k}_1$. The modulus of the scattering vector is defined as q:

$$|\vec{Q}| = q = 2k \sin\theta. \tag{1.1.10}$$

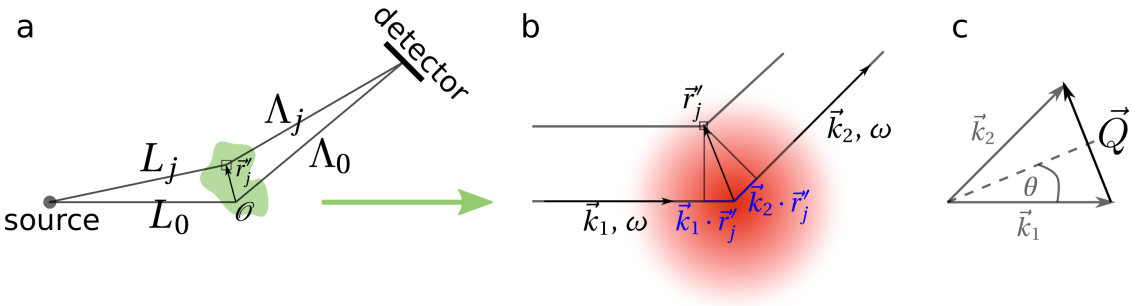

Figure 1.1.2: Scattering process and the derivation of the scattering vector a) shows multiple scattering paths from the source to the sample and from the sample to the detector. b) depicts the actual scattering event and c) shows how the scattering vector $\vec{Q}$ is defined.

Under the assumption that the sum over all scatter paths equals the integral over the electron density $\rho(r')$, the radiated wave $\vec{E}_{\text{rad}}(\vec{r}, t)$ is given as

$$\vec{E}_{\text{rad}}(\vec{r}, t) \;=\; \sum \vec{E}_j(\vec{r}, t) \;=\; \int\limits_{\text{Atom}} d^3r' \rho_e(r')\; \vec{E}_j(\vec{r}, t) \tag{1.1.11}$$

Now, using Equation (1.1.9), a new expression for the scattering process looks like:

$$\vec{E}_{\text{rad}}(\vec{r}, t) \;=\; \vec{E}_0(t) \overbrace{\int\limits_{\text{Atom}} d^3r' \rho_e(r')\; e^{-i(\vec{Q}\vec{r}_j)}}^{f_0(\vec{Q})} \tag{1.1.12}$$

$$\vec{E}_{\text{rad}}(\vec{r}, t) \;=\; E_{\text{in}} \frac{1}{L_0} e^{-i\omega t} \cdot (-r_0) p_j(\theta) \hat{e}_2 \cdot f_0(\vec{Q}) \cdot \frac{1}{\Lambda_0} e^{-i\omega\left(t - \frac{\Lambda_0}{c}\right)} \tag{1.1.13}$$

Here, the atomic form factor $f_0(\vec{Q})$ is introduced.

$$f_0(\vec{Q}) = \int\limits_{\text{Atom}} d^3r' \rho_e(r')\; e^{-i(\vec{Q}\vec{r}_j)} \tag{1.1.14}$$

It is the FOURIER transform of the electron density $\rho_e(r)$. Notably, the scattering process of many free electrons equals the single-electron scattering process of one path, cf. Equations (1.1.6) and (1.1.7), times the atomic form factor.

Up to now, the electrons were considered to be free. In the next step, the binding energies between the electron and the atomic nucleus are included leading to the complete energy-dependent atomic form factor $f(\vec{Q}, \omega)$.

1.1.2 Interaction with Bound Electrons – Atomic Form Factor

In an atom, the electrons cannot be considered as free but bound to the atomic nucleus with element and shell specific binding energies. This fact results in the energy dependency of the atomic form factor, since the electrons behave differently when being excited by photons with an incoming energy close to the binding energies. The binding energies can be modelled using the damped, forced harmonic oscillator:

$$m_e(\ddot{\vec{d}_j} + \underbrace{\gamma_j \dot{\vec{d}_j}}_{\text{attenuation}} + \underbrace{\omega_j^2 \vec{d}_j}_{\text{restoring force}}) = e_0 \vec{E}_{\text{in}}, \tag{1.1.15}$$

with the damping coefficient γ_j and the resonant frequency ω_j. The classical solution is

$$\ddot{\vec{d}_j} = \frac{e_0}{m_e} \cdot \frac{1}{1 - \left(\frac{\omega_j}{\omega}\right)^2 + i\frac{\gamma_j}{\omega}} \cdot \vec{E}_{\text{in}} e^{-i\omega t}, \tag{1.1.16}$$

where the fraction term can be written as the sum of the real and the imaginary part:

$$\frac{1}{1 - \left(\frac{\omega_j}{\omega}\right)^2 + i\frac{\gamma_j}{\omega}} = 1 + \underbrace{\frac{\omega_j^2(\omega^2 - \omega_j^2) - \omega^2\gamma_j^2}{(\omega^2 - \omega_j^2)^2 + \omega^2\gamma_j^2}}_{\text{real part}} - i \underbrace{\frac{\omega^3 \gamma_j(\omega_j)}{(\omega^2 - \omega_j^2)^2 + \omega^2\gamma_j^2}}_{\text{imaginary part}}. \tag{1.1.17}$$

At this point, the classical approach of the forced damped oscillator is extended. The scattering process of bound electrons is integrated in the context of perturbation theory and the transition probability g_{if} of the system from the initial to the final state due to the electron-photon interaction is described by FERMI's Golden Rule[38]:

$$g_{if} \quad = \quad \frac{2\pi}{\hbar} |\left\langle \psi_f \right| \mathcal{H}_{if} \left| \psi_i \right\rangle|^2 \, \delta_{E_f - E_i - \hbar\omega} \tag{1.1.18}$$

Here, the HAMILTONian interaction operator defines the matrix element M_{if}

$$M_{if} \quad = \quad \left\langle \psi_f \right| \mathcal{H}_{if} \left| \psi_i \right\rangle \tag{1.1.19}$$

The entire scattering process can be understood as the superposition of oscillators and the transition probabilty $g(\omega)$ serves to weight the oscillator strengths. Thus, the scattering process is proportional to the interaction transition defined in Equation (1.1.18). Considering this together with the solution of the damped, forced harmonic oscillator given in Equation (1.1.16) and the radiated wave field as given in Equation (1.1.5) leads to

$$\begin{aligned} \vec{E}_{\text{rad}}(\vec{r}, t) \quad = \quad & E_Q \frac{1}{L_0} e^{-i\omega t} \cdot (-r_0) p(\theta) \hat{e}_2 \\ & \cdot \underbrace{\sum_j e^{-i\vec{Q}\vec{r}_j} \int_{\omega_j}^{\infty} d\omega' \frac{g_j(\omega')}{1 - \left(\frac{\omega_j}{\omega'}\right)^2 + i\frac{\gamma_j}{\omega'}}}_{\text{atomic form factor } f(\vec{Q}, \omega)} \cdot \frac{1}{\Lambda_0} e^{-i\omega(t - \frac{\Lambda_0}{c})}. \end{aligned} \tag{1.1.20}$$

The total atomic form factor $f(\vec{Q},\omega)$ consists of three parts and indicates the scattering strength of an atom.

$$\begin{aligned} f(\vec{Q},\omega) &= \sum_j e^{-i\vec{Q}\vec{r}_j} \overbrace{\int_{\omega_j}^{\infty} d\omega' g_j(\omega')}^{\equiv 1} \\ &+ \sum_j e^{-i\vec{Q}\vec{r}_j} \int_{\omega_j}^{\infty} d\omega' g_j(\omega') \frac{\omega_j^2(\omega'^2-\omega_j^2)-\omega'^2\gamma_j^2}{(\omega'^2-\omega_j^2)^2+\omega'^2\gamma_j^2} \\ &- i\sum_j e^{-i\vec{Q}\vec{r}_j} \int_{\omega_j}^{\infty} d\omega' g_j(\omega') \frac{\omega'^3\gamma_j(\omega_j)}{(\omega'^2-\omega_j^2)^2+\omega'^2\gamma_j^2} \end{aligned} \tag{1.1.21}$$

$$\boxed{f(\vec{Q},\omega) = f_0(\vec{Q}) \; + \; f_1(\omega) \; - \; if_2(\omega)} \tag{1.1.22}$$

The term $f_0(\vec{Q})$ is proportional to the atomic number and is dominated by scattering processes by the outer shell electrons, where the binding energies are negligible. Consequently $f_0(\vec{Q})$ is independent of the photon energy, but changes with the scattering vector $\vec{Q}$. In the lower limit $\vec{Q} \to 0$, all scatterers radiate in phase which means $f_0(\vec{Q}=0) = Z$, with Z as the number of electrons (atomic number). For large $\vec{Q}$, the scattering gets out of phase towards the upper limit $f_0(\vec{Q} \to \infty) = 0$.
The real part $f_1(\omega)$ modifies the scattering strength, for X-rays it is a negative number. The imaginary part $f_2(\omega)$ depicts the absorption of photons and is a positive number. Both correction terms are energy-dependent. From Equation (1.1.21), it can be seen that f_1 and f_2 reach their extremal values when the photon energy equals the binding energy – the resonance frequency ω_j – of a certain electron shell. Therefore, the atomic form factor, and consequently the scattering process, is sensitive to elements and to oxidation states. Further discussion can be found in *Elements of Modern X-Ray Physics* by Als-Nielsen and McMorrow [2011].

Molecules and (Non-)Crystalline Structures

In molecules (or bulky samples in general), the atomic form factor describing the scattering strength of electrons is extended to the structure factor describing the scattering strength of m atoms.

$$F_{\text{bulk}}(\vec{Q}) = \sum_m f_m(\vec{Q}) e^{-i\vec{Q}\vec{r}_m} \tag{1.1.23}$$

During the experiments, $|F_{\text{bulk}}(\vec{Q})|^2$ is measured by a detector, cf. Equation (1.1.8). Due to the modulus square, the complex exponent vanishes and the direct access to the phase of the wave function is lost. This is called the *phase problem*. In this work, non-crystalline samples were analysed. To obtain the complex transmission function of such specimens, coherent X-rays, cf. Section 1.2, are used. In this way, the information on the phase of

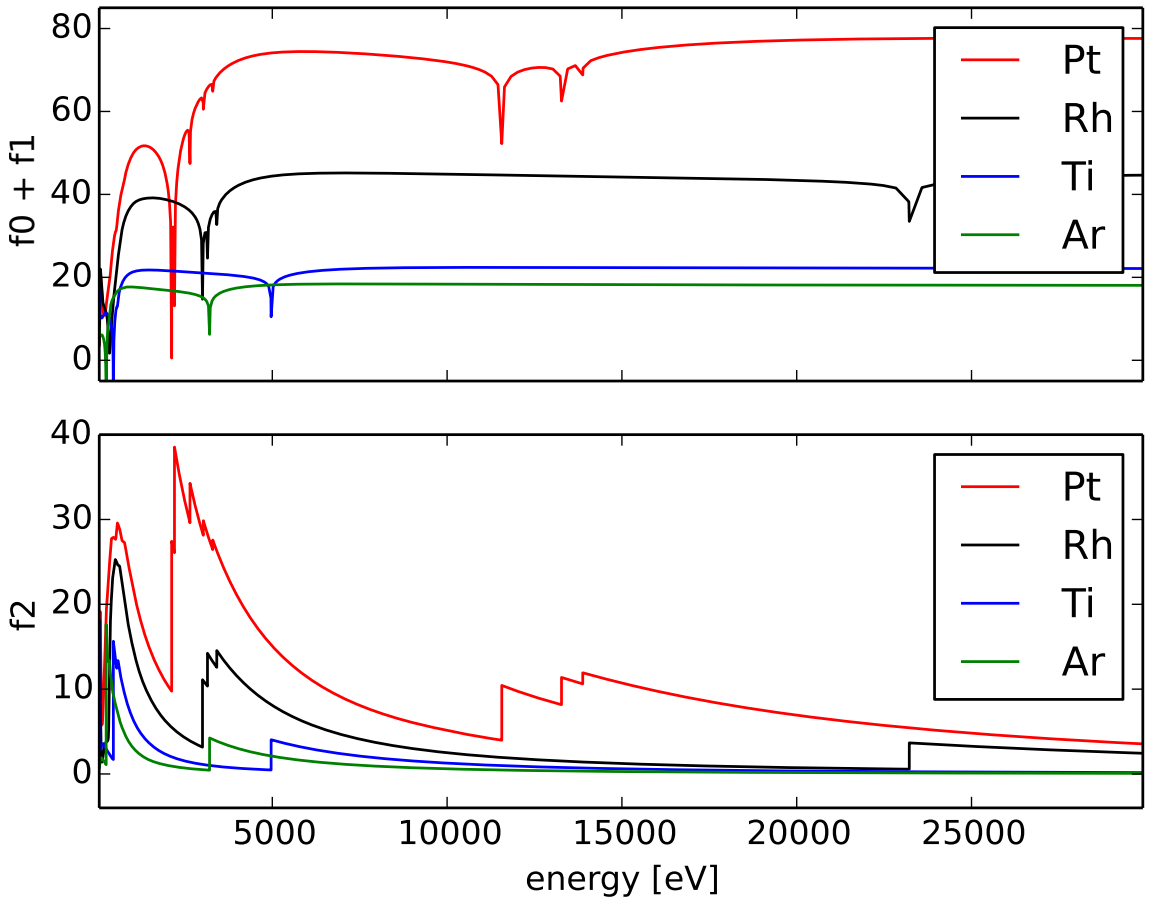

Figure 1.1.3: Resonance effect of the atomic form factor. The real part $f_0 + f_1$ and the imaginary part f_2 of the atomic form factor are separately plotted for several elements using data from the data base by Henke et al. [1993].

an object is conserved during the scattering process and during the wave propagation to the detector. The impossibility to observe complex values – resulting in the loss of phase – can be compensated for by appropriate sampling and advanced phase retrieval algorithms, which will be introduced in the next Chapter in Section 2.1.1.

1.1.3 Scattering Cross Section

In the previous section, the scattered wave function $\vec{E}_{\text{rad}}$ and the atomic scattering factor $f(\vec{Q}, \omega)$, were derived. In an X-ray experiment, only the modulus square of a wave can be detected and the incoming flux Φ_0, which is the number of photons passing through a unit area per second, is proportional to the modulus square of this incoming wave $\vec{E}_{\text{in}}$.

$$\Phi_0 \propto c \cdot \frac{|\vec{E}_{\text{in}}|^2}{\hbar\omega} \tag{1.1.24}$$

After the scattering process, the scattered intensity I_{sc} that is detected at the distance R from the object under the solid angle $\Delta\Omega$ is proportional to the radiated electromagnetic wave $\vec{E}_{\text{rad}}$:

$$I_{\text{sc}} \propto c \cdot R^2 \Delta\Omega \cdot \frac{|\vec{E}_{\text{rad}}|^2}{\hbar\omega} \tag{1.1.25}$$

The scattering process is illustrated in Figure 1.1.4 and the scattering process equals:

$$|\vec{E}_{\text{in}}|^2 d\sigma \quad = \quad |\vec{E}_{\text{rad}}|^2 R^2 d\Omega \tag{1.1.26}$$

Using the Equations (1.1.24) and (1.1.25), the differential scattering cross section $\frac{\mathrm{d}\sigma}{\mathrm{d}\Omega}$ results in

$$\boxed{\frac{\mathrm{d}\sigma}{\mathrm{d}\Omega} = \frac{I_{\text{sc}}}{\Phi_0 \Delta\Omega}} \tag{1.1.27}$$

This fundamental quantity in scattering experiments describes how efficiently a sample scatters radiation as function of the scattered intensity I_{sc} under the solid angle $\Delta\Omega$ compared to the incident flux Φ_0 per unit area per second.

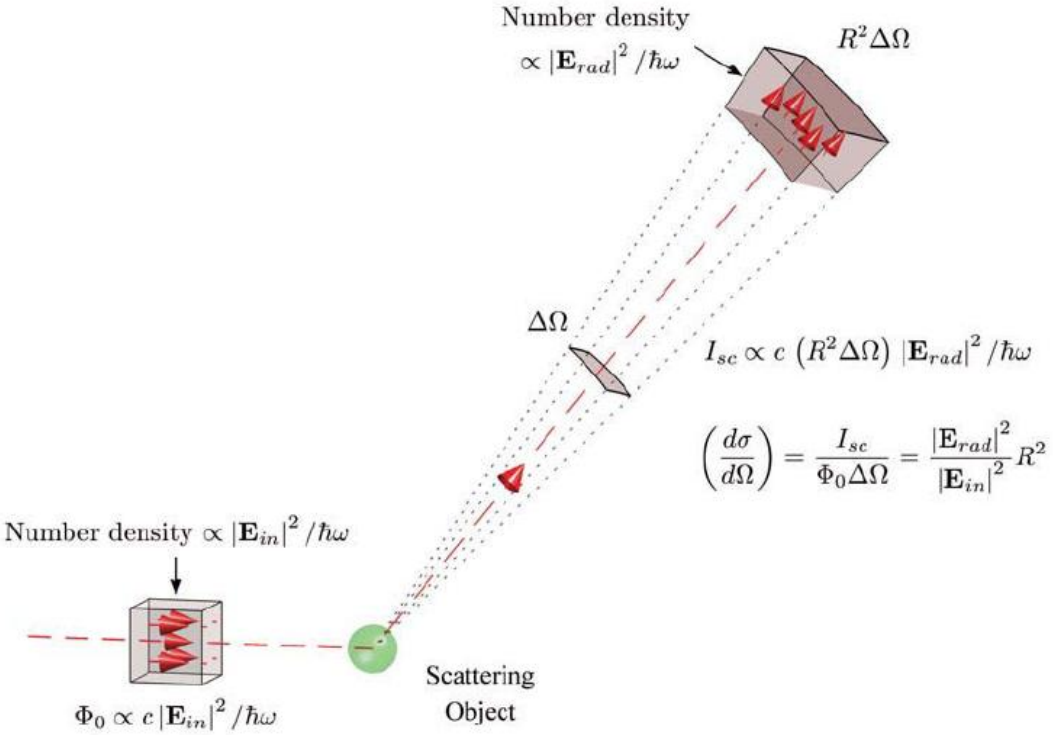

Figure 1.1.4: Illustration of the scattering cross section adopted from Als-Nielsen and McMorrow [2011].

Another important quantity is the THOMSON scattering cross section which describes the scattering length of a *single* free electron with the classical electron radius r_0 in the case of elastic scattering as the low energy limit of COMPTON scattering. Using Equation (1.1.6) in Equation (1.1.26) the THOMSON scattering cross section results in

$$\boxed{\left(\frac{\mathrm{d}\sigma}{\mathrm{d}\Omega}\right)_{\text{Th}} = r_0^2 p^2(\theta).} \tag{1.1.28}$$

Here, the polarisation factor $p(\theta)$ covers the different polarisation planes of radiation.

$$p(\theta) = \begin{cases} 1 & \text{vertical scattering plane} \\ \cos^2(\theta) & \text{horizontal scattering plane} \\ \frac{1}{2}\left(1+\cos^2(\theta)\right) & \text{unpolarised} \end{cases} \tag{1.1.29}$$

The experiments of this work were performed with synchrotron radiation polarised in the horizontal plane. More details on the derivation of scattering cross sections and also on the polarisation factor are provided in *Elements of Modern X-Ray Physics*[2].
In order to describe the photon-electron scattering by an entire atom, the scattering cross section is extended by the atomic form factor.

$$\left(\frac{\mathrm{d}\sigma}{\mathrm{d}\Omega}\right)_{\text{total}} = r_0^2 p^2(\theta) |f(\vec{Q,\omega})|^2 \tag{1.1.30}$$

1.1.4 Refraction, Absorption and Phase Shift

Two of the effects that are observed macroscopically when X-rays interact with matter are the change in direction and the reduction in intensity of the outgoing beam. These phenomena – named refraction and attenuation/absorption – can be described by the complex refractive index $n(\omega)$. In this subsection, the relation between the scattering strength of a material and the corresponding absorption and phase shift of X-rays passing through the material is derived based on the textbook by Attwood [2007]. Figure 1.1.5 illustrates the attenuation of the wave amplitude and how refraction arises due to the retardation/shift of the phase of the wave in the material compared to a reference wave (in vacuum).

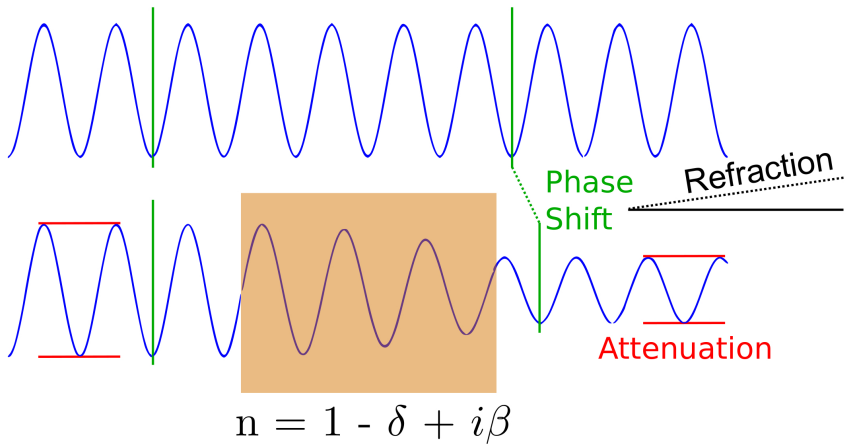

Figure 1.1.5: The complex refractive index n leads to an attenuated and phase shifted wave relative to a reference wave (in vacuum) after passing through a material with the refractive index n.

1.1.4.1 Complex Refractive Index

When the X-rays impinge on an object of the thickness d under a certain angle θ the electrons of the entire layer are excited and they contribute to the exit wave field in reflection and transmission geometry, cf. Fig. 1.1.6. Similar to the derivation of the atomic form factor,

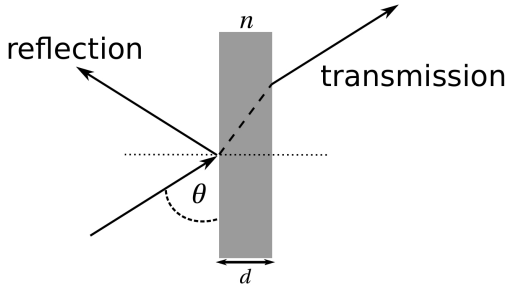

Figure 1.1.6: Transmission of X-rays through a thin layer of the thickness d and the refractive index n

this wave field is obtained by the integration over all scattering paths in the plane. Here, attention is given to the absorption and phase shift of the transmitted X-rays. Thus, only the forward scattering under consideration of the superposition with the undisturbed wave is expressed as:

$$\vec{E}_{\text{trans}}(\vec{r},t) \quad = \quad \left(\hat{e}_1 - r_0 f(\vec{Q}=0)\hat{e}_2 \cdot \mathrm{i}\frac{\lambda \cdot d \cdot n_{\text{EZ}} \cdot \Lambda}{\sin\theta}\right) \frac{E_{\text{in}}}{\Lambda} \cdot e^{-\mathrm{i}\omega\left(t-\frac{\Lambda}{c}\right)}, \tag{1.1.31}$$

with n_{EZ} as the atomic density and Λ as propagation from the sample to the detector plane. The interaction of the X-rays with the electrons results in a slightly different phase velocity $v = {}^{c}/_{n}$ in the material and thus a phase retardation compared to the undisturbed wave in vacuum. This retardation Δt is given by

$$\begin{aligned} \Delta t &= \frac{{}^{d}/_{\sin\theta}}{{}^{c}/_{n}} - \frac{{}^{d}/_{\sin\theta}}{c} \\ &= (n-1) \cdot \frac{d}{c \cdot \sin\theta}\ , \end{aligned} \tag{1.1.32}$$

and illustrated in figure 1.1.6. Using the phase shift $\phi_0 = \omega\Delta t$ in Equation (1.1.1), the transmitted wave is given as:

$$\begin{aligned} \vec{E}_{\text{trans}} &= E_{\text{in}} \cdot e^{+\mathrm{i}\omega\Delta t} \\ &= E_{\text{in}} \cdot e^{\mathrm{i}\omega(n-1)\frac{d}{c\cdot\sin\theta}} \\ &\overset{\text{TAYLOR}}{=} E_{\text{in}} \cdot \left(1 + i\omega(n-1)\frac{d}{c\cdot\sin\theta}\right) \end{aligned} \tag{1.1.33}$$

By comparing the Equations (1.1.31) and (1.1.33) the complex refractive index $n(\omega)$ is identified as:

$$n(\omega) \quad = \quad 1 - \frac{1}{2\pi} r_0 \lambda^2 n_{\text{EZ}} f(\vec{Q}=0) \tag{1.1.34}$$

Together with the atomic form factor from Equation (1.1.22), the complex refractive index can be written as

$$\boxed{n(\omega) = 1 - \delta(\omega) + i\beta(\omega)\ .} \tag{1.1.35}$$

The real part δ and the imaginary part β are given as

$$\delta(\omega) = \frac{n_{\mathrm{EZ}}}{2\pi}\, r_0\, \lambda^2 (Z + f_1(\omega)) \tag{1.1.36}$$

$$\beta(\omega) = \frac{n_{\mathrm{EZ}}}{2\pi}\, r_0\, \lambda^2 (f_2(\omega))\ , \tag{1.1.37}$$

where the atomic density $n_{\mathrm{EZ}} = N_A \frac{\rho}{A}$ is related to the AVOGADRO's constant N_A, the mass density ρ and the atomic mass A.

The refractive index is energy dependent and since δ and β are connected to the resonant corrections of the atomic scattering factor, $n(\omega)$ also shows the resonant behaviour at photon energies close to the binding energies of the electrons. Whereas the real part δ is proportional to the sum of $f(\vec{Q} = 0) = Z$ and f_1, the imaginary part β is proportional to f_2 and thus connected to absorption effects. By convention, the refractive index in vacuum is one. In contrast to visible light, where n lies in the range of 1.5 to 1.8 for different kinds of glass, the refractive index n for X-rays is slightly smaller than unity. This comes from the fact that the energies of X-rays are usually higher than the binding energies of the electrons to the atomic nucleus (potentially except from inner K- or L-shells). This fact results in interesting properties of X-Rays, such as the total *external* reflection, which is utilised by focusing mirrors or higher-order reflecting mirrors, cf. Section 3.1.

1.1.4.2 Absorption

The attenuation of X-Rays in matter is described by the LAMBERT-BEER Law. The intensity decreases exponentially with the thickness d of the material and the absorption coefficient μ.

$$I_{\mathrm{out}} = I_{\mathrm{in}} \cdot e^{-\mu d} \tag{1.1.38}$$

The absorption coefficient μ is related to the imaginary part in the scattering process and can be expressed by β and as a function of the energy or the wavelength λ, respectively.

$$\mu \;=\; \frac{4\pi}{\lambda}\beta \tag{1.1.39}$$

Later on in section 2.2, the application of X-ray absorption in spectroscopy techniques is presented by the examples of the two common techniques EXAFS and XANES.

1.1.4.3 Phase shift

The other important property of the interaction of X-rays with matter is the shift in the wave's phase when passing through a material. This phase shift is always a relative measure, that means the phase shift caused by a certain material is related to another phase, usually to the phase of a reference wave in vacuum. Because of this, the Δ sign describing a difference term will be omitted when describing the phase shift of a material. If not explicitly stated otherwise, the phase shift relatively to the vacuum phase is meant. Looking at a

plane wave $\vec{E}_{\text{sample}}(z)$ that propagates through a material with the refractive index n the phase shift compared to a reference wave in vacuum evolves:

$$\begin{aligned} \vec{E}_{\text{sample}}(z) &= E_0 e^{iknz} \\ &= \underbrace{E_0 e^{ikz}}_{\text{wave in vacuum}} \cdot e^{-ik\delta z} \cdot e^{-k\beta z} \end{aligned} \tag{1.1.40}$$

The first term in Equation (1.1.40) equals an undisturbed reference wave in vacuum. For a weakly absorbing object, the relative phase shift between a wave in vacuum and the wave passing through a sample of the thickness d is given by the exponent of the second term. In general, the phase shift ϕ can be calculated by

$$\boxed{\phi = \frac{2\pi}{\lambda} \int_0^d -\delta \mathrm{d}z.} \tag{1.1.41}$$

1.1.4.4 KRAMERS-KRONIG Relationship

The previous sections have shown that the scattering process can be described by either the complex atomic form factor or the complex refractive index. In real experiments, usually either the real part, the dispersion, or the imaginary part, the absorption, of these physical terms is measured. Under certain conditions, the KRAMERS-KRONIG relationship connects the real part and the imaginary part of a complex function.

For this, the complex atomic scattering factor can be considered as a frequency-dependent linear response function $\chi(\omega)$. Since a physical system cannot respond to a force before the force was applied, $\chi(t - t') = 0$ for $t < t'$, the causality condition is given and consequently the FOURIER transform $\mathcal{F}[\chi(t)] = \chi(\omega)$ is analytic in the upper half-plane. Thus the real and imaginary part of this function are connected by the integrals:

$$\mathrm{Re}\left[\chi(\omega)\right] = +\frac{1}{\pi}\,\mathcal{C}\int_{-\infty}^{+\infty}\frac{f\,\mathrm{Im}\left[\chi(\omega')\right]}{(\omega'-\omega)}\mathrm{d}\omega' = +\frac{2}{\pi}\,\mathcal{C}\int_{0}^{+\infty}\frac{\omega'\,\mathrm{Im}\left[\chi(\omega')\right]}{(\omega'^2-\omega^2)}\mathrm{d}\omega' \tag{1.1.42}$$

$$\mathrm{Im}\left[\chi(\omega')\right] = -\frac{\omega}{\pi}\,\mathcal{C}\int_{-\infty}^{+\infty}\frac{\mathrm{Re}\left[\chi(\omega)\right]}{(\omega'-\omega)}\mathrm{d}\omega' = -\frac{2\omega}{\pi}\,\mathcal{C}\int_{0}^{+\infty}\frac{\mathrm{Re}\left[\chi(\omega)\right]}{(\omega'^2-\omega^2)}\mathrm{d}\omega' \tag{1.1.43}$$

where $\mathcal{C}$ is the CAUCHY principle value[3] handling the poles at $\omega = \omega'$.

The Equations (1.1.42) and (1.1.43) can be derived from the physical principles linearity, causality and the inability of a physical system to respond to excitation at indefinitely high frequencies[14]. However, Kramers [1927] and de L. Kronig [1926] discovered these relations in a more specific way for the calculation of the real and imaginary part of the refractive index. Using the KRAMERS-KRONIG relation it is possible to calculate the phase shift generated by a sample via the real part f_1 from absorption data measured in an experiment. This is common for many applications where resonant data sets are measured.

In this work, it will be used to calculate reference curves of the expected phase shift. A detailed description and calculation examples will be given in the methods chapter in Section 2.2.3.

1.2 Coherence

Coherence describes the correlation between the phase of waves. A constant phase relation of waves builds the basis for coherent scattering experiments. In this section, the transversal and longitudinal coherence length are introduced.

1.2.1 Longitudinal Coherence

The longitudinal coherence is also called temporal coherence, since the difference in the phase is changing over time. Partial longitudinal coherence arises from the limited spectral bandwidth that is given by the monochromator. The distance when the wave minimum and

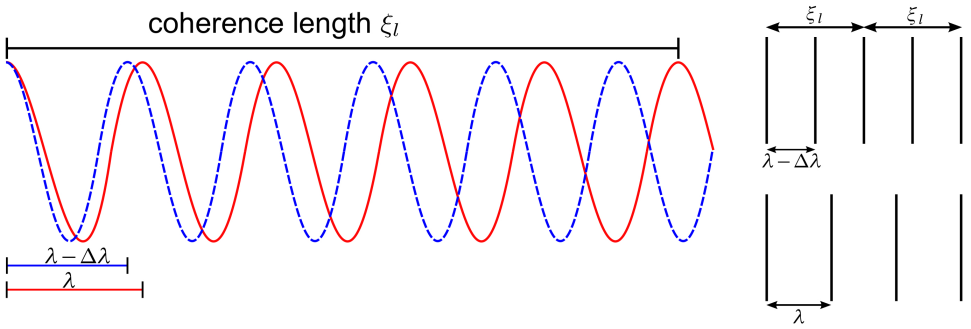

Figure 1.2.1: Basic scheme for the longitudinal coherence length.

maximum overlap is defined as longitudial coherence length ξ_l.

$$n\lambda \;=\; (n+1)(\lambda - \Delta\lambda) \;=\; 2\xi_l.$$

Under the assumption of only small variations $\Delta\lambda$ compared to the wavelength λ the term is derived:

$$\begin{aligned} n \;=\; \frac{\lambda}{\Delta\lambda} \;\Rightarrow\; \lambda\frac{\lambda}{\Delta\lambda} \;&=\; 2\xi_l \\ \xi_l \;&:=\; \frac{1}{2}\lambda\frac{\lambda}{\Delta\lambda}. \end{aligned} \tag{1.2.1}$$

The longitudinal coherence length ξ_l defines the maximum path difference between scattered waves for which the interference pattern is still visible. Therefore, the coherence length influences the dimensions of a specimen, that are coherently illuminated.

1.2.2 Transversal Coherence

The origin of limited transversal coherence, also called spatial coherence, is the extend of the source. Whereas the wave front of an ideal point source is diffracted singularly and results in an interference pattern with perfect contrast, each point of an extended source S

contributes to a superposition of fringes, which decreases the visibility of the speckles in the diffraction pattern. The interference fringes are detected under the angle α after they

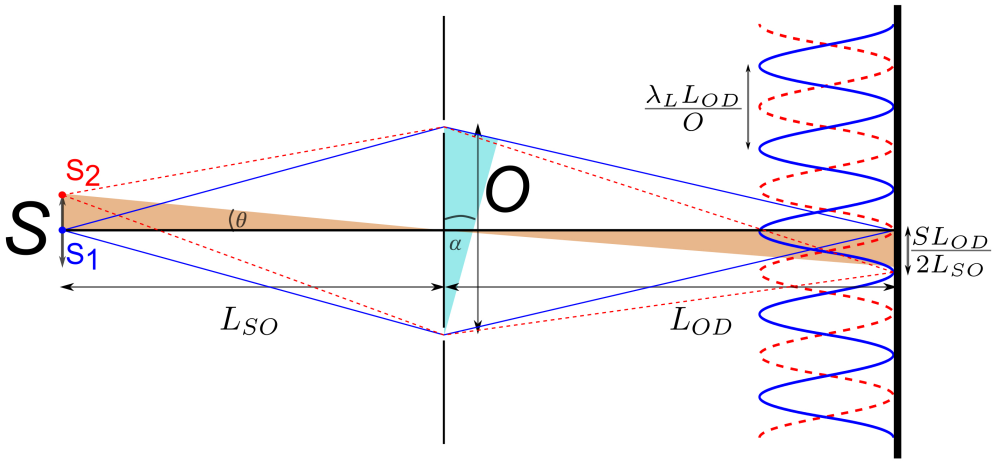

Figure 1.2.2: Basic scheme for the transversal coherence length.

were diffracted by an object of size O

$$\alpha \approx \frac{m\lambda}{O}. \tag{1.2.2}$$

Related to the optical axis, m counts the minima for $m = \pm^{2j+1}/_2$ and the maxima for $m = \pm j$. This process occurs for every point of the extended source. When a minimum and a maximum of different diffraction paths overlap

$$\frac{\lambda}{S} = \frac{\lambda}{2S} + \frac{S}{2L_{SO}} \tag{1.2.3}$$

the fringes cannot be resolved anymore and the diffraction information is lost. The condition above defines the maximum extent of the object O and consequently the coherence length ξ_t depends on the source size S, the wavelength λ and the distance between the source and the object L_SO as follows:

$$O = \frac{\lambda L_{SO}}{S} := \xi_t. \tag{1.2.4}$$

1.2.3 Incoherent Scattering

Incoherent scattering such as COMPTON scattering and scattering generated by the interaction of X-rays with the air molecules, components of the experimental setup such as pinholes or windows[1] and the detector material are considered as parasitic as they negatively influence the experimental data quality. In this section, the basic physical processes are described.

[1] e.g., made of Kapton®, diamond or beryllium

COMPTON Scattering

COMPTON scattering is inelastic[2] scattering of photons by charged particles such as electrons, cf. Als-Nielsen and McMorrow [2011]. In contrast to the classical description of the X-rays as waves, the COMPTON effect is considered within the concept of wave-particle dualism in quantum theory, where the X-rays are as well represented by a beam of photons. In a collision event, a fraction of energy of the photon is transferred to the electron, thus the energy (wavelength) of the scattered photon is lower (larger) than that of the incident one. Under the assumption of conservation of energy and momentum[2] during the process the scattering formula is derived:

$$\lambda_{\text{sc}} - \lambda_{\text{in}} = \frac{\hbar}{m_e c}(1 - \cos\theta) \tag{1.2.5}$$

Here, λ_{in} is the initial wavelength, λ_{sc} is the wavelength after scattering, $\hbar$ is the PLANCK constant, m_e is the electron rest mass, c is the speed of light, and θ is the scattering angle between the incoming and outgoing beam. The COMPTON scattering length is defined by

$$\lambda_C = \frac{\hbar}{m_e c} \tag{1.2.6}$$

The difference in wavelength before and after the scattering event is proportional to the COMPTON wavelength. Comparing the THOMSON and the COMPTON scattering length it is noticeable that the latter is incoherent; there is no fixed phase relationship between the scattered photons.

In the measurements of this work, COMPTON scattering will mainly occur as a parasitic scattering effect due to the interaction with air, experimental components and the detector material itself at higher photon energies. Since all experiments were performed at energies below 12 keV the amount of parasitic COMPTON scattering is comparatively low.

Air Scattering

In principle, the scattering of X-rays by the atoms of air is a coherent and elastic scattering process as described in the first section. However, since air scattering occurs along the entire beam path from the aperture of the optics to the detector, all scattering events sum up incoherently. In addition, the position of the air molecules is not constant over time which also leads to incoherent superposition of the scattering events.

1.3 Wave Propagation

After the X-rays interacted with the sample material as discussed in the beginning of this chapter, the wave field $\psi(x, y, z)$ propagates from the sample plane $\vec{S}(u, v; z = 0)$ towards the detector plane $\vec{P}(x, y, Z)$. The propagation process is shown in simplified terms in Fig. 1.3.1. By means of that, this section illustrates how a diffracted complex wave field $\psi_Z(x, y)$ can be calculated from an initial complex wave field $\psi_0(u, v)$.

[2] *Inelastic* refers to the change in energy/wavelength of the scattered photons; the total energy and momentum of the entire scattering process are naturally conserved.

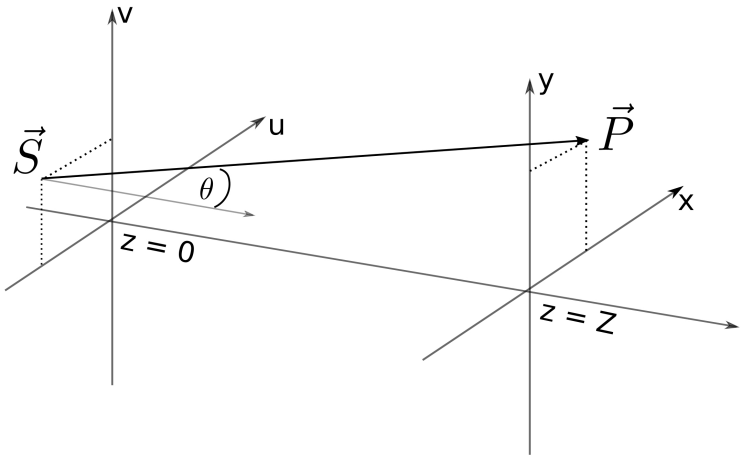

Figure 1.3.1: Wave propagation and Fresnel-Kirchhoff Integral. Free wave propagation from a point $\vec{S}(u, v, z = 0)$ to the point $\vec{P}(x, y, z = Z)$ under the paraxial approximation.

According to the HUYGENS-FRESNEL principle, the superposition of the spherical wavelets originating from all points of an initial wave describe a new wave front at a later time at any point in space[15]. A mathematical description of the wave propagation is gained from the solution of the homogeneous wave equation by the FRESNEL-KIRCHHOFF integral:

$$\psi_Z(x,y) \quad = \quad \frac{1}{i\lambda}\iint \psi_0(u,v)\frac{e^{ik\vec{r}}}{\vec{r}}\cos(\theta)\; dudv \tag{1.3.1}$$

Here, the distance r from the object plane to the propagation plane is given by $r = \sqrt{(x-u)^2+(y+v)^2+Z^2}$. With the paraxial approximation, the distance Z between the two planes is considered to be large in comparison to the dimensions of the object and the diffraction pattern. This means that the X-rays are mostly travelling along the optical axis under the angle $\theta \approx 0$ consequently the factor $\cos(\theta) = 1$. Furthermore, the paraxial approximation justifies to expand r around Z resulting in

$$r \quad \approx \quad Z + \frac{(x-u)^2}{2Z} + \frac{(y-v)^2}{2Z} \tag{1.3.2}$$

stopping after the second order term. The FRESNEL approximation is obtained by considering the higher orders of r only in the exponent in Equation (1.3.1).

$$\psi_Z(x,y) = \qquad -\frac{e^{ikZ}}{i\lambda Z}\iint \psi_0(u,v)e^{\frac{ik}{2Z}\left[(x-u)^2+(y-v)^2\right]}\; dudv \tag{1.3.3}$$

In order to rewrite this equation as the convolution of the original wave field ψ_0 with the FRESNEL operator P_Z

$$\psi_Z(x,y) \quad = \quad \psi_0(u,v) \otimes P_Z(u,v), \tag{1.3.4}$$

the FRESNEL operator P_Z describing the free propagation of X-rays is defined as

$$P_Z(u,v) \quad = \quad -\frac{e^{ikZ}}{i\lambda Z}e^{\frac{ik}{2Z}(u^2+v^2)}. \tag{1.3.5}$$

By expanding the quadratic terms in Equation (1.3.2) the FRESNEL integral is rewritten as

$$\psi_Z(x,y) \quad = \quad -\frac{e^{ikZ}}{i\lambda Z} e^{\frac{ik}{2Z}(x^2+y^2)} \iint \psi_0(u,v) e^{-\frac{ik}{Z}(xx'+yy')} e^{\frac{ik}{2Z}(u^2+v^2)} \, dx'dy' \tag{1.3.6}$$

For a finite object size and large distances between the object and the detector plane, the quadratic phase factor of the last exponent in the integral is negligible, since

$$k\frac{u^2+v^2}{2Z} \ll \pi. \tag{1.3.7}$$

With the object dimension a and wavelength λ the far-field condition can be defined as

$$Z \quad \gg \quad \frac{a^2}{\lambda}, \tag{1.3.8}$$

leading to the dimensionless FRESNEL number f_n

$$f_n \equiv \frac{a}{\lambda Z} \quad \ll \quad 1. \tag{1.3.9}$$

The far-field condition leads to the FRAUNHOFER approximation, where the wave field is expressed by

$$\boxed{\psi_Z(x,y) = A_Z(x,y) \iint \psi_0(u,v) \; e^{-\frac{ik}{Z}(xu+yv)} dudv} \tag{1.3.10}$$

with the far-field propagator A_Z defined as

$$A_Z(x,y) \quad = \quad -\frac{e^{ikZ}}{i\lambda Z} \, e^{\frac{ik}{2Z}(x^2+y^2)} \, . \tag{1.3.11}$$

The general n-dimensional definition of the FOURIER transform is

$$\boxed{\Psi(\vec{k},t) \; = \; \mathcal{F}\left[\psi(\vec{r},t)\right] \; = \; \frac{1}{(2\pi)^{\frac{n}{2}}} \int\limits_{\mathbb{R}^n} \psi(\vec{r},t) e^{i\vec{k}\vec{r}} \mathrm{d}r^n \, .} \tag{1.3.12}$$

In Equation (1.3.10), the integrand depicts the two-dimensional FOURIER transform, thus the wave field in the far-field – the FRAUNHOFER diffraction – can be written as

$$\psi_Z(q_x,q_y) \quad = \quad A_Z\left(q_x\frac{Z}{k}, q_y\frac{Z}{k}\right) \mathcal{F}\left[\psi_0(u,v)\right](q_x,q_y) \tag{1.3.13}$$

with the coordinates in reciprocal space $(q_x,q_y) = (\frac{kx}{Z}, \frac{ky}{Z})$.

Depending on the experimental conditions, the near or far-field diffraction condition is applied in the reconstructions. In this work, the diffraction patterns were recorded in the far-field and the FRAUNHOFER approximation will be applied in the reconstruction process, cf. Section 2.1.1.

2 Methods

Based on the theory given in the previous chapter, here, the methods relevant to the evaluation procedure in Chapter 4 are described. Basically, to understand how chemical imaging was realised in this work, knowledge of two main techniques – ptychography and X-ray spectroscopy – is required. First, the main principles of ptychographic measurements as well as the reconstruction algorithm are introduced along with some special extensions to the algorithm that are important for the evaluation later on. Afterwards, the chemical aspect based on spectroscopy techniques is explained. The combination of both techniques, cf. Section 2.2, leads to resonant ptychography for chemical imaging which requires further post processing such as image alignment, cf. Section 2.3. At last, different methods to determine the image quality in terms of spatial resolution, cf. Section 2.4, are shown together with the analysis of the diffraction patterns to determine the data quality for different experimental conditions, e.g. with and without a beamstop. A detailed description of the experimental procedures and detectors at the beamline P06 will be given in the next Chapter *"Experimental Setup"*.

2.1 Ptychography

Ptychography is an imaging technique based on coherent diffraction. For ptychographic measurements, the specimen is scanned through a confined beam recording a (far-field) diffraction pattern of the scattered wave behind the specimen at each scan point. Due to an appropriate overlap between the illumination at adjacent scan points, a microscopic image in form of the object's complex transmission function can be retrieved computationally from the ensemble of coherent diffraction patterns using an iterative reconstruction process. In this way, ptychography is able to solve the *phase problem* which was addressed in Section 1.1.2.

Figure 2.1.1 illustrates a simplified ptychographic setup and a basic scanning scheme to record the diffraction patterns. All the ptychograms of this work were recorded by using such a rectangular grid scan, but in fact, the trajectory of the scan points can follow a random scan pattern. The choice of the scan pattern must only fulfil the sampling, cf. Section 2.1.3 and the exact position of the beam on the sample for each scan point must be known in order to achieve the best reconstruction results. Differences between the real positions and the positions provided to the phase retrieval algorithm lead to artefacts and distortions in the reconstructed object function. Extensions of the basic phase retrieval algorithm, cf. Section. 2.1.7, as well as post-processing such as image alignment, cf. Section 2.3, can provide remedy to positioning errors.

The basic ptychographic model expects a coherent incident probe that is constant during the entire scan. Furthermore, the intensity measured in the diffraction patterns

is assumed to originate purely from the scattering process of the incident probe and the sample area that is illuminated at a particular scan point. Deviations from this basic model must be carefully treated by additional constraints and modified assumptions during the reconstruction algorithm. The basic algorithm is described in the following section. Afterwards, modifications will be discussed.

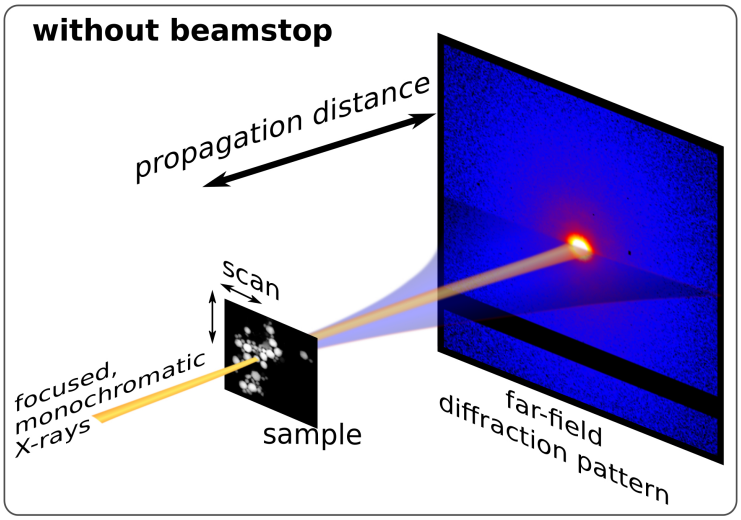

(a) For a ptychographic scan, a confined, monochromatic X-ray beam passes through the sample. The transmitted wave propagates to the detector and its intensity distribution is recorded as a so-called diffraction pattern.

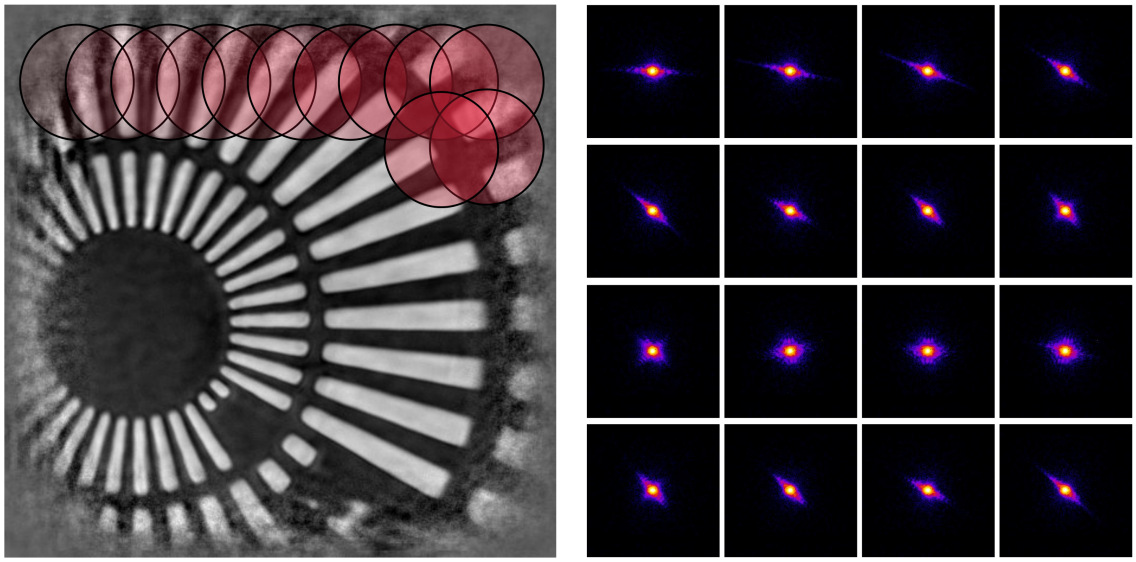

(b) Left: The sample is scanned with sufficient overlap between adjacent scan points. Right: For each scan point an individual diffraction pattern is recorded.

Figure 2.1.1: Ptychographic Setup and Scanning Scheme

2.1.1 Phase Retrieval Algorithm

In general, there are different approaches to iteratively retrieve the lost phase from the diffraction patterns. The most common ones are the *extended Ptychograpic Iterative Engine*

(ePIE)[65] and the *Difference Map* (DM)[97]. In this work, an own implementation of the ePIE algorithm was used for the ptychographic reconstruction. The main procedure of the algorithm can be described in five steps.

From the diffraction patterns to the object and probe function in 5 steps:

1. An initial guess for the object function $\mathcal{O}(\vec{r})$ and an initial guess for the probe function $\mathcal{P}(\vec{r})$ are multiplied to model an initial complex transmission function $\psi(\vec{r})$ in real space in the sample plane.

$$\psi_n(\vec{r}) \quad = \quad \mathcal{P}(\vec{r})\mathcal{O}(\vec{r} - \Delta\vec{r}_n), \tag{2.1.1}$$

   where $\vec{r}$ is the position vector and $\Delta\vec{r}_n$ represents the relative shift of the sample in real space for the n$^{\text{th}}$ diffraction pattern.

2. Via the FOURIER transform the wave function $\psi(\vec{r})$ is converted into reciprocal space, which is equal to a wave propagation from the sample to the detector plane in the far field.

$$\Psi_n(\vec{Q}) \quad = \quad \mathcal{F}\left[\psi_n(\vec{r})\right]. \tag{2.1.2}$$

   The detector measures $I_n(\vec{Q})$, the square modulus $|\Psi_n(\vec{Q})|^2$ of the propagated transmission function.

3. Thus, the values of $\Psi_n(\vec{Q})$ can be updated by inserting the square root of the measured intensity $I_n(\vec{Q})$ of the n$^{\text{th}}$ diffraction pattern:

$$\Psi'_n(\vec{Q}) \quad = \quad \sqrt{I_(\vec{Q})} \cdot \frac{\Psi_n(\vec{Q})}{|\Psi_n(\vec{Q})|}. \tag{2.1.3}$$

4. The updated transmission function $\Psi'_n(\vec{Q})$ is propagated back into real space by the inverse FOURIER transform.

$$\mathcal{F}^{-1}\left[\Psi'_n(\vec{Q})\right] \quad = \quad \psi'_n(\vec{r}). \tag{2.1.4}$$

5. With the refined transmission function in real space $\psi'_n(\vec{r})$ the object and probe function are updated:

$$\mathcal{P}_{j+1}(\vec{r}) \quad = \quad \mathcal{P}_j(\vec{r}) + \beta\frac{\mathcal{O}^*_{j+1}(\vec{r} + \Delta\vec{r}_n)}{|\mathcal{O}_{j+1}(\vec{r} + \Delta\vec{r}_n)|^2_{\max}}(\psi'_n(\vec{r}) - \psi_n(\vec{r})) \tag{2.1.5}$$

$$\mathcal{O}_{j+1}(\vec{r}) \quad = \quad \mathcal{O}_n(\vec{r}) + \alpha\frac{\mathcal{P}^*_j(\vec{r} - \Delta\vec{r}_j)}{|\mathcal{P}_j(\vec{r} - \Delta\vec{r}_n)|^2_{\max}}(\psi'_n(\vec{r}) - \psi_n(\vec{r})) \tag{2.1.6}$$

   α and β serve as regularisation coefficients to control the update strength of the probe and object function.

   Different ways of updating the probe and the object as well as different ways of normalisation, instead of the uniform norm, are conceivable, they influence the stability and speed of convergence[65,72].

These steps are performed for all N diffraction patterns in one iteration j. They are repeated until the difference between the measured and the calculated intensity for all diffraction patterns converges. Depending on the data quality this is the case after only several 10 or up to several 100 of iterations or even more. Fig. 2.1.2 concludes all steps of one iteration of the reconstruction process.

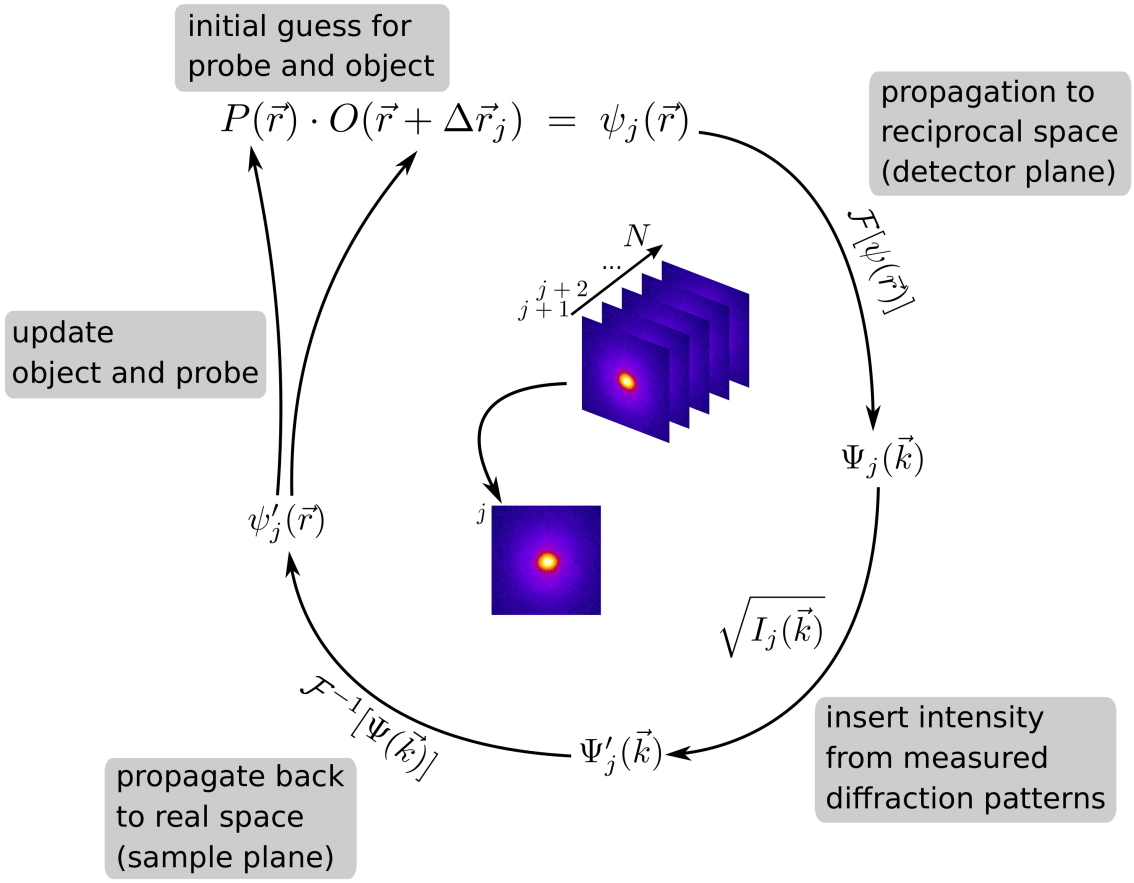

Figure 2.1.2: ePIE scheme. This scheme shows one iteration of the ePIE reconstruction algorithm.

2.1.2 Error Measure

To determine the progress of the reconstruction, a quantitative counter is required. For this, the error function R is introduced.

$$R = |\sqrt{I_j} - |\Psi_j||^2 \tag{2.1.7}$$

R calculates the difference between the square root of the recorded diffraction pattern I_j and the current calculated transmission function in the detector plane Ψ_j. Depending on the noise and background level in the recorded diffraction patterns, the error measure converges to a higher or lower level.

2.1.3 Sampling

In order to reconstruct the complex transmission function properly, the scattering information from the sample must be sufficiently sampled. In ptychography, the term *sampling* is two-fold: On the one hand, sufficient sampling relates to the overlap between adjacent scan points in order to create sufficient redundancy of information in neighbouring diffraction patterns in order to reconstruct the complex object transmission – including the hidden phase as well as the complex probe function. Different scan patterns such as a grid, a Fermat spiral or a concentric pattern, can handle different percentage of overlap as shown by Bunk et al. [2008] or are advanteageous in terms of efficient scanning by uniformly covering the scan area[44]. In the work at hand, basic grid scan patterns were applied with an overlap of 60 % to 70 % for the ptychographic scans.

On the other hand, the speckle pattern in each diffraction pattern must be sufficiently sampled. That means, that the minima and maxima of the interference patterns must be sufficiently resolved. Therefore, the pixel size of the detector must be small enough depending on the probe size, the setup geometry and photon energy. Figure 2.1.3 shows the relation between the distance of minima and maxima in the diffraction pattern and the pixel size of the detector. The physical pixel size of the detector p_{Det} at a given sample-

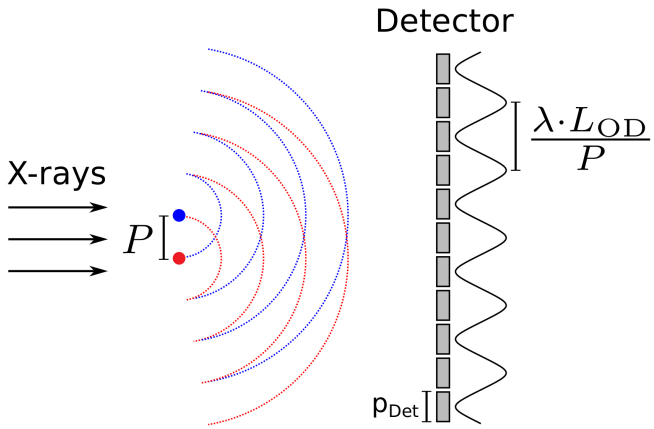

Figure 2.1.3: Sampling of the Speckles. The maximal size of the incoming probe P and the pixel size in the reconstructions depend on the propagation distance L_{OD}, the pixel size of the detector p_{Det} and the wavelength λ of the X-rays.

detector distance L_{OD} sets the limit to the maximum size of the illuminating probe P. This maximum probe size P also depends on the wavelength λ or the photon energy E, respectively, and is given by:

$$P < \lambda \cdot \frac{L_{\text{OD}}}{2 \cdot p_{\text{Det}}} \tag{2.1.8}$$

This term equals the half of the speckle size, which is required since only the square modulus of the propagated wave function can be detected.

Due to the discrete pixel size p_{Det} in reciprocal space, the ptychographic reconstruction also results in a discrete pixel size x_{rec} in real space. The pixel size x_{rec} in the ptychographic reconstruction depends on the sample-detector distance and the field-of view used for the

reconstruction, which is given by the pixel size of the detector times the number of pixels N_{Det}.

$$\Delta x_{\text{rec}} = \lambda \cdot \frac{L_{\text{OD}}}{N_{\text{Det}} \cdot p_{\text{Det}}} \tag{2.1.9}$$

The number of pixels N_{Det} is also called the *cropping* of the diffraction patterns. It is chosen based on the scattering strength of the object, i.e. the highest q-values where a scattering signal can be detected over scattering background, and often also to speed-up the computation of preliminary reconstructions.

As resonant ptychography, cf. Section 2.2.2, is performed at different energies, the pixel size in the reconstruction changes concomitantly. Depending on the energy range, the varying pixel size has to be corrected to achieve the same scaling for all reconstructions, which is important for the chemical imaging procedure, cf. Section 2.3.

2.1.4 Initial Guess

In general, to start a ptychographic reconstruction, no specific a priori information about the sample or the probe is needed. However, the computation of the initial complex transmission function requires a complex-valued array for the probe and the object which will be updated during the iterative reconstruction process. These arrays can be empty or random arrays, but for real measurements usually the initial guess is chosen according to the experimental conditions. At the beamline P06, the nano-focusing refractive lenses produce a GAUSSian-shaped focus, thus a suitable initial guess of the probe function for the ptychographic reconstruction is a complex-valued 2D array of a GAUSSian. The initial probe amplitude is set based on the measured flux of the incoming beam. In some cases, especially for fairly weakly scattering samples, it is helpful to start with an initial guess for the probe function using a reconstructed probe function of a preceding measurement under exactly the same or similar conditions. For the initial guess of the object function no further assumptions are set. The initial object function is a complex-valued 2D array depicting a fully transparent object (modulus = 1).

2.1.5 Ambiguities in the Reconstruction

The general idea of the overlap in a coherent ptychographic scan is to create sufficient redundancy in information to deconvolve the complex object function and the complex probe function in order to finally achieve an unambiguous reconstruction of each function separately. However, this is not always the case, ambiguities can occur and result in artefacts in the reconstruction caused by inherent limitations of the technique or by deviations of the measured data from the basic ptychographic model.

An inherent limitation is posed by the phase shift in the reconstruction, which can only be expressed by values between 0 and 2π. Consequently, in a reconstruction of an object with a phase shift larger than one period length, so-called *phase wrapping* appears as an artefact of discontinuity, where the algorithm tries to keep all phase values in the range of 0 and 2π by shifting larger values back to this range.

Another artefact originates from the attempt of the algorithm to preserve the all-over phase in an object during reconstruction. This leads to *phase ramps*, i.e. a linear gradient in phase along the 2D image, which is usually correctable during post-processing with the help of a phase gradient analysis.

Beside these intrinsic limitations, in particular variations of the illuminating probe are a principal reason for artefacts in a ptychographic reconstruction. Against the assumption of the ptychographic model, the probe intensity or probe phase may vary during a ptychographic scan. Changes in the incident probe intensity (changes in the photon flux) will mainly influence the reconstruction of the object amplitude. This can usually be correct by normalisation of the intensity, cf. Section 2.1.6.

Angular changes of the incident probe that might be caused by angular vibrations of the monochromator or other optics such as the high-order reflecting mirrors, result in variations of the phase of the incident probe. However, the probe in general and consequently the probe phase is considered constant during the reconstruction. Therefore, the algorithm tries to compensate the phase variations in the probe by mismatching the change in phase to the object phase shift. Angular variations and concomitant phase variations are difficult to correct during the reconstruction. Thus, resulting artefacts must be carefully considered during all further post-processing and analysis.

2.1.6 Additional Constraints

The advantage of self-consistent data sets that lead to the reconstruction of the object and probe without further information than the diffraction patterns and the corresponding positions cannot always be exploited. Measurement errors such as vibrations and drifts of the sample, variations of the incoming beam as well as background and noise are not considered in the basic ptychographic model. Therefore, further constraints are required during the reconstruction process in order to achieve quantitatively reliable results that comply with the physical conditions.

In this section, three adjustments that improve the reliability and stability of the reconstruction process are presented.

Intensity Normalisation

The interaction of the X-ray beam with the sample leads to a certain intensity in the diffraction pattern. When scanning over an inhomogeneous sample the intensity changes according to the transmission of the sample area being illuminated. Due to the overlap of adjacent scan points the redundant information allows for the reconstruction of the object transmission function. Hereby, a constant probe intensity is assumed during the entire scan. If this is not the case, the ptychographic reconstruction algorithm is not able to distinguish whether the intensity variation was caused by a varying probe or by the structures in the object. During the data acquisition, the transmission diode, cf. Section 3.3.3, records the beam intensity upstream of the sample. This information is used to normalise the intensity of the diffraction patterns relative to each other within one dataset. To do so, all transmission diode values of the scan are scaled to 0 and 1, afterwards the corresponding

diffraction pattern is divided by the scaled transmission diode value.

Object Constraint

In general, any values are possible in the reconstructed object transmission. Physically, only values between 0 and 1 for the transmission and values between 0 and multiples of 2π for the phase shift are valid. If the solution for the object and probe function is not constraint at all, the ptychographic algorithm can choose their values freely in order to minimize the difference between the intensity distribution in the measured and calculated diffraction patterns. This result is not necessarily physically correct but rather another local minimum leading to convergence of the algorithm. Often, the intensity of the reconstructed probe function does not converge but decreases with a increasing object amplitude, which depicts a decreasing object transmission respectively an increasing object absorption. A restriction of the amplitude values of the object function to be smaller or equal than 1 is set in the end of each iteration. As a consequence, the intensity of the reconstructed probe function usually converges close to the real absolute value.

It is also possible to constrain the object phase shift to a certain interval. But since the phase shift is comparatively robust against intensity variations it does not improve the reconstruction result.

Probe Constraint

In order to assure quantitative values in the reconstructed object function, the probe function should be constraint to intensity values I_{in} of the incoming illumination. The intensity I_{in} is either measured by a diode upstream of the sample or it can be extracted from flat field diffraction patterns of the scan itself. Areas of flat field diffraction pattern do not contain any scattering from the structure of the object, even though there could be a homogeneous layer of material as long as its absorption (given by thickness and material) is known.

$$\mathcal{P}'_{\text{norm}}(\vec{r}) \quad = \quad \mathcal{P}'(\vec{r}) \cdot \sqrt{\frac{I_{\text{in}}}{|\mathcal{P}(\vec{r})|^2}} \tag{2.1.10}$$

The probe constraint in the form of normalising the probe intensity is done after the probe update in every iteration of the reconstruction. With this, usually no further constraints to the object are required to achieve reliable results.

2.1.7 Extension of the Basic Model

The basic ptychographic model assumes a fully coherent and constant probe $P(\vec{r})$ and an optically thin object $O(\vec{r})$. For real experimental data sets, some of these conditions might not be fulfilled. The sample can be thick and subject to vibrations. The Probe can be partially coherent and also vibrating. Various extensions and modifications of the ptychographic model are published such as the treatment of thick samples by multi-slicing[93], the correction of positioning errors[64] of the sample as well as multiple modes to handle a decoherent[99] or broad-bandwidth illumination[26].

At beamline P06 the illuminating probe can be considered fully coherent relative to the thin and weakly scattering samples. Nevertheless, other effects such as a shaking beam as well as sample drifts and vibrations may reduce the reconstruction quality. To correct these, the basic phase retrieval algorithm can be extended to an ensemble of probe modes. This extension considers a motion of the object relative to the probe during the exposure time of a single scan point. For each scan point $\Delta\vec{r_n}$, the transmission function equals a multiplication of the object and probe function:

$$\Psi_{n,\nu}(\vec{Q}) \quad = \quad \mathcal{F}\left[O(\vec{r}-\Delta\vec{r}_n)P(\vec{r}-\Delta\vec{r}_\nu)\right]. \tag{2.1.11}$$

For every scan position $\Delta\vec{r}_n$ the probe function $P(\vec{r})$ is the same but shifted to ν different positions $\vec{r}_\nu$. A density matrix $\rho_{n,\nu}$ weights the probe function at different positions and the ensemble can be different for each scan point since the motion of the object relative to the probe can be different for each scan point. According to this, the intensity $I_n(\vec{Q})$ in the nth diffraction pattern can be described by

$$I_n(\vec{Q}) \quad = \quad \sum_\nu \rho_{n,\nu}\left|\Psi_{n,\nu}(\vec{Q})\right|^2. \tag{2.1.12}$$

During the reconstruction process, the additional correction algorithm calculates the non-negative parameter $\rho_{n,\nu}$ using a least-squares method to minimize the cost function.

$$\left|I_n - \sum_\nu \rho_{n,\nu}|\Psi_{n,\nu}|^2\right|^2 \rightarrow \text{min} \tag{2.1.13}$$

Afterwards, the all members of the ensemble of probe modes and the object are updated and weighted by the optimised weight density $\rho_{n,\nu}$. This correction will be applied to the combined reconstruction of the catalyst model sample, in Section 4.2.3. Further details on the implementation of this extension to the ptychographic algorithm can be found in the publication by Schroer [2017].

This approach differs from the one published by Thibault and Menzel [2013], where multiple *different* probe modes $P_\nu(\vec{r})$ build an ensemble that is constant for all scan points.

2.2 Chemical Imaging

In materials science, the atomic structure and the morphology/shape of an object are ideally gathered at once to achieve complementary information.

In the previous section, the basics of the imaging part which provides the morphology for the analysis of nanomaterials were treated. Now, the basics of X-ray absorption spectroscopy which is used for chemical investigation in terms of elements and oxidation states are presented.

2.2.1 X-Ray Absorption Spectroscopy

The energy dependence of the atomic form factor due to the binding energies of the electrons to the atomic nucleus is element specific and enables to determine the chemical composition of a material by spectroscopic techniques. X-ray absorption spectroscopy (XAS) using synchrotron radiation is widely established to investigate the electronic, structural and magnetic properties of many kinds of samples, cf. Hippert et al. [2006].

According to the energy range measured around the absorption edge the resulting spectra are either part of the X-ray Absorption Near-Edge Structure[1] (XANES) or of the Extended X-ray Absorption Fine Structure (EXAFS). Fig. 2.2.1 shows the distinction in XANES and EXAFS range by the example of the palladium K-edge. In addition, the basic processes causing the typical appearance of the spectrum are illustrated.

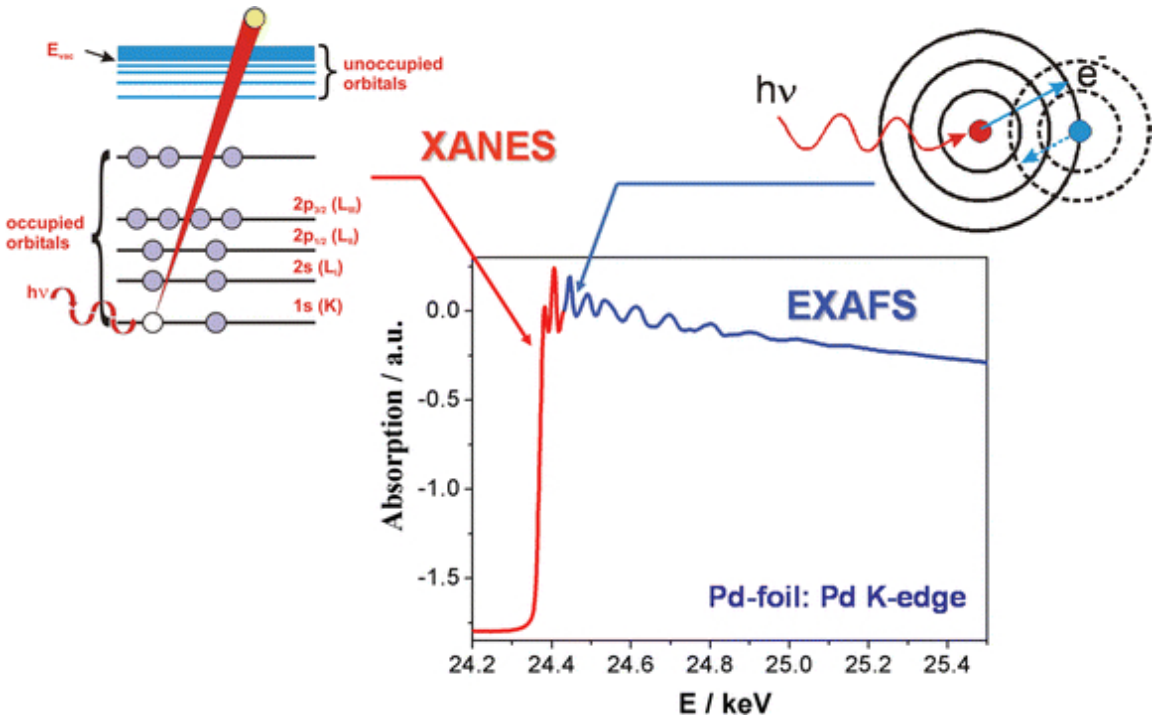

Figure 2.2.1: Scheme of X-ray absorption spectroscopy with the XANES and EXAFS regions. This scheme shows an example of X-ray absorption spectroscopy at the palladium K-edge. It illustrates the different energy ranges for the XANES and EXAFS regime and the corresponding photon-electron interaction. Drawing adopted from Grunwaldt and Baiker [2005].

XANES

A XANES spectrum covers the energy range from approximately $-50\,\mathrm{eV}$ to $200\,\mathrm{eV}$ around the edge energy. The shape of the absorption edge is correlated to the density of states that are available for the excitation of a photo electron. The density of states is affected by the binding geometry and the oxidation state of the atom with the transitions following FERMI's Golden Rule, cf. eq. 1.1.18. Thus the analysis of the XANES region in the absorption

[1] also known as NEXAFS – Near-Edge X-ray Absorption Fine Structure, mostly used in the soft X-ray regime, e.g. in Stöhr [1992].

spectrum gives information about the electronic properties of the absorbing atom, i.e., its current oxidation state and bindings[38]. A scheme of the absorption process is shown in the upper left side in Fig. 2.2.1.

In combination with full-field imaging or scanning imaging techniques such as scanning transmission X-ray microscopy (STXM)[105], XANES adds chemical contrast to spatially resolved images of the sample. For standard STXM, the sample is scanned perpendicularly to a confined beam, recording the intensity after the sample by a point detector. To obtain chemical contrast between different species, the scan is repeated at different energies around an absorption edge of an element of interest. Only this element will show a significant change in transmission as a function of energy.

For full-field chemical imaging the sample area of interest is entirely illuminated by the X-ray beam and instead of an intensity measurement using an ion chamber or PIN diode, a 2D detector such as a CCD camera as described in Section 3.3.1 is used to record the transmitted intensity distribution downstream of the sample. This measurement is repeated for different energies along an absorption edge resulting in an absorption spectrum in each pixel.

The spatial resolution of these two techniques is either limited by the resolution of X-ray optics (beam size) or by the effective pixel size of the detector. Detailed discussions of chemical imaging using X-ray microscopy technique were published by Grunwaldt and Schroer [2010] or Sakdinawat and Attwood [2010].

EXAFS

For EXAFS measurements, the energy-dependent absorption of the sample is measured up to approximately $1\,\mathrm{keV}$ above an absorption edge. These spectra show an oscillatory behaviour that originates from the scattering of the excited electrons by the neighbouring atoms. Thus, EXAFS gives information about the local atomic structure *around* the element of interest. A scheme of the scattering process of the outgoing electron is shown in the upper right side in Fig. 2.2.1. EXAFS measurement are usually not directly combined with imaging techniques to obtain spatially resolved mappings of the sample. However, the detailed analysis of the spectrum in reciprocal space reveals the distances between the atoms of the material giving access to the molecular structure with high spatial resolution[78].

2.2.2 Resonant Ptychography

Resonant ptychography combines the benefit of the high spatial resolution obtained by ptychography with the chemical contrast obtained by varying the photon energy as it is done in XANES measurements. In the previous chapter, the energy-dependent atomic form factor $f(\vec{Q},\omega)$ and the refractive index $n(\omega)$ were derived to describe the interaction of X-rays with matter. Whereas XAS measurements directly obtain the energy-dependent absorption by recording the intensity up- and downstream of the sample, ptychography records the intensity distribution downstream of the sample in 2D diffraction patterns. So how is the chemical information accessed by resonant ptychography?

The intensity distribution I_n in the diffraction patterns is proportional to the modulus

square of the structure factor $F(\vec{Q})$ given in Equation (1.1.23). Thus, the energy-dependent atomic form factor $f(\vec{Q}, E)$ respectively the refractive index $n(E)$ are also encoded in the diffraction patterns. The ptychographic scan is repeated for several energies E_k and, as described before, the ptychographic reconstruction yields the quantitative two-dimensional complex transmission function of the object $O(\vec{r}, E_k)$ that contains the absorption and phase shift of the sample. For each energy E_k, the reconstruction of the object function varies according to the absorption and phase shift of the material at this particular energy. Thus, each pixel of the reconstruction contains a discrete spectrum for the phase shift and the absorption of the object. Especially for weakly scattering objects, the object phase and the resonance effect in the phase shift is stronger than the absorption and the change in absorption. For example, a 100 nm thick layer of gold has a phase shift of approx. 130 mrad at a photon energy of 11 000 eV and the phase shift decreases about 20 % at the Au-L_3 edge at 11 920 eV. The absorption for the gold layer is about 2 % at 11 000 eV and it only increases by less than 2 % at the Au-L_3 edge. Therefore, the phase reconstructions are used for the further chemical analysis. Figure 2.2.2 illustrates the different steps of the resonant ptychography procedure. It starts with the acquisition of ptychographic data sets at different energies around an absorption edge. In a next step, the ptychographic reconstruction retrieves the complex transmission functions of the object at each energy. After further post-processing such as image alignment, the phase shift values in each pixel are extracted and can be compared to reference measurements.

A 2D ptychographic reconstruction is a projection of the sample along the optical axis. If the sample is not homogeneous, each pixel may contain a mixture of different materials and oxidation states. In order to find the chemical composition of the sample from the resonant phase shift in the reconstruction, reference measurements of the anticipated elements and oxidation states are required. These are gained from XANES or EXAFS measurement but still require a conversion to the phase shift which can be achieved by using the KRAMERS-KRONIG relation. This conversion is discussed in the following section.

2.2.3 Kramers-Kronig Calculations

From XAS measurements, the absorption coefficient μ is calculated from the ratio of the beam intensity before and after the sample, cf. Equation (1.1.38). μ provides access to the imaginary part β of the complex refractive index respectively to the imaginary part f_2 of the atomic scattering factor, cf. Equation (1.1.37). For direct comparison of the XAS measurement to the phase of a ptychographic reconstruction, the real part of the refractive index respectively the phase shift is desirable. Using the KRAMERS-KRONIG equations as given in Section 1.1.4.4, the real part of the scattering factor can be calculated from absorption spectra measured in an EXAFS or XANES experiment. For this conversion, the open source python-based software package called *kkcalc* by Watts [2014] was used. Here, its main principle is briefly explained.

According to Equation (1.1.42) the KRAMERS-KRONIG relation can be written in terms of the Henke[37] scattering factors as:

$$f_1(E) \quad = \quad Z^* - \frac{2}{\pi}\mathcal{C}\int_0^\infty \frac{\omega f_2(x)}{\omega^2 - E^2} d\omega, \tag{2.2.1}$$

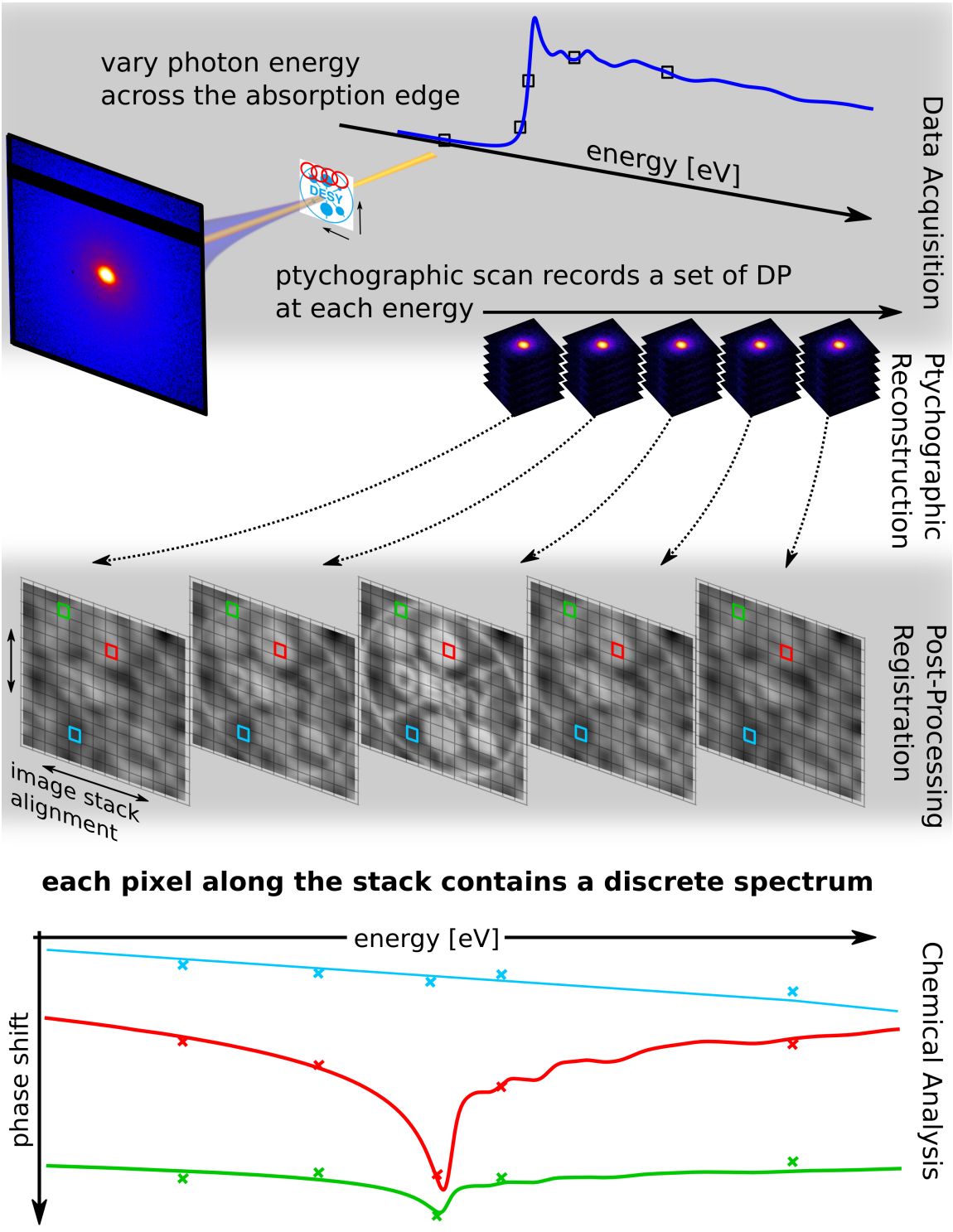

Figure 2.2.2: Resonant ptychography scheme. The ptychographic scan is repeated at several energies around an absorption edge. Each set of diffraction patterns is reconstructed separately. The phase reconstructions are aligned to each other resulting in an image stack as a function of energy. Each pixel contains a discrete spectrum along the stack. Depending on the sample material and thickness, the resonance effect is apparent in these spectra and the data points can be fitted by reference measurements.

where Z^* is the relativistic correction

$$Z^* = \sum_n s_n \left(Z_n - \left(\frac{Z_n}{82.5} \right)^{2.37} \right) \tag{2.2.2}$$

with Z_n and s_n as the atomic number and stoichiometric quantity of the nth element in the material. The software package *kkcalc* is based on an algorithm that calculates the KRAMERS-KRONIG transform of a given spectrum via a piecewise LAURENT polynomial method. Decomposing the data in piecewise polynomial functions circumvents the undefined points that are critical for the evaluation of the integral in Equation (2.2.1). As an extension of the algorithm that was used by Henke et al. [1993], *kkcalc* provides computationally cheap calculations with higher accuracy than other methods. At the same time, the requirements on the input data – a XANES or EXAFS spectrum – are modest as the data points can be spaced arbitrary and missing data points for energies between zero and infinity are covered by scattering factor data from the data base published by the Center for X-ray Optics[17] and from data by Biggs and Lighthill [1988]. *kkcalc* also offers the option "fix distortions" which is helpful to match the junction between measured data and data from the data base especially if the experimental data has an offset due to background or an uncalibrated energy dependence. Nevertheless, the better and the larger the measured XANES/EXAFS region, the better the measured data is adapted to the data from the data base resulting in a higher accuracy of the calculated real part.
After the real part f_1 of the scattering factor was computed from f_2 using *kkcalc*, the dispersive part δ and, assuming a certain thickness of the sample, the phase shift of the reference materials can be calculated using the Equations (1.1.36) and (1.1.41). Fig. 2.2.3 shows the graphical user interface during the conversion of experimental absorption data at the Pt-L_3 edge of a platinum foil to the real part of the scattering factor.

2.3 Image Alignment

The ptychographic reconstructions obtained at different energies require a good alignment relative to each other. Due to positioning errors, this is not a trivial task.

Image alignment is a wide field and various aspects such as feature-based versus intensity-based image registration, image transformation and sampling are discussed in the literature[61,66,110]. Especially, in the field of medical imaging many algorithms were developed and are well-established.

The general task to solve by an image alignment algorithm is to find a transformation $T(x)$ that spatially aligns a so-called moving image O_m to a fixed reference image O_f. Depending on the deformations between the reference image and the moving image, a suitable transformation model is chosen. Four of these transformation models are illustrated in Fig. 2.3.1 in the order of increasing flexibility.

Software Package – SimpleElastix

The alignment of the reconstructions of the samples that were investigated in this work, was done using the open-source software package *SimpleElastix* published by Marstal

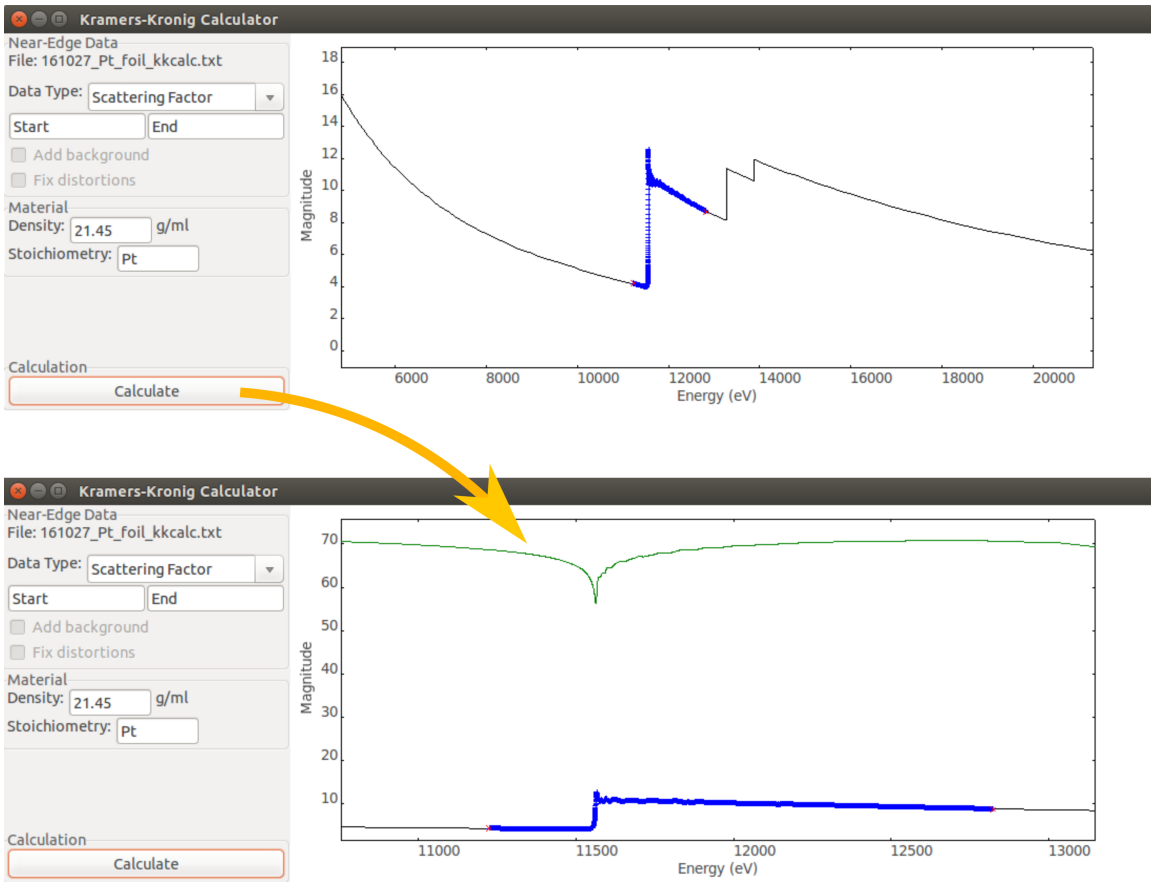

Figure 2.2.3: Screenshots of the graphic user interface (GUI) of the kkcalc software package. First, the experimental data, shown in blue was loaded and adapted to data from the data bases. With the information of the material density and the present components, the real part of the scattering factor is calculated (bottom in green).

et al. [2016] and Lowekamp et al. [2015]. SimpleElastix is an extension to the command-line, open-source package of the intensity-based image registration software called *elastix* [53,88]. These packages were developed in the framework of medical imaging. Both are well documented and all details can be found in the elastix manual [88] and in the web documentation of SimpleElastix [67]. SimpleElastix offers different transforms (rigid, affine, B-spline), different metrics as well as different optimizers and regularisation factors to optimize the alignment process for various types of deformation between images. It is beyond the scope of this work to discuss all options as well as their mathematical implementation and influence on the alignment process. Even though the software is relatively complex and offers many options to tune the alignment process, it is rather simple to implement into own scripts in different languages such as Python. Therefore, a brief overview of the actual alignment procedure is given here:

As a first step in the alignment process, all images are roughly registered by the rigid alignment tool *StackReg* [96] implemented in the java-based image processing program *imageJ* [80]. With this, the images are shifted and rotated, if applicable. As a result the object position matches for all reconstructions. Since each single reconstruction can be subject to distortions due to positioning errors and drifts during the scan, a simple rigid image

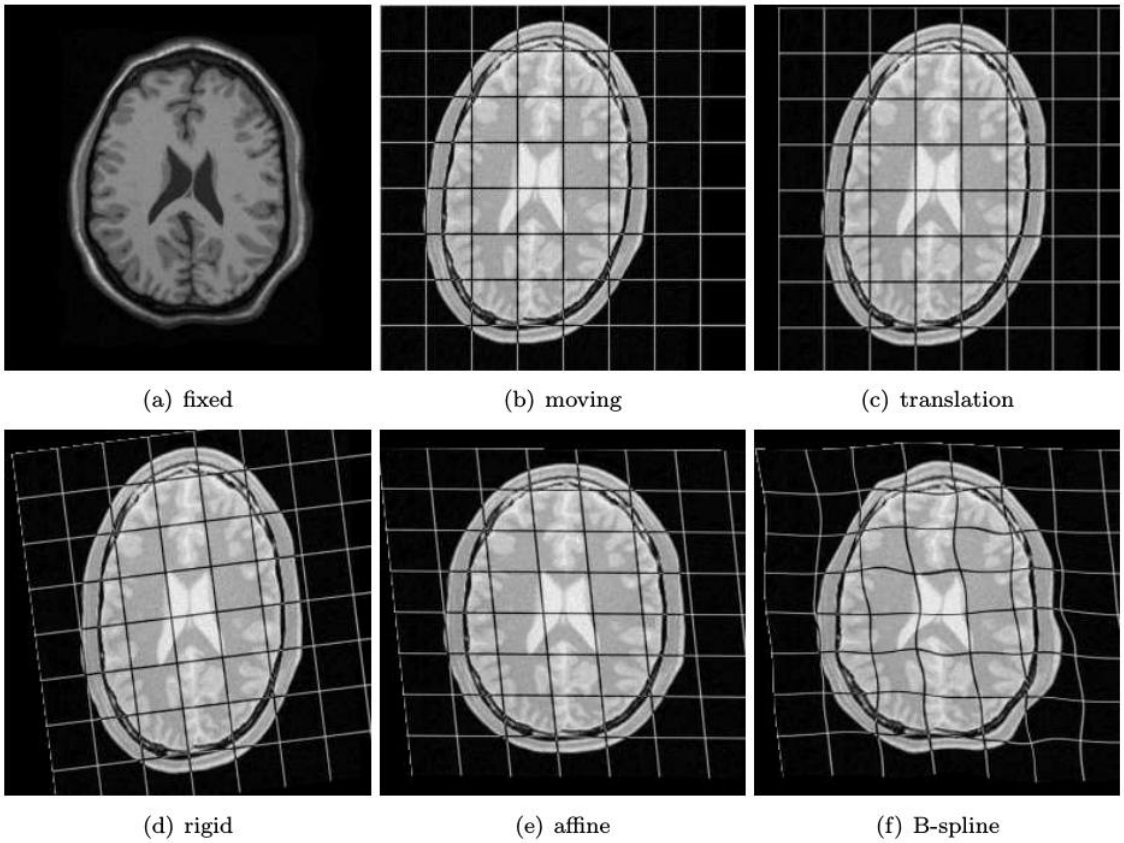

Figure 2.3.1: Different transformations for rigid and non-rigid image registration. a) shows the reference (fixed) image. b) shows the initial moving image with a grid overlay. c) shows the moving image after a translation transformation. d) shows the moving image after a rigid transformation as a combination of translation and rotation. e) shows the moving image after an additional affine transformation, where only parallel lines of the image grid are preserved. f) shows the moving image after a b-spline transformation that finally achieves a good match with reference image. Image was adopted from the manual of *elastix* by Klein and Staring [2015]

alignment, which simply moves the object, is not sufficient for the subsequent chemical analysis of the entire resonant data set. After the coarse alignment, SimpleElastix is used for affine and b-spline registration.

SimpleElastix provides groupwise alignment, where all images are aligned simultaneously. However, due to background variation and probably also due to the inevitable resonant phase shift variation, the simultaneous alignment of the entire stack of images resulted in artefacts such as vertices and an overall worse alignment than the successive alignment of one image after the other. Therefore, the successive registration will be performed using the average of the rigid-registered stack as fixed image . In a second step the affine transform is applied to the images with SimpleElastix. This transform does not only adjust the varying pixel size for the reconstructions at different energies, cf. Sec. 2.1.3, but also compensates slight drifts during the scan that caused distortion along one direction. In the final step, the b-spline transform was performed with SimpleElastix to correct all further distortion caused by positioning errors during the scan. Details on the parameters will be given in the

evaluation part in Chapter 4 Section 4.3 and a complete list is attached in the Appendix A.

2.4 Spatial Resolution and Contrast

Often, a precise measure of the resolution is desirable in order to compare the quality of different reconstructions. Since the spatial resolution of ptychography is not limited by the pixel or beam size, the resolution has to be determined in the reconstructions in the final analysis. The maximal spatial resolution is given by the highest scattering angle, where the signal of the sample is detected over noise and over background. The spatial resolution in one image can be different for different directions and different kinds of features. Therefore, it is difficult to determine the point spread function for the entire image. Numerous procedures either in the spatial or the frequency domain are more or less established in X-ray microscopy and two of these will be introduced in this section. The quality of an image is not purely determined by the spatial resolution, but also does the contrast or visibility play an important role in feature detection.

2.4.1 Edge Detection and Line-Spread-Function

The edge detection method displays the intensity variation at sharp features (lines and edges). Its derivation is the Line-Spread-Function (LSF) showing the intensity across a thin line in an image. As resolution parameters for these methods, usually the FWHM (for LSF) or the edge response between $10\,\%$ to $90\,\%$ of the total intensity are assumed[90]. Often, the major drawback of this simple but sound technique is the absence of sharp features for real nano-structured specimens. Since the spatial resolution is feature dependent, edge detection and LSF usually serve as an approximation of the spatial resolution for particular features. If the shape of an object, for example a sphere, is well known, a line plot should be deconvolved first to obtain a more realistic result.

2.4.2 FOURIER Ring Correlation

The estimation of the spatial resolution via the FOURIER ring correlation[2] has been adopted from electron microscopy[5]. For this method, two images of the same field of view are required to determine the spatial resolution. From the FOURIER transform of these two images, the normalised cross-correlation FRC_{12} is calculated.

$$\mathrm{FRC}_{12}(q_i) \quad = \quad \frac{\sum_{q\in q_i} F_1(q)\cdot F_2(q)^*}{\sqrt{\sum_{q\in q_i} F_1^2(q)\cdot \sum_{q\in q_i} F_2^2(q)}} \tag{2.4.1}$$

For ptychography, different options are eligible to get two images to correlate:

- One dataset is reconstructed twice using only every second scan point. Due to the high overlap, this usually succeeds, but with slightly reduced image quality.
- During the experiment the scan is repeated at the same sample position and with the same parameters.

[2] FOURIER shell correlation for 3-dimensional data

- Two slightly different dataset are used, e.g., at slightly different energies.

Physically, the FRC of the two images should decrease with an increasing q-value. In fact, background noise leads to artificial high frequency features in the reciprocal image, which can lead to a correlation curve that is increasing again after dropping and the resolution determination is not clear. In this case, a window function (GAUSSian, KAISER-BESSEL[55] etc.) is helpful to avoid these oscillations in the FRC. There are different cut-off criteria to determine the resolution having regard to distinct aspects. Referring to van Heel and Schatz [2005] the half-bit criterion is used in this work.

2.5 Diffraction Data Analysis

In ptychography, the spatial resolution and also the sensitivity to the phase shift of small features is inherently limited by the signal-to-noise in the diffraction patterns. Besides the unavoidable limitation in the signal-to-noise ratio due to the given shot noise, also background scattering occurs from incoherent scattering processes of the X-rays with air molecules, windows and the detector material itself. In this section, the two measures of data quality – the Signal-to-Noise Ratio (SNR) and the Signal-to-Background Ratio (SBR) – are introduced.

2.5.1 Signal-to-Noise Ratio

Regarding the photon flux, the information in the diffraction patterns is limited by POISSON statistics, which are defined as:

$$P_W(l) \quad = \quad \frac{W^l}{l!} \cdot e^{-W}, \tag{2.5.1}$$

where W is the expected value and l is the number of events. The standard deviation σ in the POISSON distribution is

$$\sigma \quad = \quad \sqrt{W} \tag{2.5.2}$$

Subsequently, the signal-to-noise ratio SNR for a diffraction pattern with the intensity distribution I as function of the scattering vector $\vec{q}$ subject to the POISSON statistics is generally defined by:

$$\mathrm{SNR} \quad = \quad \frac{I(\vec{q})}{\sqrt{I(\vec{q})}} = \frac{\text{mean intensity}}{\text{standard deviation}} \tag{2.5.3}$$

A limitation in the quality of the reconstructed images only due to the limited photon statistics is a best case scenario. In real measurements also parasitic scattering effects reduce the spatial resolution and phase shift sensitivity. All these effects are merged as background, which is defined in the following subsection.

2.5.2 Signal-to-Background Ratio

The background can be calculated from diffraction patterns of the *empty* beam, that is to say, a measurement where no sample was placed in the beam. In that case, all scattering recorded in the diffraction patterns is parasitic and does not contribute to the sample signal. In the following, such diffraction patterns will be refered to as flat field.

In this work, the Signal-to-Background Ratio SBR is defined as:

$$\mathrm{SBR}(\vec{q}) = \frac{\sqrt{\frac{1}{N}\sum_j^N \left(\mathrm{DP}_n(\vec{q}) - \overline{\mathrm{DP}}_{\mathrm{flat}}(\vec{q})\right)^2} - \sigma_{\mathrm{flat}}(\vec{q})}{\sigma_{\mathrm{flat}}(\vec{q})}, \tag{2.5.4}$$

where N is the total number of included diffraction patterns DP_n containing the scattering signal of a sample, $\overline{\mathrm{DP}}_{\mathrm{flat}}$ is the average and σ_{flat} is the standard deviation of the flat-field diffraction patterns. This kind of SBR calculates the variance between the diffraction patterns containing the signal scattered by the sample and the average background scattering. The square root of the variance depicts the signal in this definition, which leads to the form of a conventional signal-to-noise definition. The subtraction of σ_{flat} simply modifies the value when the signal cannot be distinguished from noise anymore from 1 to 0. The value of the scattering vector, when the SBR reaches 0 can be assumed as a marker for the highest spatial resolution that could be achieved in the ptychographic reconstruction.

The signal-to-background ratio is particularly useful to estimate the data quality for measurements under different experimental conditions such as using a beamstop. In Chapter 4, the SBR is used to discuss the enhancement in data quality for the catalyst model sample with an opaque beamstop, which is also published by Reinhardt et al. [2017].

3 Experimental Setup

The experiments were performed at the nanoprobe endstation of beamline P06[82] at the synchrotron radiation light source PETRA III, DESY, Hamburg. In this chapter, the devices and parameters directly relevant for the measurements analyzed in Chapter 4 will be discussed. Further details on synchrotron radiation theory, machine parameters and so on can be found in textbooks by Attwood [2007], Wiedemann [2003] and Baruchel [1994].

3.1 Beamline P06 at PETRA III

PETRA III is a third generation synchrotron radiation source with a ring energy of $6\,\mathrm{GeV}$. It is usually operated in top-up mode of $\pm 1\,\mathrm{mA}$ for a ring current of $100\,\mathrm{mA}$. For the beamline P06, a $2\,\mathrm{m}$ long undulator serves as insertion device, it can be tuned in the range of $3\,\mathrm{keV}$ to $100\,\mathrm{keV}$. In the optics hutch of the beamline, three different monochromators – a multi-layer, a double-crystal SI-111 and a channel-cut – can be used separately to vary the energy[1]. The double-crystal and the channel-cut silicon monochromators were used for the coherent imaging experiments of this work. Both have an energy bandwidth of $1 \times 10^{-4}\,\mathrm{dE/E}$.

Further components are available in the optics hutch such as pre-focusing lenses to adapt the coherence length to the entrance aperture of different nano-focusing optics depending on the experiment. Furthermore, higher-order reflecting mirrors are installed downstream of the monochromator. Three different layers – silicon, chrome and platinum – are available. Depending on the cut-off energy desired for a particular experiment, one of these layers can be moved into the beam to suppress the higher-order harmonics of the X-ray beam by making use of the energy-dependent and angle-dependent total external reflection of X-rays.

At the beamline P06, two experimental stations are available for different experimental purposes. The microprobe endstation offers high photon flux of up to $1 \times 10^{11}\,\mathrm{Ph/s}$ with an entrance aperture of the KB mirrors for beamsizes from micrometers down to approximately $300\,\mathrm{nm}$. the nanoprobe setup provides a highly-focused beam down to a size of about $50\,\mathrm{nm}$, but with a lower flux in the range of $1 \times 10^{7}\,\mathrm{Ph/s}$ to $1 \times 10^{9}\,\mathrm{Ph/s}$. The nanoprobe endstation[82] of beamline P06 is about $100\,\mathrm{m}$ away from the undulator source and offers a highly coherent beam. The experimental setup is optimised for (coherent) scanning imaging techniques like ptychography and is usually operated at photon energies in the range of $5\,\mathrm{keV}$ to $25\,\mathrm{keV}$. A set of high-precision step and piezoelectric motors provides the degrees of freedom required for 2D and 3D imaging experiments with nano-scale resolution.

Even though the beamline operates in the hard X-ray regime an evacuated or Helium filled flight tube is available to clear the beam path between the sample and the detector.

[1] The exact energy range depends on the monochromator that is used.

Figure 3.1.1 illustrates the setup as it was used for the experiments of this work[2]. The focusing optics and relevant detectors are briefly described in the following.

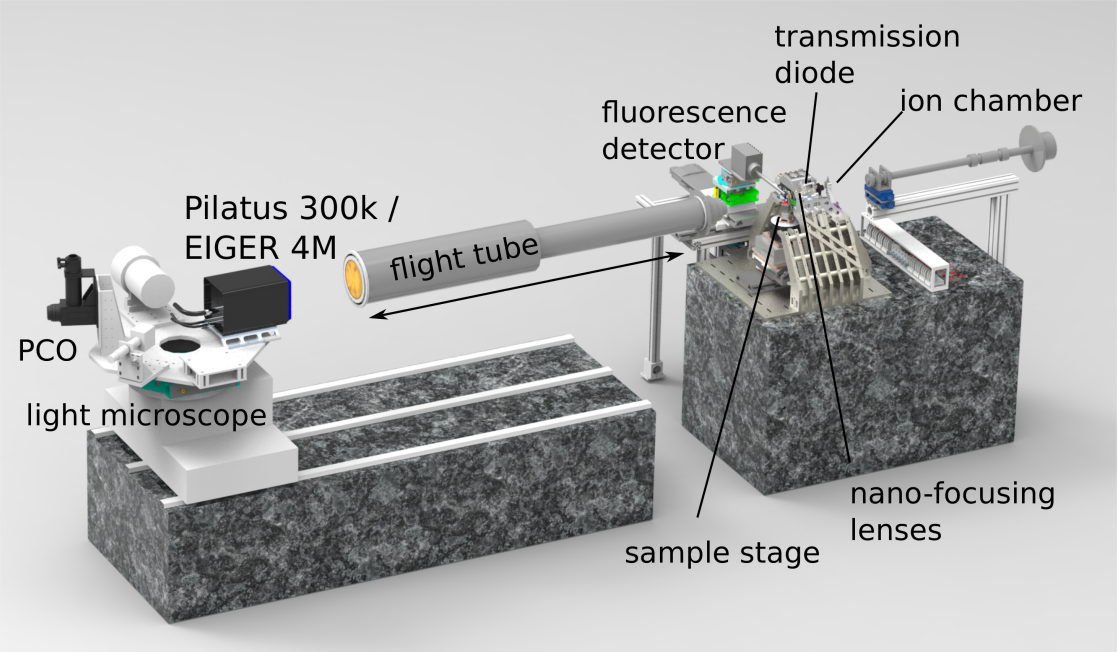

Figure 3.1.1: Drawing of the P06 nanoprobe setup. The detector table on the left carries various detectors and offers 4 degrees of freedom to adapt different experimental conditions. A movable flight tube can be installed to clear the beam path, especially when working at lower photon energies (<15 keV). The granite on the right carries the sample and lenses stages as well as the fluorescence detector, the transmission diode and the ion chamber. Courtesy: H. Lindemann

3.2 Focusing Optics

To achieve a defined nanobeam, different kinds of focusing optics are used depending on the photon energy that is required for the experiment. In the hard X-ray regime above 10 keV refractive lenses[59,60] made of silicon are typically used. For focusing in the tender X-ray regime below 10 keV Frensel zone plates are available[29]. In the experiments of this work, discussed in Chapter 4, refractive lenses were used within an energy range between 11 keV to 12 keV. The focusing length f_0 of a refractive lenses using the thin lens approximation is calculated by

$$f_0 = \frac{R}{2\delta N} \tag{3.2.1}$$

where R is the curvature radius of lens, δ is the refractive index of the lens material and N is the number of lenses. As the lens gets thicker, the principal plane H is shifted to H_2 respectively to H_1, cf. Figure 3.2.1, and the focal length $f_2 = f_{\text{thick lens}}$ is calculated as

[2]The nanoprobe setup was being re-designed during the time of this work in 2016, please refer to the beamlines web site for the latest setup.

follows:

$$f_{\text{thick lens}} = f_0 \frac{1}{1 - (1/6)(L/f_0)} \tag{3.2.2}$$

This equation is a simplification, a full description can be found in the references below. For the evaluation of this work, the energy-dependence of the focus is relevant. When changing the photon energy, the focal length changes concomitantly due to the energy dependence of the refractive index. Therefore, during the resonant experiments, the sample position relative to the focal spot changes. Since the depth of focus is in the range of 200 µm and the divergence of the beam focused by refractive lenses is about 1 mrad this is generally not influencing the data quality if the energy changes in the range of 100 eV.

A pair of a vertical and a horizontal lens must be aligned perpendicular to each other and to the beam in order to produce a Gaussian shaped focus. Without pre-focusing this nano beam is considered to be fully coherent. For a detailed discussion on X-ray optics, please refer to the publications by Lengeler et al. [1999a], Schroer et al. [2001] and Seiboth et al. [2014] or the textbooks, e.g., by Hecht [2002] and Träger [2012],

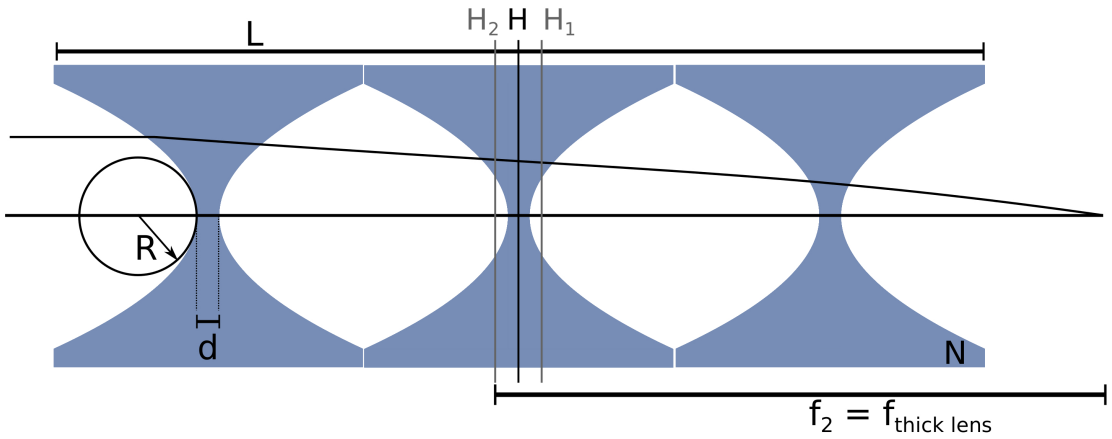

Figure 3.2.1: Focusing scheme of refractive X-ray lenses. For a thick lens the principal plane H is shifted to H_2 respectively to H_1.

3.3 Detectors

A set of different detectors is available at the nanoprobe setup. Each of them providing a different contrast or serving a different purpose during the measurements. In this section, all detectors that were involved in the measurements of this work are briefly described together with some comments on certain properties influencing the data.

3.3.1 X-ray Camera

The high-resolution X-ray camera is based on a thin single-crystal scintillator transforming the incident X-rays into visible light that is imaged onto a CCD chip through a visible light microscope optic. The light microscope comes with 3 different lenses for different magnification of 2x, 4x and 10x or 20x and is manufactured by OptiquePeter[74]. The CCD

chip is part of a PCO4000 camera[75] with a pixel size of $9\,\mu m \times 9\,\mu m$, a sensitive area of $36\,mm \times 24\,mm$ and a digital range of $14\,bit$. The combination of these components allows for full-field X-ray microscopy with a high spatial resolution down to an effective pixel size of $180\,nm$. For ptychography experiments, the X-ray camera is used for the initial lens alignment as described below in the standard experimental procedure, step 2.

3.3.2 Light Microscope

An optical microscope, Keyence VH-Z100UR[49], is used for the initial coarse sample alignment. It is mounted on the detector table with 4 degrees of freedom. The working distance is $25\,mm$ and the reproducibility of the microscope position is given by the precision of the motors of the detector table and is better than $5\,\mu m$. The microscope carries a zoom lens offering a $100\,x$ to $1000\,x$ magnification with a maximum resolution of $1\,\mu m$.

3.3.3 PIN Diode

For the measurements of the intensity of the photon flux, PIN diodes are used. The incident X-rays generate electron-hole pairs and the induced current is measured by a highly sensitive Keithley-6487[95] pico ammeter. This ammeter averages the incoming signal over a time interval of $300\,ms$ and automatically adapts its internal gain to the photon flux.

Transmission Diode

The transmission diode manufactured by Hamamatsu [2017] works similar to the standard PIN diode, but its detection material in the active area is as thin as $5\,\mu m$. Because of that, this diode can be used in transmission mode to measure the incident photon flux upstream of the sample without loosing a significant amount of intensity. Due to the geometry of the experimental setup, the transmission diode is not placed directly upstream of the sample but upstream of the lenses and downstream of the slits. Because of this, the intensity measurements for the incoming beam do not take into account the absorption of the lenses, but relative changes of the intensity can be tracked. Since the detection volume of the transmission diode is reduced, the measurements of this diode are less precise than the ones of the standard PIN diode. Detailed studies on the calibration of the transmission diode ascertained that the transmission diode behaves linearly as a function of flux. Besides this regular performance, the transmission diode is highly sensitive to sudden changes of the beam intensity of more than $2\,\%$, even if it operates in its linear range. Even though the ring current of PETRA III is usually in top-up mode, cf. Section 3.1, irregular beam intensity variations can occur. In the absence of a better alternative, the transmission diode had to be used for normalisation of the diffraction patterns.

3.3.4 Fluorescence Detector

The emission of X-rays of a characteristic energy after an atom was ionised by high-energetic radiation is called X-ray fluorescence. Since the energy of the X-ray fluorescence

photons is element-specific, this technique is used for chemical analysis for almost all kinds of matter. A detailed description of the physical process and its applications can be found in the textbooks by Lachance and Claisse [1995] or Beckhoff et al. [2007].

In the nanoprobe setup, a silicon drift detector Vortex®-EM manufactured by Hitachi High-Technologies [2017] is used. The energy-dispersive fluorescence detector determines the energy of the incoming X-ray fluorescence photons with an energy resolution of approximately 150 eV. Thus, it can be used for direct investigation of the elemental distribution of a sample. The fluorescence detector plays an important role for the ptychography experiment concerning the search of interesting sample areas during the fine adjustment. Additionally, the fluorescence detector is used to track the sample position during tomography or resonant scans to check that the desired sample area stays in field of view.

3.3.5 Photon Counting Detectors

In the hard X-ray regime, the latest detector technology offers fast and efficient single photon counting detectors providing high-quality data without read-out noise.

Table 3.3.1: Parameters photon counting detectors EIGER 4M vs. Pilatus 300k

Parameter	EIGER 4M	Pilatus 300k
Sensitive area (width x height) mm^2	233.2×245.2	83.8×106.5
Pixel size [μm^2]	75×75	172×172
Total number of pixels	$2070 \times 2167 = 4\,485\,690$	$487 \times 619 = 301\,453$
Gap width (hor./vert.) [px]	10/37	-/17
Maximum frame rate [Hz]	750	20
Readout time	continuous readout, 3 µs dead time	0.95 ms
Point-spread function	1 px	1 px
Sensor thickness	450 µm	450 µm
Maximum count rate [$Ph/s/mm^2$]	5×10^8	1×10^7
Counter bit depth [bit]	12	20
Data format	HDF5/NeXus	edf/tiff

Pilatus 300k

The diffraction patterns of the catalyst model sample, cf. Section 4.2, including the Siemens star reference measurements were recorded by a Pilatus 300k detector[21]. The parameters are listed in Table 3.3.1

EIGER 4M

For the experiment of the Pt Bubble in Section 4.3 the EIGER 4M detector[20] was used. Especially, the larger dynamic range and the smaller pixel size are advantageous for coherent diffraction experiment at beamline P06, where the propagation distance was limited to only 2.1 m.

3.4 Opaque Beamstop

An opaque beamstop can be used for high-resolution ptychography in order to reduce background scattering effects from any material downstream of the sample, including air scattering and the scattering by the detector material itself. In comparison to a semi-transparent beamstop, an opaque beamstop is intransparent to X-rays with the intention to absorb the central beam completely. Figure 3.4.1 illustrates the influence of a beamstop on the scattering information in the diffraction patterns.

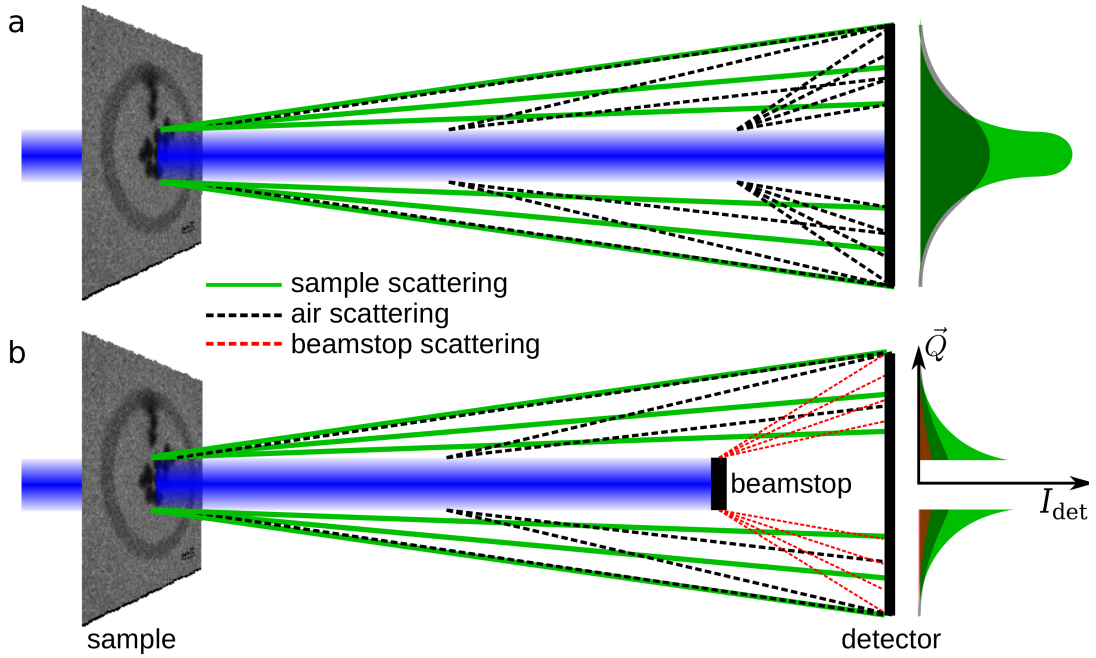

Figure 3.4.1: Scheme of the effect on the background scattering when using an opaque beamstop. a) schematically shows the scattering distribution of the background and the sample scattering for the conventional setup without beamstop. For larger scattering angles $\vec{Q}$, the scattering signal of the sample (green) is covered by background scattering (gray). In b) the background scattering is suppressed and the sample signal emerges, but eventually parasitic scattering from the beamstop itself (red) occurs in the diffraction patterns. The low-frequency information is missing.

The dimension and position of a beamstop should be adapted to the specific experimental conditions regarding the beam size, the photon flux and the scattering strength of the sample. The beamstop that was implemented during the experiments analysed in Section 4.2 was made of steel, had with a length of approximately $10\,\mathrm{mm}$, and a diameter of $1.5\,\mathrm{mm}$. It was placed into the central beam about $500\,\mathrm{mm}$ upstream of the detector. In the last $500\,\mathrm{mm}$ of the air path near the detector, more than $90\,\%$ of the air scattering are generated. In this way, it is possible to suppress the major part of air scattering as well as background scattering by the detector material under feasible experimental conditions, i.e., a macroscopic beamstop which is almost scatterless and can be mounted with high stability. About 3σ of the approximately GAUSSian shaped central beam were covered and the maximal count rate of the central beam was reduced by a factor of 10^5. Accordingly, the beamstop can be considered as fully absorbing.

3.5 General Experimental Procedure

The process of a ptychographic experiment can be generalised by the following 5 steps:

1. **Choosing the photon energy and calibration of the monochromator:**
   The scientific question determines the photon energy for the experiment, either depending on the sample material (for chemical contrast) or on the best possible beam conditions (focus size, flux etc.), usually it is a compromise of both. In the beginning of an experiment, the monochromator is tuned to the required energy. If the energy must be known very precisely – as it is the case for resonant measurements – a reference XANES measurement is performed.

2. **Optics alignment:**
   Afterwards, optics that are suitable for the chosen photon energy are aligned with the help of the PCO X-ray camera. One stack of refractive lenses only focuses in one dimension, a point focus is achieved by aligning two stacks perpendicular and with the correct lens-to-lens distance to each other.

3. **Finding the focus and determining the beam properties:**
   The standard X-ray chart – the Siemens star – is used to find the focus position after the lens alignment. The first approximation is done by a knife-edge scan. For knife edge scans, a crossed vertical and horizontal $50\,\mu m$ gold wire is scanned perpendicularly to the beam at different positions along the beam. The focus position is indicated by the steepest slope in intensity. Afterwards a ptychographic scan is recorded. The reconstruction provides the probe function in the sample plane, that is propagated to find the focal position. Eventually, the lens alignment will be refined, if the probe propagation shows a misalignment of the vertical and the horizontal focus. Finally, the focal position is adapted with the light microscope, so it can be used to put all following samples directly to the focal spot.

4. **Finer sample alignment using the fluorescence/transmission detector:**
   The actual sample is placed in the focal plane with the help of the light microscope. The spatial resolution of this microscope is limited to $1\,\mu m$, therefore the fluorescence detector and/or the PIN diode are used for the finer sample alignment until the region of interest is found.

5. **Recording ptychographic data sets:**
   After these 4 steps the actual measurements start by recording ptychograms of desired regions of the sample. For the first data sets, the scan parameters are slightly tuned in terms of step size and exposure time per scan point. If required, a beamstop is installed and aligned in the setup to minimize parasitic scattering effects. When the results of the ptychographic reconstruction match the expectation, the measurement is eventually extended to 3D measurement by recording data sets at different projection angles (tomography) or at different energies (resonant ptychography). If the sample is changed during a beamtime, the experimental procedure is repeated beginning at step 4.

4 Samples – from the Test Pattern to Model and Real Samples

Since this work focuses on the further development of resonant ptychography for chemical imaging of weakly scattering objects such as catalyst particles, the reliability of the ptychographic reconstruction for quantitative analysis must first be proven. To achieve this, well-defined experimental conditions were created: On the one hand, the exact specifications of the experimental setup, e.g., the X-ray beam properties, as well as their influence on the reconstruction algorithm must be ascertained. This was accomplished by measuring a standard resolution chart, the so called Siemens star, in advance of subsequent experiments. The analysis of the Siemens star and the discussion of the most-suitable reconstruction parameters are presented first in Section 4.1.

On the other hand, a well-known weakly scattering model sample, which nonetheless represents realistic specimens, was required. The complete analysis of such a model sample including the pre-characterization by electron microscopy, the resonant ptychographic experiment with and without a beamstop as well as the ptychographic reconstructions resulting in chemical imaging are described in Section 4.2.

In a next step, resonant ptychography was applied to a real sample, cf. Section 4.3 demonstrating the possibilities for chemical imaging with hard X-rays.

4.1 Siemens Star Reference

For the ptychographic reference measurements, the standard resolution evaluation chart for X-ray analysis manufactured by NTT-AT[73] (Model: ATN/XRESO-50HC) was used. It is a $500\,\mathrm{nm}$ thick tantalum layer containing multiple structures of different sizes in the nanometer range. The circular inner structure, the so-called Siemens star shown in green in Fig. 4.1.1, consists of various rings of lines that narrow to a common center. The inner ring is composed of smallest structures of $50\,\mathrm{nm}$ lines and spaces. Due to its sharp features and the relatively thick tantalum layer, the Siemens star is a strongly scattering sample, compared to real catalyst samples. Therefore, this test pattern is dedicated to reference measurements in order to determine the optimal reconstruction parameters mostly depending on the experimental setup and not being limited by the sample.

The actual experiments of the model sample, cf. Section 4.2, were performed around the gold L_3 edge at $11.919\,\mathrm{keV}$ as well as at the platinum L_3 edge at $11.564\,\mathrm{keV}$. Therefore, the Siemens star was also measured at these two energies and reference values of the phase shift and the transmission of the X-rays for a tantalum layer of $500\,\mathrm{nm}$ thickness were calculated beforehand. At the energy of $11.564\,\mathrm{keV}$ the phase shift of tantalum is about $552\,\mathrm{mrad}$ and transmission is about $83.2\,\%$. At the energy of $11.919\,\mathrm{keV}$, the phase shift is

about 547 mrad and the transmission is about 82.6 %. The unusual decrease in the X-ray transmission with the increased photon energy from the platinum to the gold L_3 is based on the jump in transmission due to the tantalum L_1 absorption edge at 11.682 keV. For direct comparison of the reconstruction results in the next sections, an approximate value of 550 mrad for the phase shift and 83 % transmission should be kept in mind.

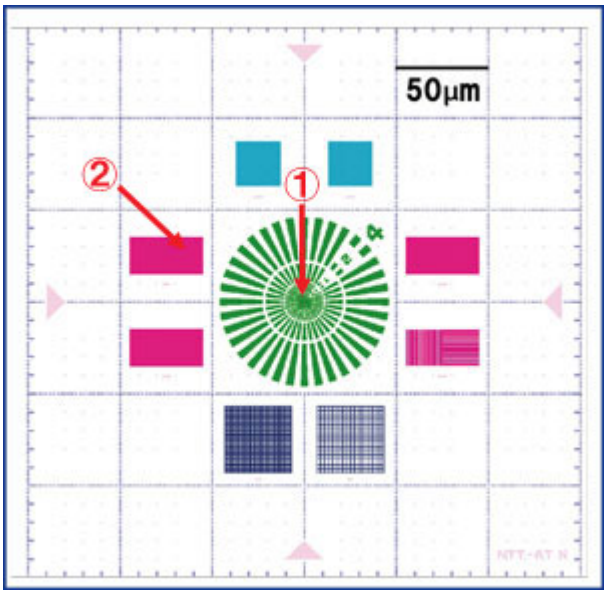

Figure 4.1.1: Scheme of the resolution chart *Siemens star* by NTT-AT. The marker (1) in the center points out the smallest structures of 50 nm lines and spaces, which were scanned for the reference ptychograms.

4.1.1 Experimental Parameters

Following the general experimental procedure described in Section 3.5, first, the photon energy was tuned to the gold L_3 absorption edge at 11.92 keV. After the optics alignment, knife edge scans as well as some test ptychography scans, the actual ptychography measurements of the *Siemens* star test pattern were performed with the scan parameters listed in table 4.1.1.

Table 4.1.1: Basic scan parameters: Siemens Star

Parameter	
Dwell time per scan point	0.5 s
Scan area (h x v)	2 µm × 2 µm
Number of steps (h x v)	50 × 50
Step size	40 nm
Photon flux in focus	2.48×10^7 Ph/s

Afterwards, the reconstruction of this data set was conducted using the ePIE algorithm, cf. Section 2.1.1, implemented in python.

4.1.2 Ptychographic Reconstruction

In Section 2.1.6, additional constraints to the object as well as to the probe function during the reconstruction process were discussed. Here, these constraints will be applied after the basic reconstruction. Based on this, it will be shown which procedure achieves the best results and will consequently be used for the following reconstructions of the model sample later on. Independent of the reconstruction parameters and constraints, the diffraction patterns were normalised using the transmission diode values to correct the intensity fluctuations of the initial beam.

(i) Basic Reconstruction

The results of a basic reconstruction without further modifications, i.e., no further constraints neither to the object nor to the illumination function are shown in figure 4.1.2a and 4.1.2b. After about 10 iterations, the error function converged and further improvement of the reconstruction was not expected. In a reliable reconstruction process, the probe intensity should also converge. Instead, in this case, the intensity of the reconstructed illumination decreased with the number of iterations and did not converge. This indicates that the algorithm could not extract the correct intensity distribution of the object and the probe when only using the total intensity in the diffraction patterns. With a decreasing probe intensity the object transmission cannot be properly reconstructed. After 100 iterations of this basic reconstruction, leaving all degrees of freedom to the algorithm, the transmission values of the sample are arbitrary due to the incorrect intensity of the reconstructed illumination. The reconstructed phase shift of about $400\,\mathrm{mrad}$ is about $150\,\mathrm{mrad}$ lower than the expected value. The reconstructed values for the phase shift and the transmission of the object were determined with the help of the histograms shown in Fig. 4.1.5. Under the assumption, that the Siemens star pattern is a binary object, the difference between the peaks of the highest and lowest values in the histograms of the reconstructed field of view reveals the average phase shift or transmission, respectively.

(ii) Amplitude Constraint Reconstruction

By setting a constraint to the amplitude of the object function – forcing the transmission of the object to be no larger than unity – the probe intensity converges as fast as the error function , cf. Fig. 4.1.2d. Nevertheless, the quantity of the ptychographic reconstruction still suffers from the degree of freedom in adjusting both, the probe intensity as well as the transmission of the sample. In this case, the reconstructed phase shift of tantalum is again too low with a value of about $410\,\mathrm{mrad}$. The probe intensity of about $2.2 \times 10^7\,\mathrm{Ph/s}$ is still incorrect, in this case it is too low. This leads to a shift in the object transmission to higher values. Since values higher than 1 are cut off due to the object constraint, the resulting object transmission of about $93\,\%$ is incorrect. According to that, the reconstruction algorithm was not able to find the true values only from the experimental data input without further constraints to the probe intensity.

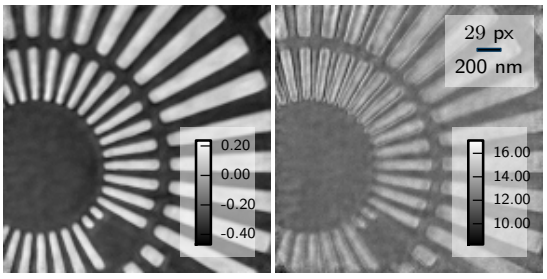

(a) Reconstruction of the object phase (left) and object amplitude (right) without constraints.

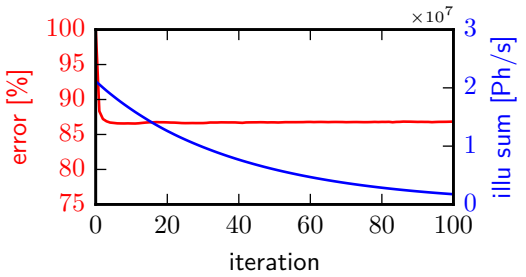

(b) Without constraints, the probe intensity does not converge.

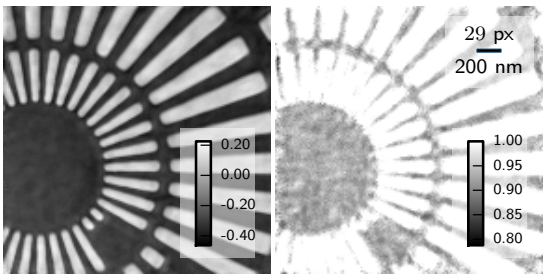

(c) Due to the object constraint, values larger than 1 are cut in the object amplitude.

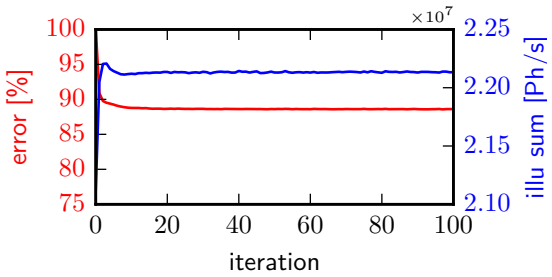

(d) With the object constraint, the probe intensity converges to a value of about 2.2×10^7 Ph/s

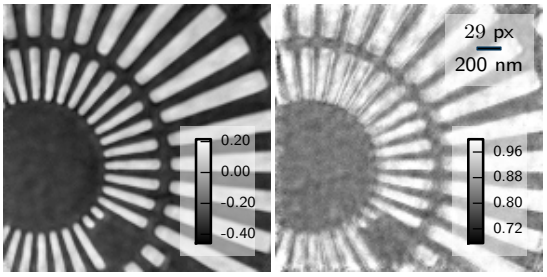

(e) Due to the object constraint, values larger than 1 are still cut in the object amplitude, but because of the correct probe intensity the amplitude reconstruction is more realistic.

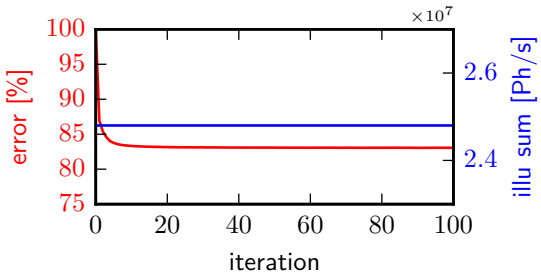

(f) Besides the object constraint, the probe intensity is constraint to value of about 2.48×10^7 Ph/s

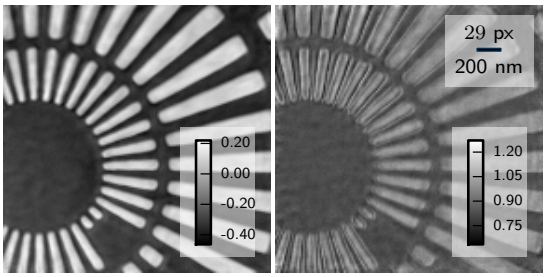

(g) The probe constraint leads to the best reconstruction results without the need of an object constraint.

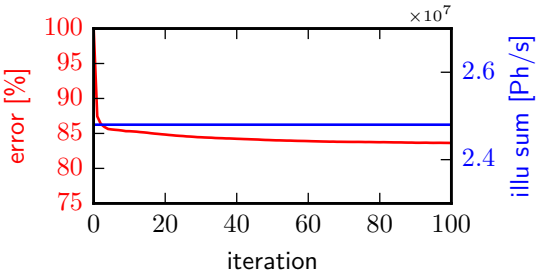

(h) The probe intensity is constraint to value of about 2.48×10^7 Ph/s. Without the object constraint the error converges to the lowest value compared to the previous reconstructions.

Figure 4.1.2: Comparison of the different reconstructions of the Siemens star at the Au-L_3 edge with and without constraints. Whereas the phase reconstruction are almost identical for different constraints, clear differences are visible in the transmission reconstruction.

(iii) Amplitude and Probe Constraint Reconstruction

The intensity in the diffraction patterns from scan points in the flat area of the inner part of the Siemens star was used to constrain the probe function. In addition, the absorption by the 500 nm thick tantalum layer as well as the absorption of the air path were considered. Based on that, the algorithm should find an incident probe intensity of 2.48×10^7 Ph/s. The probe intensity was constrained to this value during the reconstruction. The result of this reconstruction performed with a constraint to both, the object and the probe is shown in Fig. 4.1.2e and Fig. 4.1.2f. Here, the object phase shift and transmission values are about 410 mrad and 83.7 %, respectively, cf. red curves in Fig. 4.1.5. At least the absorption matches the expected value for 500 nm of tantalum.

(iv) Probe Constraint Reconstruction

Finally, the constraint to the object amplitude was turned off and only the constraint to the probe function was set during the reconstruction. This reconstruction converged to a result comparable to the previous one, cf. Fig 4.1.2g and 4.1.2h. The resulting phase shift and transmission values for the object function are 410 mrad and 83.7 %, respectively, cf. turquoise curves in Fig. 4.1.5. The transmission matches with the expected value, indicating the correctness of the given probe intensity. The discrepancy between the expected and reconstructed phase shift cannot completely be explained. One reason could be that the Siemens star sample is thinner than specified by the manufacturer. A phase shift of 410 mrad corresponds to a thickness of approximately 380 nm, which in turn matches with a transmission of 86.4 %

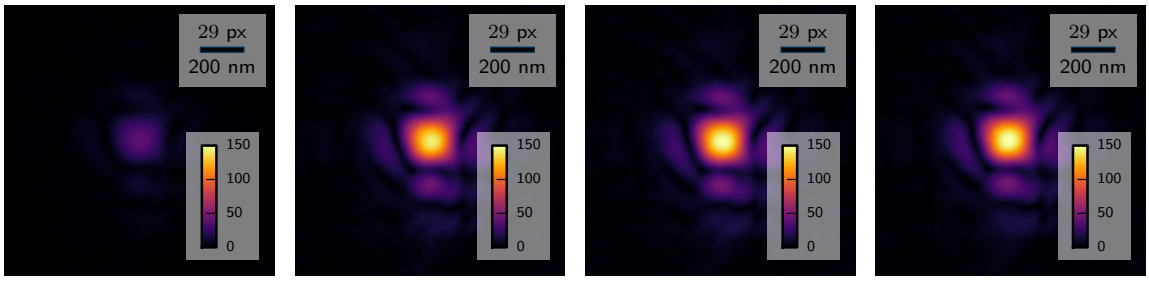

(a) Without constraints **(b)** object constraint **(c)** object and probe contraints. **(d)** probe constraint

Figure 4.1.3: Comparison of the amplitude of the reconstructed probe functions for the Siemens star with and without constraint to object and probe. The intensity of the probe function is not properly reconstructed without the constraints to the object or probe.

In Fig. 4.1.3, the reconstructed probe function of all four cases is shown for comparison. Whereas the intensity of the probe varies, the shape of the amplitude and the phase wavefront are identical. The focus size and focal plane were determined from the reconstruction where only the probe constraint was applied and they will be used as reference markers for the actual experiment of the model sample later on. The full-width-half-maximum lateral size of the amplitude of the illuminating beam in the sample plane is approximately 190 nm $\times$ 180 nm (h x v).

As a last measurement of the Siemens star, the ptychographic scan was repeated at the Pt-L_3 edge to check the beam conditions at this energy. The reconstruction was performed with the probe constraint and, here, the size of the reconstructed probe amplitude is increased to 520 nm × 720 nm (h x v), which is still small enough for the given experimental geometry and the algorithm converged resulting in a reliable reconstruction shown in Fig. 4.1.4. The reconstructed phase shift of 400 mrad still varies from the value of 552 mrad for the phase shift and the reconstructed transmission of 82.9 % matches the theoretical values for the transmission of 500 nm tantalum at 11 564 eV of about 83.2 %.

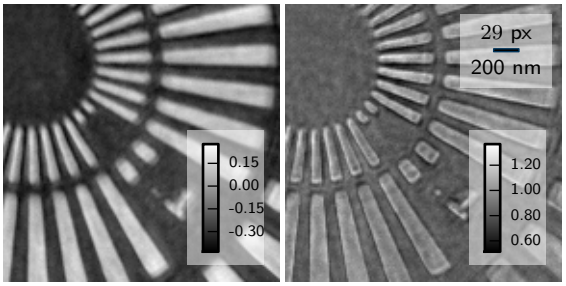

(a) Reconstruction of the object phase (left) and object amplitude (right) using the probe constraint.

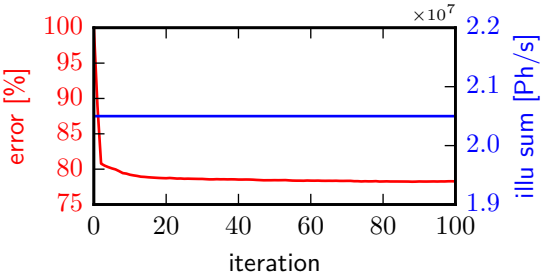

(b) The error function converges as fast as for the reconstructions at the Au-L_3 edge. The incoming probe intensity is constraint to about 2.05 Ph/s

Figure 4.1.4: Siemensstar reconstruction at the Pt-L_3 edge at 11 564 eV

4.1.3 Conclusion

In order to directly compare the influence of the different constraints on the transmission and phase shift values, the histograms of the phase and the amplitude for the different reconstructions are plotted in Fig. 4.1.5. It is apparent, that the phase shift values are mostly unaffected when the intensity of the illumination or the object constraint are changed, cf. Fig. 4.1.5a. On the contrary, the object transmission, cf. Fig. 4.1.5b, is very sensitive to these parameters: When there is no constraint applied, neither to the object nor to the probe, the absorption values are not quantitative at all, as indicated the blue curve. Solely applying an amplitude constraint leads to a cut-off and a wrong intensity distribution, cf. the green curve. The red curve stands for a reconstruction, where the probe intensity was set to a value of about 2.48×10^7 Ph/s and the amplitude of the object was constraint to be no larger than unity. Finally, the turquoise curve indicates the realistic absorption values. Here, the probe intensity was constraint to 2.48×10^7 Ph/s and the object amplitude was left free for reconstruction.

In order to achieve correct quantitative values for the complex transmission function of the object and the probe, it was important to constrain the intensity of the illumination to the real value. This was done by using the intensity in the diffraction patterns of scan points on homogeneous areas of the sample considering the absorption of the tantalum layer at the given energy.

After this discussion of the different constraints and their influence on the reconstruction,

the ptychography experiment of the catalyst model sample will be presented in the following.

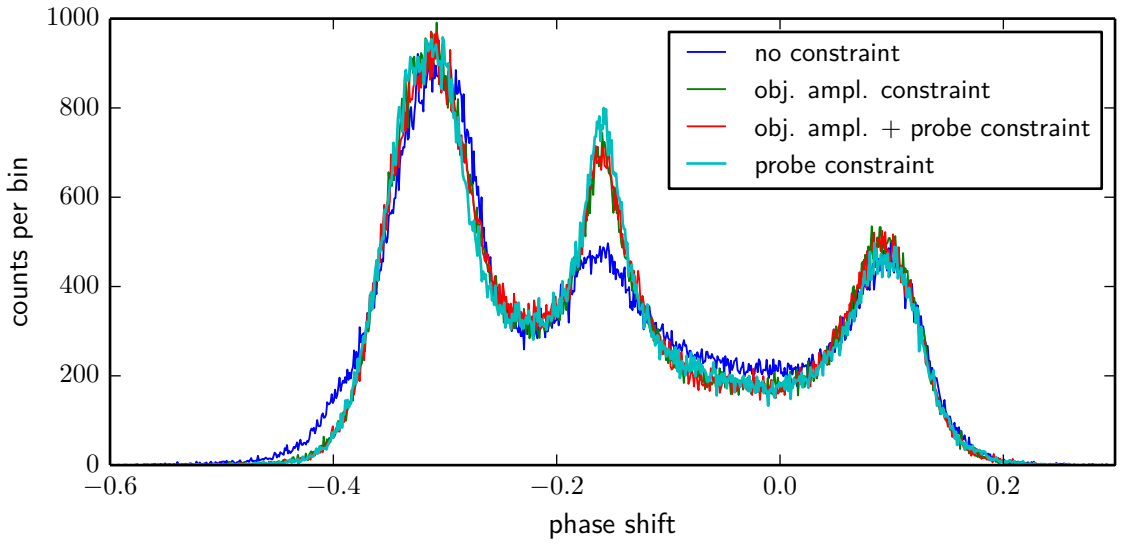

(a) Histograms of the phase reconstructions.

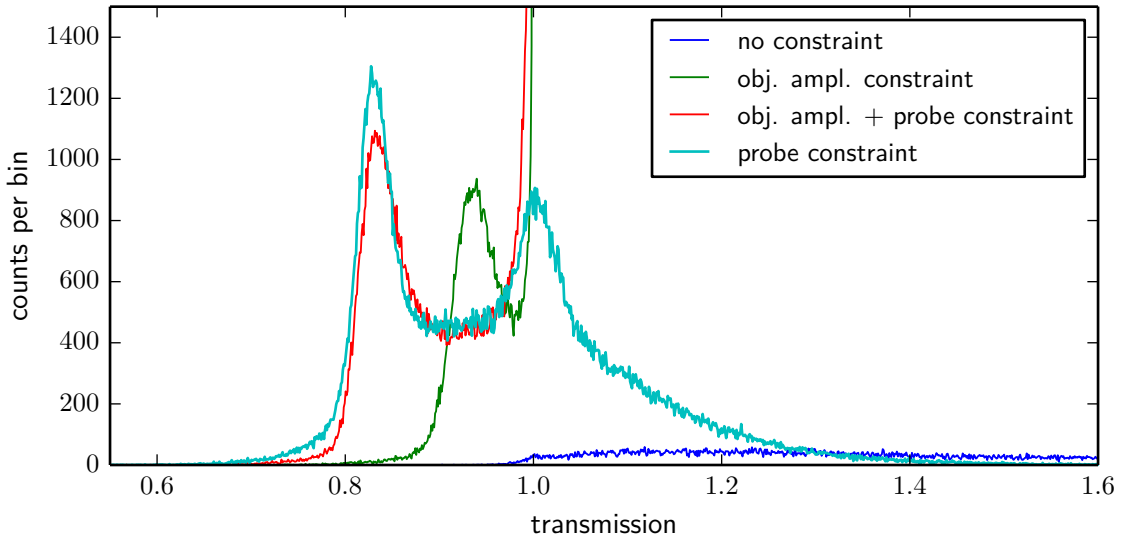

(b) Histograms of the amplitude reconstructions.

Figure 4.1.5: Histograms to check the phase and absorption values in the reconstructions. a) The phase shift remains almost unaffected when different constraints are applied. b) In contrast, the transmission clearly shows differences for each constraint.

4.2 Catalyst Model Sample

Chemical imaging of catalysts is one of the main applications for resonant ptychography. Since catalysts often have heterogeneous structures and features ranging on the lower nanometer scale, it is important to explore the current capabilities as well as the limitations of the method using a weakly scattering model sample with properties close to realistic conditions. A well-known sample is indispensable for the development and critical analysis of a rather new methodology like resonant ptychography especially at the detection limit. The model sample serves to understand the processes and potential sources of errors, since discrepancies between the theoretical expectation and the measured/reconstructed data can be assigned to the imaging technique and do not depend on unknown variations of the sample. The catalytic model sample at hand contains gold, platinum and palladium nanoparticles of different shapes and of different sizes in the range of less than 10 nm to 100 nm. Thus, it is a model sample with weakly scattering features and different materials relevant to catalysis, which actualises prospective real samples of that kind.

4.2.1 Sample Preparation and Characterisation

For the preparation of the model sample, colloidal nanoparticles, i.e., platinum and palladium buffered in acetone and also gold dissolved in water were used. The diameters of these particles range from less than $10\,\mathrm{nm}$ to about $100\,\mathrm{nm}$. After mixing the three different solutions in a glass vial, a single μL droplet of the mixture was deposited on the plasma-cleaned Si_3N_4 membrane of a TEM chip. The chip diameter is about $3\,\mathrm{mm}$, the silicon wafer contains 9 windows (eight windows of $100\,\mu\mathrm{m} \times 100\,\mu\mathrm{m}$ and one of $100\,\mu\mathrm{m} \times 350\,\mu\mathrm{m}$ size) just covered by the $20\,\mathrm{nm}$ thick Si_3N_4 membrane. Plasma cleaning allowed for fast spreading of the particles all over the TEM windows. The sample dried at room temperature under infra-red light. Further details of the sample preparation are described in the dissertation by Hofmann [2015].

In a next step, the TEM chips were analysed using a scanning electron microscope (SEM). Since the nanoparticles are arranged randomly in many clusters of different sizes and chemical distribution, the TEM windows were analysed by SEM and EDX (energy - dispersive X-ray spectroscopy) to find several suitable clusters. An ideal cluster contains all three materials equally distributed and is preferably located close to an edge of a Si_3N_4 window to assure fast and simple locating of the cluster during the X-ray experiment. Fig. 4.2.1 shows scanning electron micrographs of the sample at different magnification in backscattering contrast (SEM). From the additional energy-dispersive X-ray spectroscopy during the electron microscopy analysis, we obtained a rough elemental distribution, shown on the right in Fig.4.2.1. Different colors stand for the different materials: red – gold, blue – platinum and green – palladium. Although the energy resolution of the EDX measurements is low it served as the reference for chemical imaging with X-ray ptychography. It is very likely that smaller particles of all materials have diffused and are finally also deposited on bigger spherical objects of a different material. Thus a material mixture could be present in the projections.

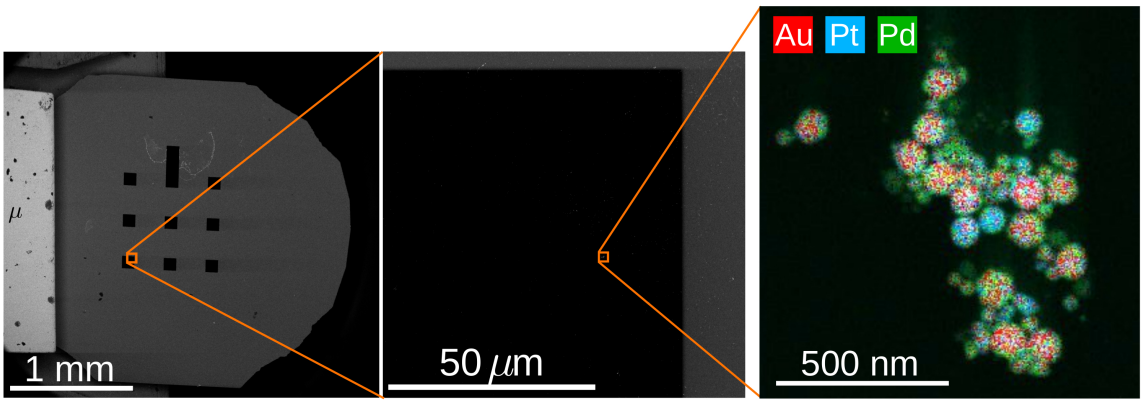

Figure 4.2.1: SEM image of the catalyst model sample. The left image shows the entire TEM chip with 9 windows. In the middle, one of the windows is zoomed. Finally, in the right image, a cluster of nanoparticles of different elements is visible. Additional EDX information unravels the elemental distribution.

4.2.2 Experimental Parameters

According to the common experimental procedure described in Section 3.5, the sample was roughly positioned in the focused beam with the help of the light microscope. The fluorescence contrast (not shown here) was used for a finer sample positioning and it also provided an overview of the sample when the diffraction data is collected. All ptychography scans of the model sample were performed with the scan parameters listed in Table 4.2.1.

Table 4.2.1: Basic scan parameters: catalyst model mample

Parameter	
Dwell time per scan point (A)	0.3 s
Dwell time per scan point (B)	3.0 s
Scan area (h x v)	1 µm × 1 µm
Number of steps (h x v)	20 × 20
Step size	50 nm
Sample-detector distance	2.08 m
Photon flux	$\approx 2.5 \times 10^7$ Ph/s

A full high-resolution data set consists of two ptychographic scans: Scan A with short exposure and without a beamstop (BS) and scan B with longer exposure and with the opaque beamstop implemented, cf. Section 3.4. These two scans were recorded one after the other. The total scan duration for one scan without beamstop was less than 4 min and for a scan with beamstop about 23 min. At each scan point of the square grid, a far-field diffraction pattern was recorded with the *Pilatus 300k* pixel detector positioned 2.08 m away from the sample in transmission geometry. Each ptychography measurement of the two scans was repeated in the same sample area at multiple energies around the Pt-L_3 and Au-L_3 absorption edge.

4.2.3 Ptychographic Reconstruction

In following subsections, the reconstruction of the conventional data set without beamstop will be described first. Afterwards, the combined reconstruction of the two data sets with and without beamstop will be presented. In both cases, the results for several modifications in terms of additional constraints, multiple probe modes and position correction are discussed.

Reconstruction of the Data without Beamstop

For the reconstruction, the diffraction patterns were cropped[1] to $180\,\mathrm{px} \times 180\,\mathrm{px}$ resulting in a pixel size in the reconstructed images of $\approx 7\,\mathrm{nm}$, cf. Equation (2.1.9). The pixel size slightly varies between $7.21\,\mathrm{nm}$ and $6.98\,\mathrm{nm}$ depending on the photon energy in the range of $11\,500\,\mathrm{eV}$ to $11\,933\,\mathrm{eV}$ between the L_3 edges of platinum and gold. The intensity in the diffraction patterns is normalised to the transmission diode data and the intensity update is applied without further modifications followed by the subsequent probe and object update as described in Section 2.1.1 steps 3 to 5. Similar to the procedure applied for the *Siemens* star reference, at first, a standard reconstruction with a single object and single probe mode was performed. Afterwards, the object and probe constraint were turned on separately as well as in combination.

The results for the different reconstructions after 300 iterations are shown in Fig. 4.2.2. In each phase reconstruction, single spherical particles down to a size of about $40\,\mathrm{nm}$ in diameter can be resolved individually, nevertheless the reconstruction quality differs regarding the reliability of the quantitative values for the probe intensity and the object transmission. As it was shown for the Siemens star reference measurements, the algorithm does not necessarily reconstruct the correct values for the transmission and phase shift of the object, because of the uncertainty in the intensity of the incoming illumination. Without further constraints, the probe intensity is increasing with the number of iterations. When only the object constraint was applied, the reconstructed probe intensity of $2.386 \times 10^7\,\mathrm{Ph/s}$ matches the real probe intensity of $2.392 \times 10^7\,\mathrm{Ph/s}$ already much better compared to the *Siemens* star reconstruction. For the model sample, the empty regions[2] over several scan points support the algorithm to properly adapt the probe intensity. In the best case, which is the reconstruction with the probe constraint only, the error function converged towards $83\,\%$ of the initial error.

The lateral size of the illuminating probe in the sample plane is about $130\,\mathrm{nm}$. As it is shown in Fig 4.2.3, the shape and size of the reconstructed probe are equal for the different reconstructions and they are also similar to the ones obtained from the *Siemens* star reconstruction, compare Fig. 4.1.3. Variations are due to a different position of the sample along the beam direction. As depicted in Fig. 4.2.4, which shows the propagation of the reconstructed probe, the difference between the *Siemens* star and the model sample at the Au-L_3 absorption edge is approximately $300\,\mu\mathrm{m}$. For the measurements at the Pt-L_3

[1] According to the highest scattering angles, cf. Section 4.2.6, a cropping of $N_{\mathrm{Det}} = 180\,\mathrm{px}$ is sufficient, if not the optimal choice. In terms of processing time, no significant change was noted in comparison to 2^n crop sizes, which are optimal for the computation of the fast FOURIER transform.

[2] Diffraction patterns in this area do not contain any sample scattering and serve as flat-field diffraction patterns.

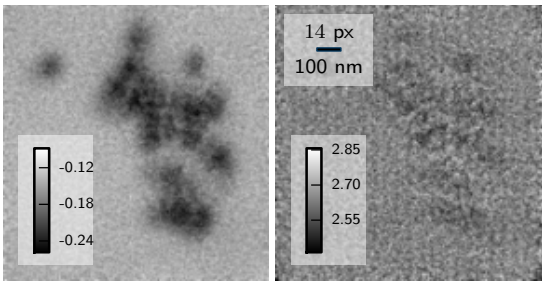

(a) Phase and amplitude reconstruction without constraints

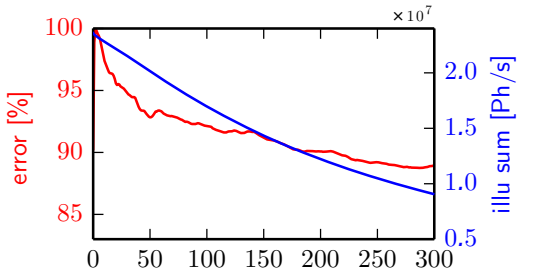

(b) The probe function does not converge without constraints.

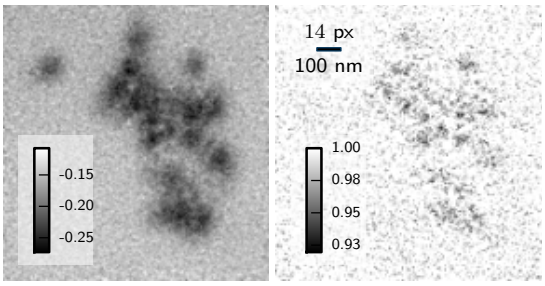

(c) Phase and amplitude reconstruction with object constraint

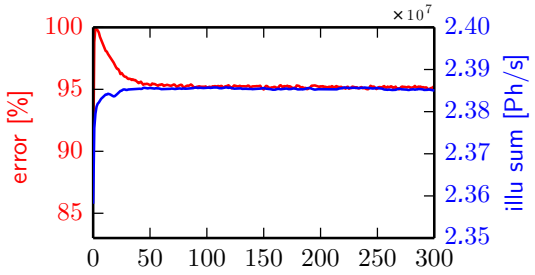

(d) With the object constraint, the probe function converges.

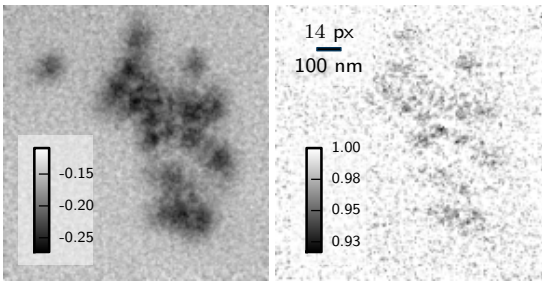

(e) Phase and amplitude reconstruction with object and probe constraint.

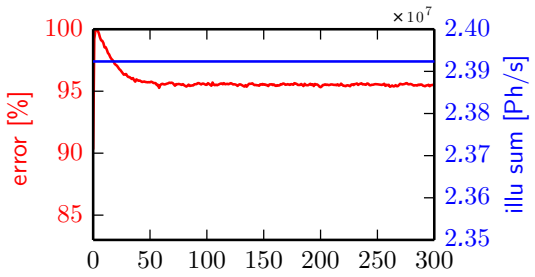

(f) With the object and probe constraint, error function converges quickly.

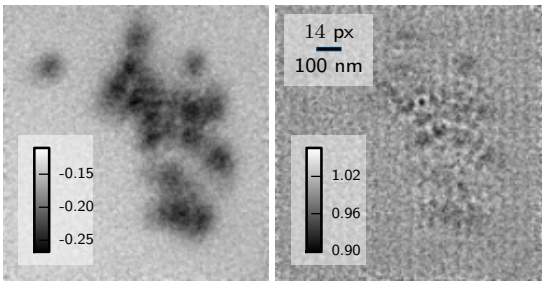

(g) Phase and amplitude reconstruction with probe constraint.

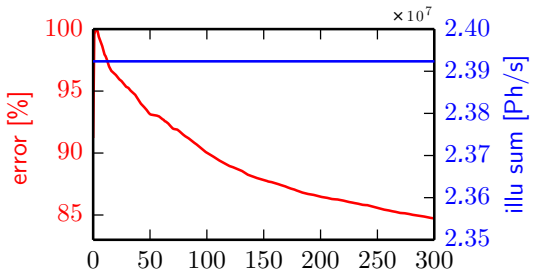

(h) By only applying the probe constraint, the error function converges slower but to lower values.

Figure 4.2.2: Comparison of the reconstructions of the catalyst model sample for different constraints without beamstop. Similar to the *Siemens* star reconstruction does the phase reconstruction remain almost identical for different constraints, whereas clear differences are visible in the transmission reconstruction.

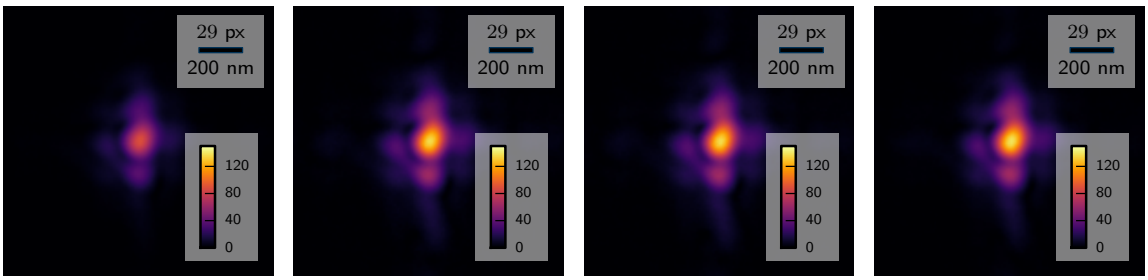

(a) Without constraints **(b)** object constraint **(c)** object and probe contraints. **(d)** probe constraint

Figure 4.2.3: Comparison of the amplitude of the reconstructed probe functions for the data set without beamstop. a) - d) show the probe reconstructions under different conditions with and without constraint to object and/or probe for the catalyst model sample.

edge around 11 564 eV the focal distance of the refractive lenses decreased about 1.1 mm due to the higher refraction power of the lenses at lower energies. In order to keep similar beam properties during the ptychography measurements compared to the measurement at the Au-L_3 edge, the sample was moved 1.1 mm upstream. During the ptychographic scans at one absorption edge, the focal length changes only slightly within the depth of focus, so that the sample position was not adapted to the photon energy.

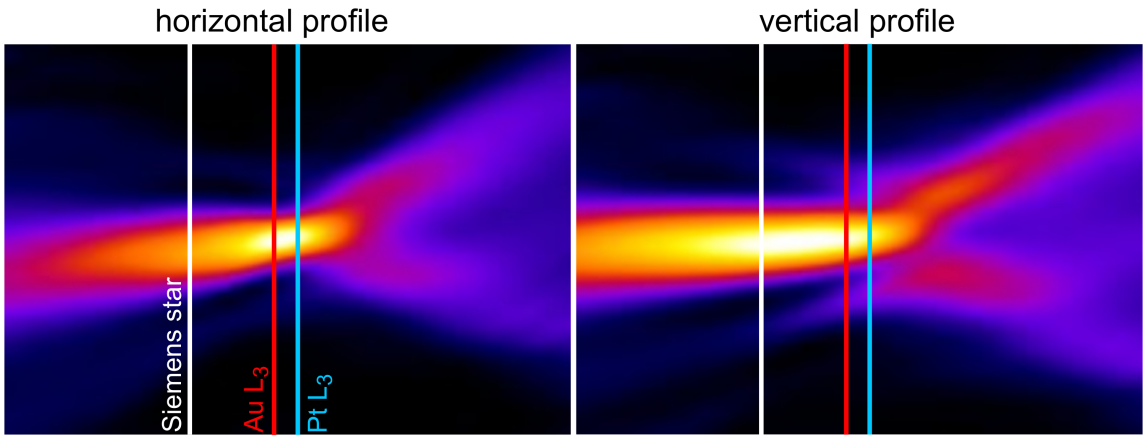

Figure 4.2.4: Propagation of the reconstructed probe. Here, the horizontal and vertical beam profile are shown together with markers for the sample position along the optical axis during the measurement of the Siemens star as well as during the measurements of the catalyst model sample at the Pt-L_3 and the Au-L_3 edge.

Combined Reconstruction of the Data without/with Beamstop

In the next step, the ptychographic data set with the beamstop was additionally used for the reconstruction process. A combined reconstruction was performed processing both data sets without beamstop (scan A) and with beamstop (scan B) simultaneously. While scan A (without beamstop) provides the low-q information in the diffraction patterns – albeit with a lower signal yield for higher angles – the diffraction patterns in scan B (with beamstop) provide the high-q information, however, they lack the low-q data behind the

beamstop. In order to consider all frequency regions, complementary masks were created: In the diffraction patterns of scan B, the pixels behind and in the immediate vicinity of the beamstop were masked to be freely adjusted by the algorithm. A complementary mask was applied to scan A. In this way, low-q information comes from scan A – assuring the correct phase shift offset – while the scattering information of smallest structures at higher q is provided by scan B. As a result, the complex transmission function of the object was quantitatively recovered, but with significantly increased sensitivity and spatial resolution compared to the reconstruction that solely used the data set without beamstop. Several

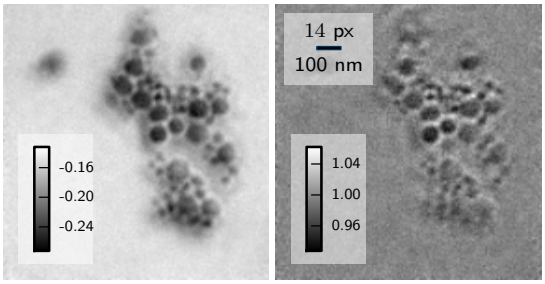

(a) phase and amplitude reconstruction, both data sets combined – shared object and shared probe

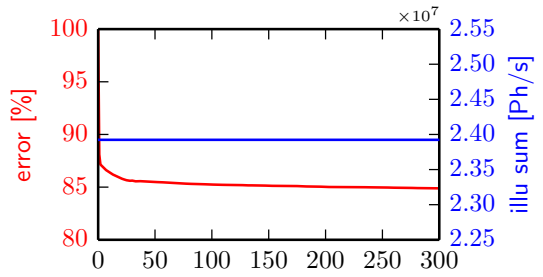

(b) Error and probe function when both data sets are combined – shared object and shared probe

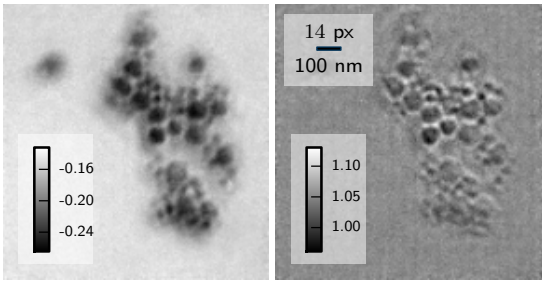

(c) phase and amplitude reconstruction, both data sets combined– shared object and two separated probes

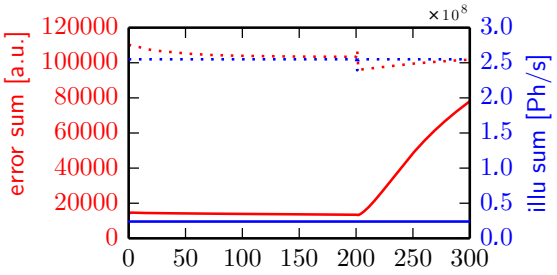

(d) Error and probe function when both data sets are combined – shared object and two separated probes

Figure 4.2.5: Comparison of the combined reconstruction using either a single shared probe function (a)+(b) or one probe function for each data set (c)+(d).

types of reconstruction were tested regarding the use of shared/multiple object and probe modes. Only the two versions with the best results are shown here. Whereas using two different probe functions – one for each data set – does not require any normalisation in terms of different exposure times between the two scans, using a shared illumination function for both scans involves exposure time normalization of the diffraction patterns. A direct comparison of the two different reconstructions in Fig 4.2.5 shows very similar results.

The shadows around the spheres in the combined reconstruction correlate with the drift between the two scans that was also observed in the fluorescence maps (not shown). Even the multiple probe reconstruction, see Fig. 4.2.5c, using one probe for each scan cannot solve this artefact. Consequently, in both cases, further correction of positioning errors was required. In Fig. 4.2.6, the reconstructions of two separate probes are compared with a

shared probe.

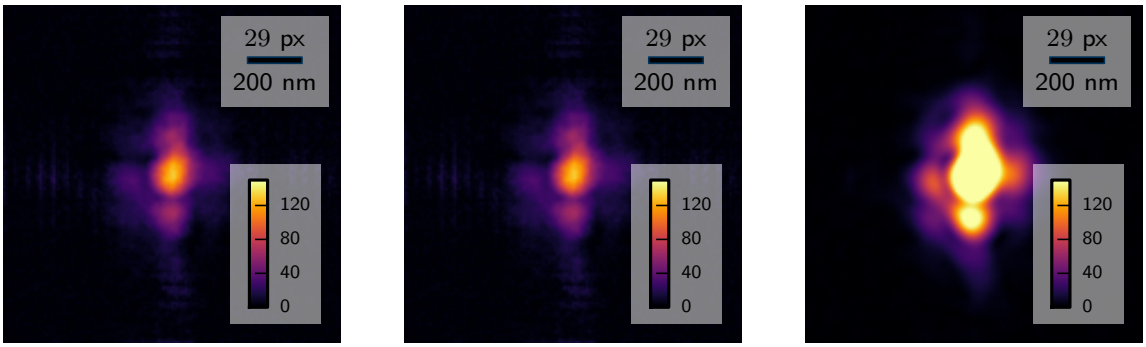

(a) amplitude of the reconstructed shared probe for the combination of both data sets

(b) amplitude of the reconstructed probe for the data set without beamstop

(c) amplitude of the reconstructed probe for the data set with beamstop

Figure 4.2.6: Comparison of the amplitudes of the probe reconstructions for shared or separate probes using the probe constraint

In the following, only the combined shared-probe shared-object reconstruction will be discussed further, since the behaviour of the error sum and the probe intensity is more physical during the reconstruction process.

Correction of Positioning Errors and Drifts

Although the image quality of the combined reconstructions is significantly increased, artefacts in particular positioning errors became obvious when the reconstructions of the different energies were aligned. In fact, the reconstructions should only differ in the phase and transmission values of the object. Instead, also the shape of the reconstructed object changes, which prevents a decent alignment and subsequently impedes the chemical imaging procedure. The variation in shape occurs due to incorrect positioning and drifts during the scan. This problem can be solved by using the position correction algorithm based on building up an ensemble of probe modes to find the correct position of the diffraction patterns in the scan. A detailed description of the algorithm was given in the Methods Chapter in Section 2.1.7. Here, the final reconstruction result as well as the average variation of the positions in the scan are presented after 200 iterations of the ensemble correction procedure. In Fig. 4.2.7, the image quality of the reconstruction is obviously improved. To achieve this tremendous improvement, the object and probe function of the conventional combined reconstruction, cf. Fig. 4.2.6a, were used as the initial object and probe function for the correction algorithm. The shadows around the spheres that were present in the combined reconstruction in Figure 4.2.5a are eliminated resulting in a clear reconstruction of the phase and transmission. In fact, the object transmission is reconstructed so well that even the difference between two elements can be seen at a glance albeit with lower resolution and a higher noise level compared to the object phase. The red circles in the zoomed area of the phase reconstruction indicate features of about 15 nm to 20 nm.

During the ptychographic measurement, the step size from one scan point to the next

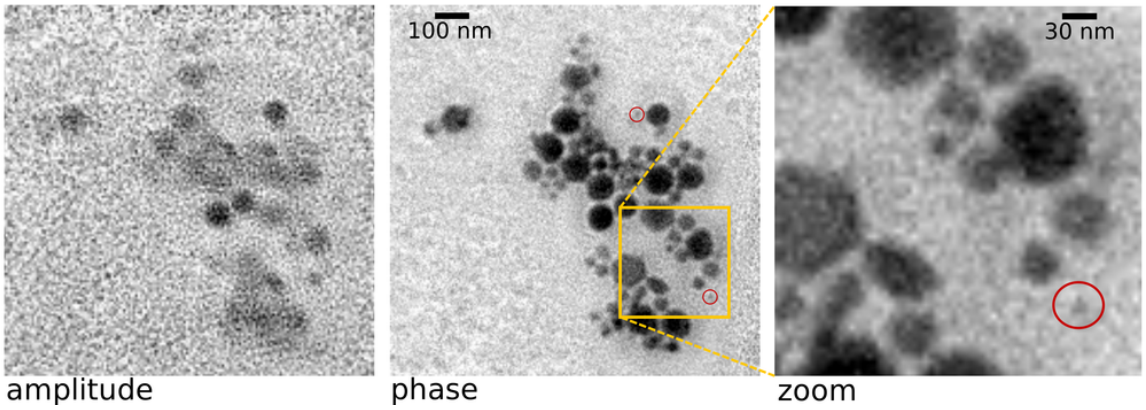

Figure 4.2.7: Final reconstruction of the model sample after the position correction. The amplitude is reconstructed so well, that the stronger absorption of platinum is clearly visible. In the phase shift reconstruction smallest particles down to 15 nm (red circle) become visible.

one is 50 nm in real space. This correlates to a step size of about 7 px related to the pixel size of 7 nm in the reconstruction. During the reconstruction, the correction algorithm had the freedom to search for the correct position of each diffraction pattern in a range of ± 5 px around the originally given position, checking every second pixel in that range. Fig. 4.2.8 illustrates the average distribution of the positions of the diffraction patterns in the scan. In Fig. 4.2.8a, the center of the image depicts the original position of a diffraction pattern.

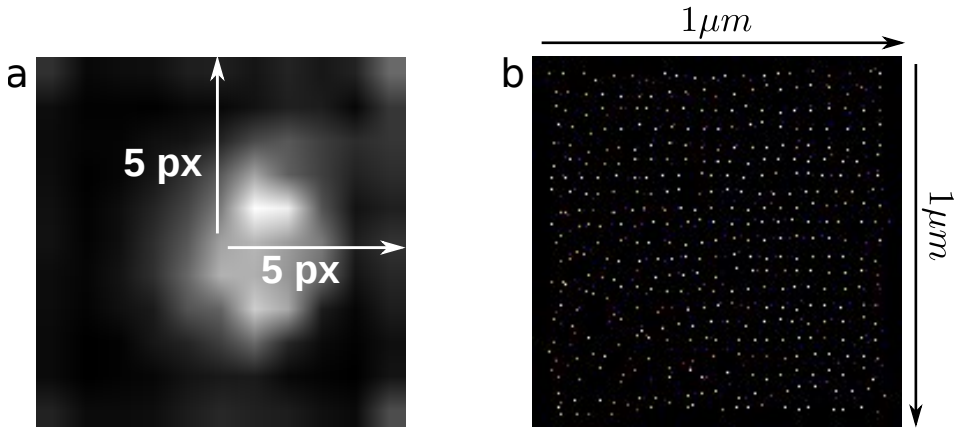

Figure 4.2.8: Information about the ensemble in the position correction algorithm. a) illustrates average position of all ensembles in the entire scan. b) shows the position of the center of mass of the ensemble of probe functions per scan point for the entire scan.

The brighter a pixel, the more often the diffraction patterns were located in the area of this pixel. The bright round distribution around the original position confirms an isotropic random positioning error. On average, the position error was in the range of about ± 3 px $\approx \pm 21$ nm. The little brighter areas in the outer region imply comparatively few larger positioning errors for individual scan points. In Fig. 4.2.8b, the positions of the center of mass are given for the probe ensemble of each scan point in both scans. The entire scan range of 1 µm $\times$ 1 µm is shown and each point stands for a center of mass of an ensemble per scan point in both scans. Additionally, the brightness of each point correlates to the number of ensemble

members at this scan point. In the lower left of the diagram in Figure 4.2.8b, the ensemble positions are more or less random, since there is no sample scattering in this flat-field area. Consequently, the algorithm had no useful information to correlate the positions with the diffraction patterns.

4.2.4 Spatial Resolution and Phase Sensitivity

In order to quantify and compare the image quality of the different reconstructions several parameters such as the standard deviation in the background of the reconstruction, the reconstructed probe intensity and the spatial resolution are used, cf. Table 4.2.2. The

Table 4.2.2: Different parameters for the comparison of the image quality

Parameter	std background	probe intensity	spatial resolution
no constraint	7 mrad	5.07×10^6 Ph/s	35 nm
obj. constraint	9 mrad	2.385×10^7 Ph/s	31 nm
obj. + probe constraint	9 mrad	2.392×10^7 Ph/s	31 nm
probe constraint	7 mrad	2.392×10^7 Ph/s	31 nm
combined data set, probe constraint	3 mrad	2.392×10^7 Ph/s	19 nm
position correction	5 mrad	2.392×10^7 Ph/s	13 nm

standard deviation in the background (SiN membrane) for the reconstruction without beamstop is about 6.7 to 8.6 mrad depending on the reconstruction constraints. This value can be assumed as a rough marker for the phase sensitivity, which plays an important role for the analysis of the scans as function of energy to determine the chemical distribution. Similar to the *Siemens* star reconstructions, the intensity of the reconstructed probe is slightly too low but almost correct, when using only the object constraint. The phase shift values of the spheres match very well with the expected values for gold and platinum. For example, a 100 nm gold sphere in the reconstruction has a phase shift of 107 mrad and the expected value for a 100 nm gold layer at 12 keV is 111 mrad.

As described in Section 2.4, the spatial resolution of an image can be determined in several ways. In the coherent imaging community, the FOURIER ring correlation (FRC) is common. Due to the absence of sharp lines and features in the model sample, edge detection is not suitable to estimate the spatial resolution. Thus, FRC was used here to compare the image quality in terms of spatial resolution for the different ways of ptychographic reconstruction. In order to avoid false correlation effects leading to an overestimated resolution a KAISER-BESSEL window of the size 1.5 was applied to the aligned images in advance. Based on the statements by van Heel and Schatz [2005], the half-bit resolution criterion was used. The spatial resolution of the reconstructions of the data sets without beamstop is about 30 nm independent of the constraints that were set during the reconstruction process. Without any constraints during the reconstruction, a spatial resolution of 35 nm illustrates similar image quality. For the combined reconstruction, an increase in resolution to about 19 nm is validated by the FRC. The best resolution of about 13 nm is achieved after the conduction of the position correction algorithm for the combined reconstruction. The FRC

plots are shown for the reconstruction without beamstop and for different constraints in Fig. 4.2.9a.

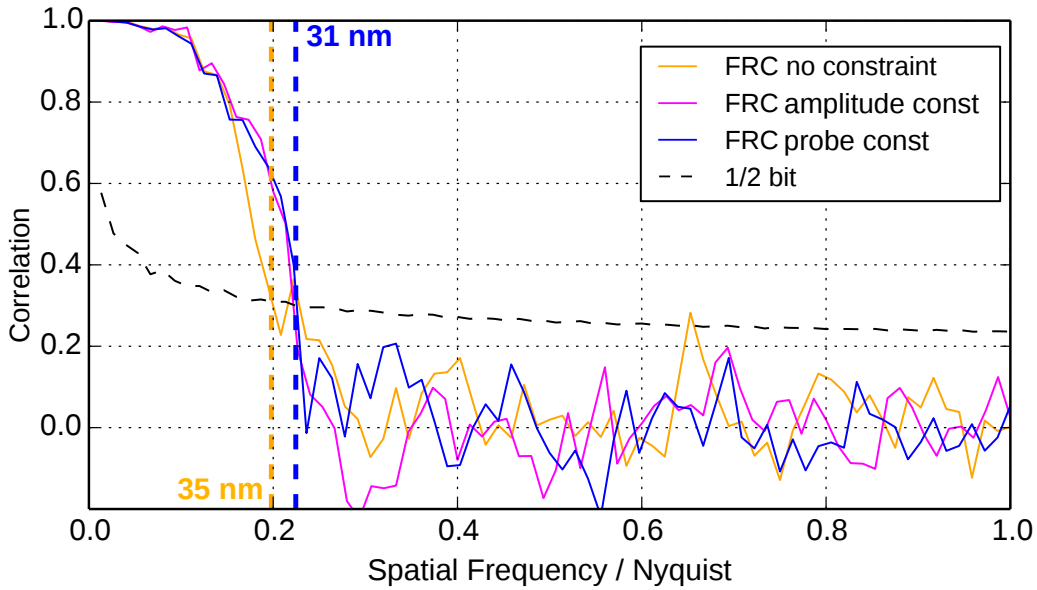

(a) FRC for the different kinds of reconstruction using only the data set without beamstop.

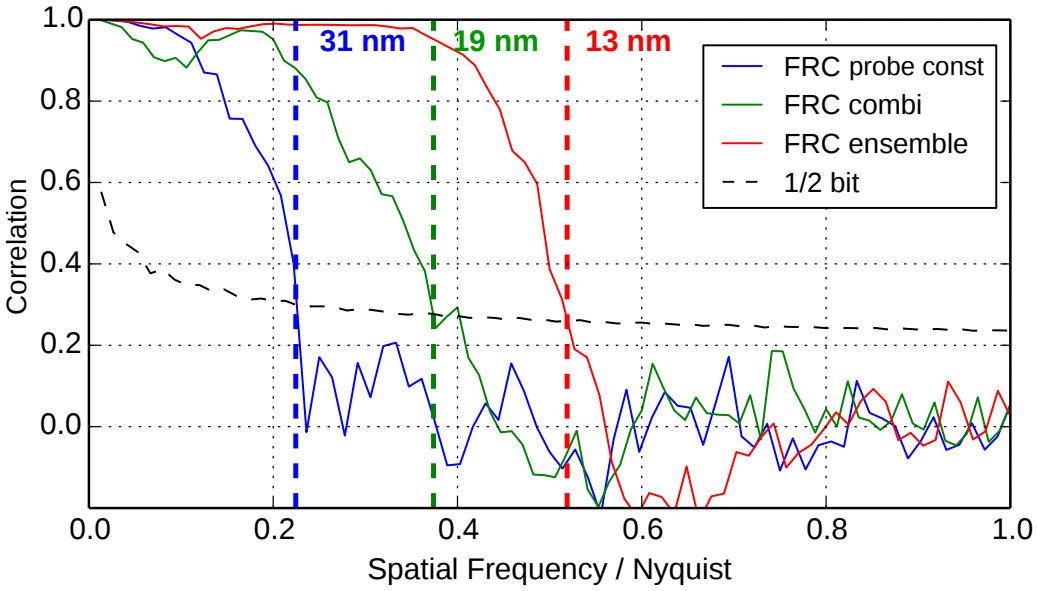

(b) FRC for the different kinds of reconstruction using the data set without beamstop (red), the basic combined reconstruction (cyan) and the final result using the position correction algorithm (magenta).

Figure 4.2.9: Spatial resolution estimated by the Fourier-Ring Correlation (FRC)

The FRC plots for the combined reconstruction with and without position correction are compared to the reconstruction without beamstop and probe constraint in Fig. 4.2.9b. The spatial resolution slightly varies for different pixel cropping of the diffraction patterns, not shown here. This is due to the higher noise level in high scattering angles. In Section 4.2.6, the signal-to-background ratio will be discussed as function of scattering angle.

4.2.5 Chemical Distribution

Resonant ptychography was applied to determine the chemical distribution of the sample, in this case, to distinguish between the different elements gold, platinum and palladium. Therefore, the ptychographic scans were repeated at 43 different energies around the Au-L_3 and the Pt-L_3 absorption edges. The energy intervals around these absorption edges are depicted by the gray area between the vertical dashed lines in Fig. 4.2.10.

One way to determine and visualise the chemical distribution is a difference map of the 2D reconstructions as shown in Fig. 4.2.10. For this purpose, first, the phase shift reconstructions at different energies were aligned to each other. Afterwards, the difference map is gained by subtracting one reconstruction from another. Here, this was done for three different cases: First, reconstructions at two energies around the Pt-L_3 egde, $11\,550\,\mathrm{eV}$ (pre-edge) and $11\,564\,\mathrm{eV}$ (at the edge) were subtracted. This is shown in Fig. 4.2.10d. Analogously, Figure 4.2.10f shows the difference at the Au-L_3 edge between $11\,930\,\mathrm{eV}$ (post-edge) and $11\,918\,\mathrm{eV}$ (at the edge). In both difference maps, the resonance effect cannot be identified by the difference within the small energy ranges at the Au-L_3 and the Pt-L_3 edge separately. Instead only artefacts due to persistent misalignment and noise are visible. Calculations for the phase shift of a $100\,\mathrm{nm}$ layer of gold respectively platinum confirm that the expected change in the phase shift within the small energy ranges, cf. Figure 4.2.10b and c, around each edge separately is minimal; for platinum approximately $10\,\mathrm{mrad}$ and for gold approximately $5\,\mathrm{mrad}$. Thus, the phase shift sensitivity achieved in the reconstructions of approximately $\pm 5\,\mathrm{mrad}$ is not sufficient to resolve the resonance effect. Instead, it was necessary to consider the entire energy range between the Au-L_3 and the Pt-L_3 edges to achieve sufficient chemical contrast. For the entire energy range, the expected difference in phase shift between the two edges of gold and platinum is approximately $20\,\mathrm{mrad}$.

According to this, the third map shows the difference between a reconstruction at the platinum edge and a reconstruction at the gold edge. In Figure 4.2.10e, the chemical contrast is clearly visible, as the dark spheres display the gold particles with $\Delta\phi$ up to $-20\,\mathrm{mrad}$ and the bright spheres display the platinum particles with a positive phase difference of $\Delta\phi = 10\,\mathrm{mrad}$. Due to a shift in the energy calibration at the Pt-L_3 edge, the phase shift minimum was probably not perfectly hit and consequently the phase shift difference for platinum turns out smaller than expected in comparison to the gold phase.

4.2.6 Diffraction Data Analysis

The analysis of the scattering power as well as the noise and background level in the diffraction patterns with and without beamstop reveal valuable information on the data quality in particular concerning the influence of the beamstop. In addition, the signal-to-background ratio (SBR), cf. Section 2.5.2 provides an estimation of the expected spatial resolution. The evaluation presented in this section is published in Reinhardt et al. [2017].

In order to unravel the scattering signal of the sample over background scattering, diffraction patterns without sample scattering (so called flat fields) are required. During the experiment, only the ptychographic scans were recorded and no further data without sample,

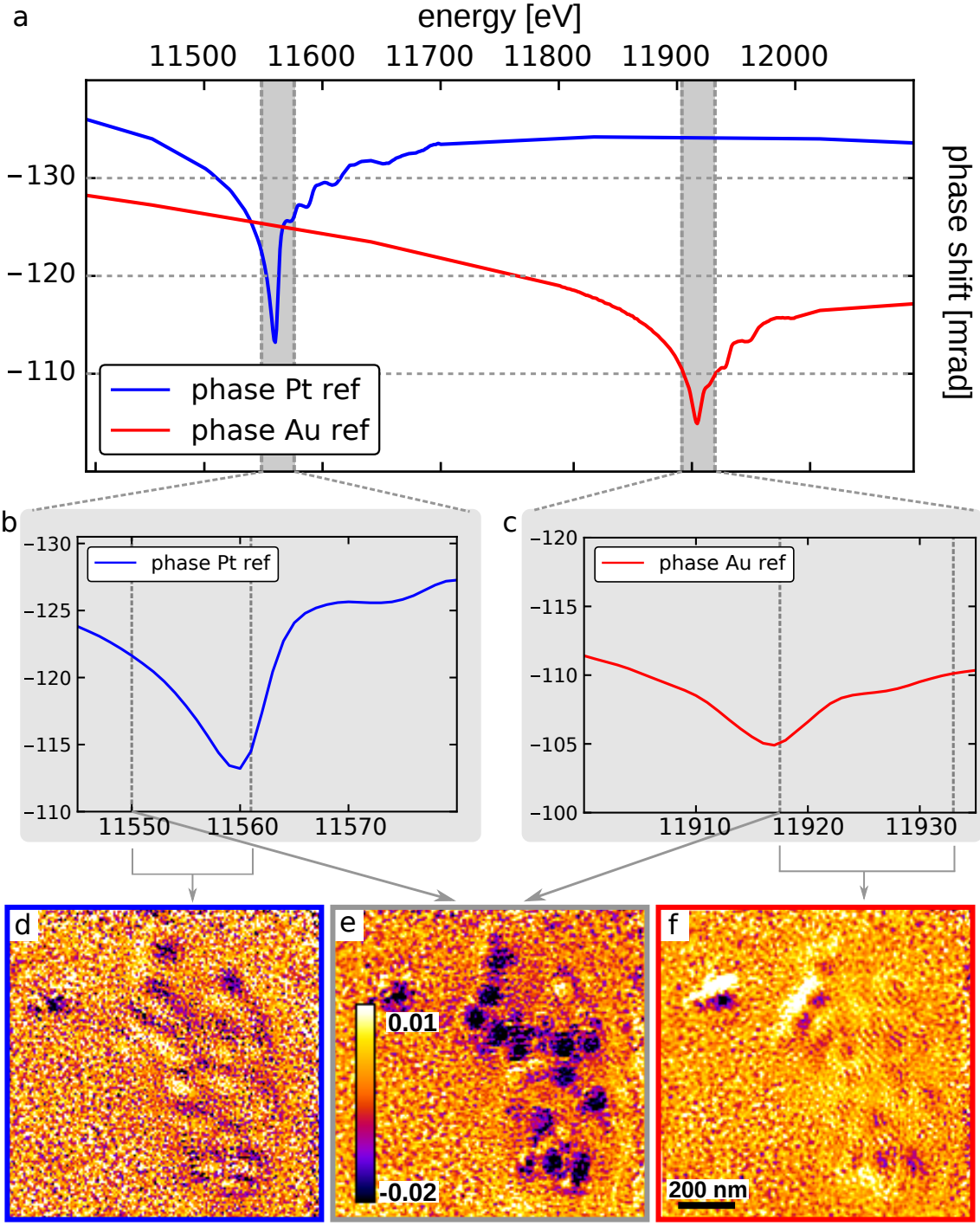

Figure 4.2.10: Chemical analysis of the model sample. a) shows the expected phase shift for platinum and gold of 100 nm thickness around the L_3 absorption edges and the energy intervalls where ptychographic data sets were recorded. b) and c) show the phase shift curve in the small energy intervall for each absorption edge separately. The resonance effect is only 10 mrad for platinum respectively 5 mrad for gold. d) shows the difference between the phase reconstructions at 11 550 eV and 11 564 eV (dashed lines in b) at the Pt-L_3 edge, analogously f) shows the difference between 11 917.5 eV and 11 933 eV at the Au-L_3 edge. In both images, the resonance effect is below the detection limit. e) shows the difference between the energies 11 550 eV and 11 917.5 eV and the resonance effect is clearly visible for gold with $\Delta\phi$ down to -20 mrad (dark spheres) and platinum with $\Delta\phi$ down to 10 mrad (bright spheres).

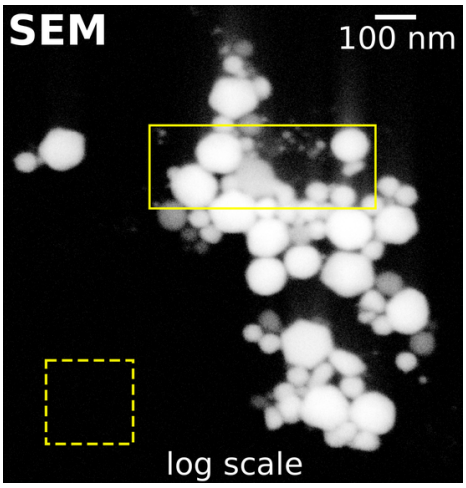

Figure 4.2.11: Regions of interest (ROI). Two different areas of the scan, containing either the sample material (rectangle = ROI *sample*) or only the empty Si_3N_4 membrane (dashed square = ROI *background*), were chosen.

that could serve as flatfields. As a consequence, the flatfields had to be extracted from areas in the ptychography scan, which do not contain any nanoparticles. Different regions of interest (ROI) were chosen within the scan area. A flat area not holding any particles of the sample (ROI *background*) is marked by a dashed yellow square in Fig. 4.2.11. On the one hand, the diffraction patterns of ROI *background* served to determine and normalise the intensity of the incoming illumination during the reconstruction, cf. Section 4.2.3. On the other hand, here, these diffraction patterns were used to determine the background and to subsequently calculate the signal-to-background ratio (SBR). In addition, another region (ROI *sample*) with a representative distribution of nanoparticles was chosen to obtain the average sample signal for a ptychography data set. This area is marked by the yellow rectangle in Fig. 4.2.11. First, the diffraction patterns of scan A taken from the ROI *sample* were averaged and the two-dimensional intensity distribution shows scattered intensity up to 0.016 Å^{-1} around the central order referring to sample features about 20 nm in size, cf. Fig. 4.2.12a. In order to achieve equal photon statistics for diffraction patterns of an exposure time of 3 s, ten single diffraction patterns of scan A (ROI *sample*) were summed up. In this case, photon scattering is detected for higher scattering angles, shown in Fig. 4.2.12b. Naively, this should result in high spatial resolution of at least 5 nm in the ptychographic reconstruction. However, further analysis pointed out that most of the scattered intensity does not come from the sample. In contrast, in the diffraction pattern with beamstop the background is considerably reduced and the signal of the sample appears clearly as a typical scattering pattern of several spheres, shown on the right in Fig. 4.2.12c. Scattering features are detected beyond 0.035 Å^{-1}, which is related to sample features of about 10 nm in size. Afterwards, the average intensity of the diffraction patterns was azimuthally integrated and the amount of photons scattered by the sample versus background scattering is visualised as a function of the length q of the scattering vector. In Fig. 4.2.13, the signal and background are compared for diffraction patterns without beamstop and exposure times of 0.3 s and 3 s, respectively. Matching colors stand for the same scan, light colors represent the background and dark colors represent the

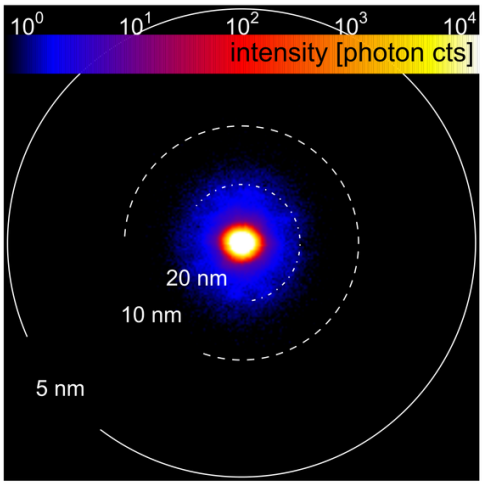

(a) Without beamstop 0.3 s exposure time.

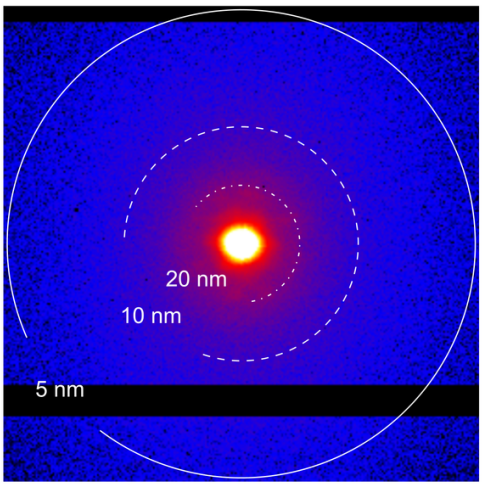

(b) Without beamstop 3 s exposure time.

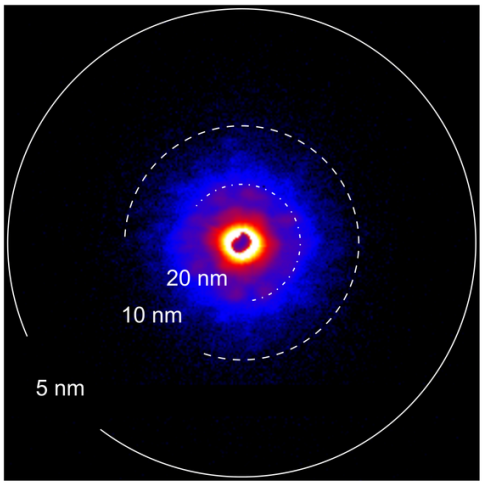

(c) With beamstop 3 s exposure time.

Figure 4.2.12: Comparison of the scattering signal in the 2D diffraction patterns with and without beamstop. a) shows the average of a conventional diffraction pattern with a short exposure time of 0.3 s. In comparison, in b) the exposure time is increased to 3 s. Not only the sample signal increases but also parasitic, incoherent background scattering. Only c) shows a flat background in high scattering angles and an increased sample signal up to 10 nm feature size.

signal of the sample. The conventional scan A – depicted in green with 0.3 s exposure

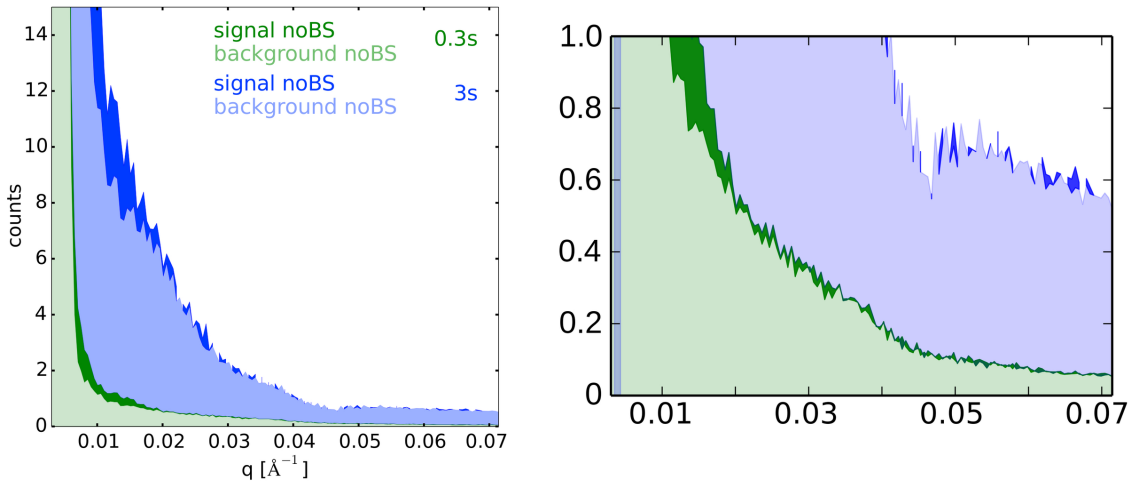

Figure 4.2.13: Comparison of the signal and background for different exposure times of 0.3 s and 3 s for the diffraction patterns without beamstop.

time – shows in general a small signal at higher q values with a small contribution (dark green) of the sample above the background scattering (light green). With an exposure time of 3 s – shown in blue in Fig. 4.2.13 – a large background signal (light blue) and a relatively low (dark blue) signal from the sample is present. At high q, the sample signal is completely covered by background radiation. The ptychographic algorithm assumes this background to be meaningful diffraction data from the sample, leading already to artifacts within the reconstruction for exposure times of 0.3 s, shown in Fig. 4.2.2. Thus, regarding the background noise, only increasing the number of photons by longer/multiple exposure times is not particularly suitable to gain higher spatial resolution from higher signal when the beam path is not cleared by ,e.g., a flight tube. By expanding the ptychographic model including an incoherent background similar to Hoppe et al. [2013], the artefacts can be reduced, but the spatial resolution and sensitivity are inherently limited by the signal-to-background ratio. Therefore, the opaque beamstop was implemented into the setup to improve the reconstruction. In Fig. 4.2.14, the signal and the background are compared

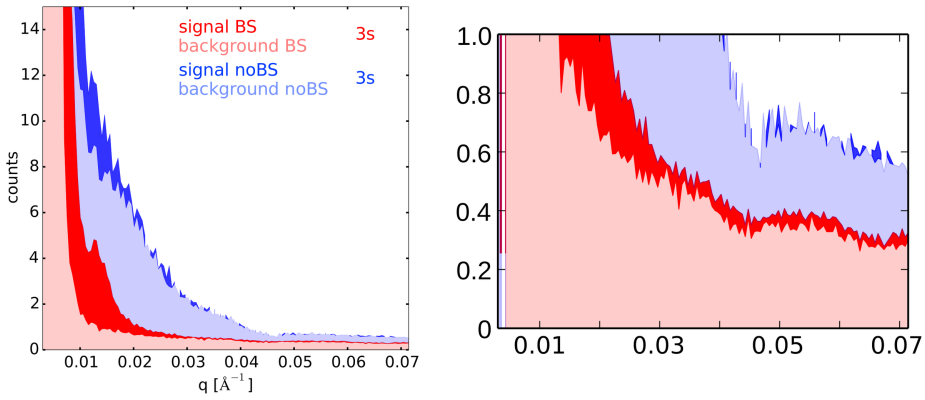

Figure 4.2.14: Comparison of the signal and background for an exposure time of 3 s for the diffraction patterns without and with beamstop.

for the scans with (scan B) and without beamstop (scan A) both for an exposure time of 3 s. With the beamstop, scan B has generally lower count rates at higher q (shown in red). Notably, the main difference lies in the reduced background signal (light red) compared to that of scan A (light blue). The signal from the sample (dark colors) is very similar for both scans. However, the sample signal (dark red) is clearly visible up to high q values on top of the low background signal (light red) for scan B, which was recorded with the beamstop. In contrast, the sample signal (dark blue) of the conventional scan A without beamstop vanishes in the high background (light blue) for high q.

Fig. 4.2.15 shows the signal-to-background ratio for both scans – with and without beamstop. In the zoomed plot in Fig 4.2.15, the improvement in data quality when using a beamstop is distinctly visible, since the level of zero is reached at around $q = 0.04\,\text{Å}^{-1} \mathrel{\widehat{=}} 8\,\text{nm}$ instead of approximately $q = 0.02\,\text{Å}^{-1} \mathrel{\widehat{=}} 16\,\text{nm}$. This is in good agreement with the improvement of the sensitivity and the spatial resolution of about 10 nm in the combined reconstruction, where individual nanoparticles of about 15 nm become visible, marked by red circles in Fig. 4.2.7.

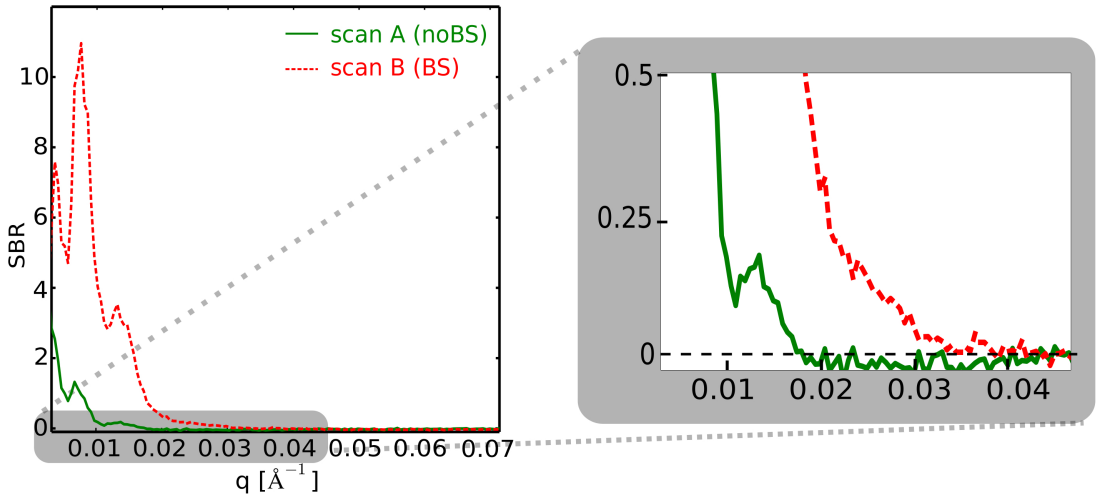

Figure 4.2.15: Signal-to-Background ratio with and without beamstop. For the data set with beamstop (dashed red), the SBR is increased by a factor of 2.

The average intensity distribution as well as the signal-to-background ratio (SBR), which is defined in Section 2.5.2, depict the influence of the beamstop on the sample signal that is still detectable in higher scattering angles. The analysis of the diffraction patterns shows that only with the use of a beamstop does the sample signal emerge significantly from the background for the increased exposure time of 3 s. Solely increasing the statistics at high scattering angles, i.e., increasing the photon flux and the dynamic range, cannot sufficiently increase the image quality. Using a semi-transparent beamstop could only achieve a minor reduction and since a major part of the background scattering arises in the detector material itself, better detectors with less intrinsic detector scattering may provide higher data quality in the future without a beamstop. For now, the reduction of background scattering by the opaque beamstop is substantial, especially since using a flight tube cannot suppress background scattering by the detector material itself.

4.2.7 Conclusion

The approach of implementing an opaque beamstop into the setup to suppress background scattering was successful. Furthermore, the simultaneous reconstruction of two data sets – one with and one without beamstop – resulted in quantitative reconstructions of the weakly scattering catalyst model sample with high spatial resolution better than $15\,\mathrm{nm}$ and high sensitivity to the weak features. Finally, the position correction algorithm allowed for the precise alignment which was required to achieve the chemical contrast between the two metals gold and platinum.

4.3 Platinum on Yttria-Stabilised Zirconia

Chemical gas sensors or solid oxide fuel cells (SOFC) play an important role for different purposes, e.g., for oxygen sensing during the combustion in automotive engines for pollution control or for the production of electricity from oxidizing a fuel. For these purposes, one of the most prominent solid state electrode systems is the platinum on yttria-stabilised zirconia ($Pt(O_2)$/YSZ) system[76,62]. To understand the processes during the chemical reaction, the $Pt(O_2)$/YSZ system has been extensively studied[104,103]. However, many open questions remain such as the formation and role of platinum oxide at the interface of the metal layer and the crystal.

4.3.1 Pt Bubble Formation

During electrochemical treatment, the platinum layer forms bubbles, which may contain different oxidation states of platinum. After the successful application of resonant ptychography for chemical imaging of the catalyst model sample, cf. Section 4.2.5, a platinum layer on yttria-stabilised zirconia was investigated in another ptychography experiment. Now, the analysis of a resonant data set aims for the determination of the oxidation states in the layer. This information on the chemical distribution is scientifically relevant since the bubble formation should be avoided to achieve durable devices such as an oxygen sensor. In Fig. 4.3.1, an SEM image of such a platinum bubble is shown after it was cut by FIB. Based on the SEM image, it is assumed that an oxide layer is present where the gray contrast is darker, marked by the yellow arrow. The actual Pt bubble studied by (resonant) ptychography was closed, cf. Fig. 4.3.2 during the X-rays studies and only cut open afterwards.

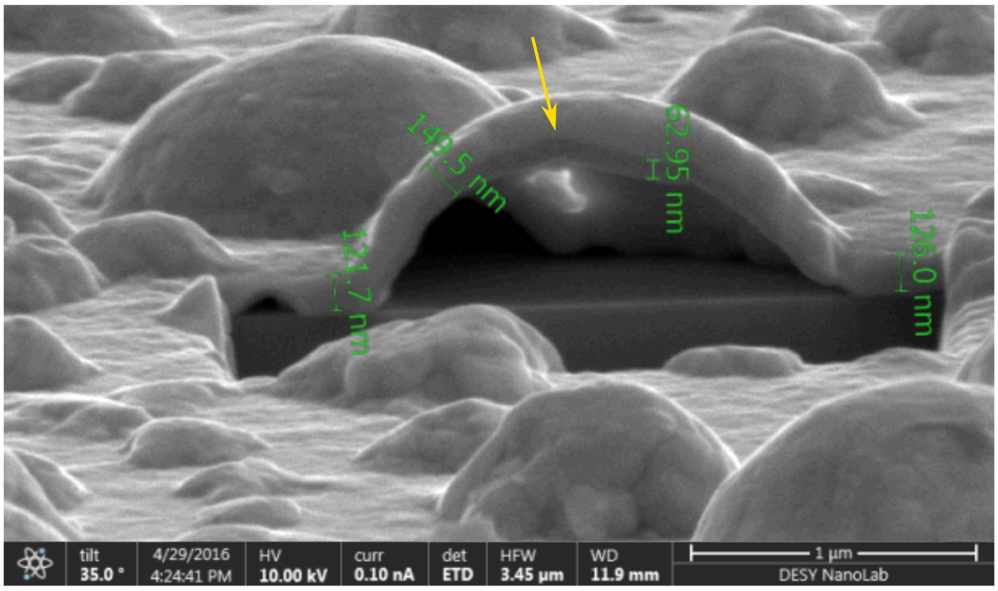

Figure 4.3.1: SEM image of a Pt bubble. The Pt bubble was cut open and shows layers of different contrast. The darker layer, marked by the arrow, is assumed to be an oxide layer. Courtesy: DESY NanoLab

4.3.2 Sample Preparation

At the DESY NanoLab, FIB techniques were used to prepare a specimen suitable for resonant and tomographic ptychography. A small piece of several square micrometers was cut from the entire platinum layer and the underlying the zirconia crystal. With the help of mirco-manipulators, this piece was deposited and fixed on the tip of a pin that serves as sample holder during the X-ray measurements. In Figure 4.3.2, the final sample preparation is shown together with the direction of the X-ray beam during the resonant ptychography experiment for better orientation to what will be seen later in the ptychographic reconstruction.

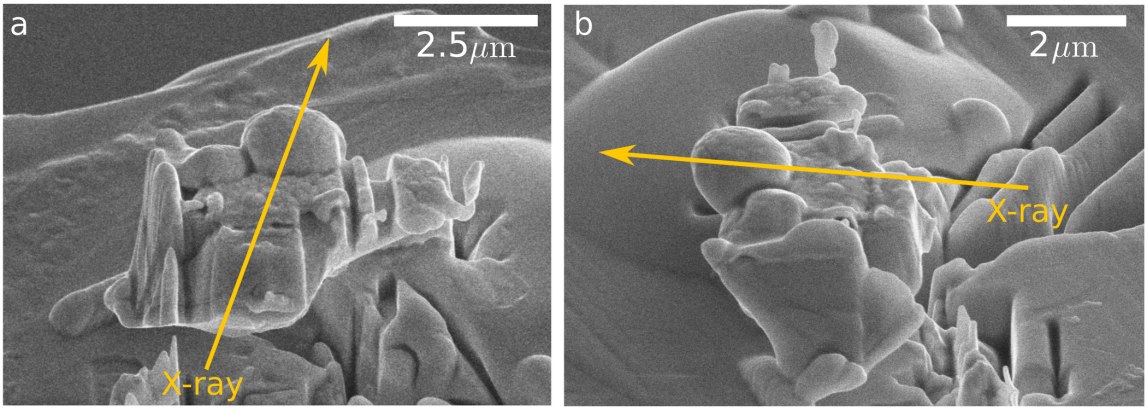

Figure 4.3.2: SEM image of the Pt bubble prepared by FIB. The yellow arrows mark the orientation of the sample relatively to the X-ray beam during resonant ptychography experiment. Courtesy: DESY NanoLab

4.3.3 Experimental Parameters

In the beginning of the experiment, the transmission of a platinum foil was recorded as function of energy around the Pt-L_3 absorption edge, to calibrate the monochromator to the actual photon energy. From this measurement, the value of 11 560 eV given by the monochromator matches the Pt-L_3 edge which is at 11 563.7 eV. Thus, the actual values of the measurement at the different energies require a shift by +3.7 eV. In Fig. 4.3.3, the imaginary part f_2 of the atomic form factor and the phase shift of metallic and oxidised platinum are shown as function of energy around the Pt-L_3 edge. The phase shift was calculated from f_2 via the KRAMERS-KRONIG relation for a Pt respectively PtO_2 layer of 1 µm thickness.

For the measurements of the Pt bubble, the chromium layer of the higher order reflecting mirror in the optics hutch of beamline P06 was used to suppress the higher harmonics of the photon energy. This leads to a cleaner beam concerning parasitic scattering and reduced chromatic aberration of the focus, which was produced by the refractive nano focusing lenses.

According to the standard experimental procedure described in Section 3.5, the ptychographic experiment was conducted after the optics alignment. An evacuated flight tube was placed into the ≈2 m long beam path to reduce the air scattering background in the

diffraction patterns. In Table 4.3.1, the basic scan parameters are listed. For the acquisition of the diffraction patterns of this experiment, the single-photon counting pixel detector – the EIGER 4M was used. The ptychographic scan was repeated at 46 different energies around the Pt-L_3 edge in the energy range between 11 480 eV and 11 680 eV marked by the dashed vertical lines in Fig 4.3.3. One ptychographic scan took approximately 25 min.

Table 4.3.1: Basic scan parameters: Ptychography of the Pt bubble

Parameter	
Dwell time per scan point	0.5 s
Scan area (h x v)	4 µm × 2.8 µm
Number of steps (h x v)	50 × 35
Step size	80 nm
Photon flux in focus	4×10^7 Ph/s
Pixel size of detector	75 µm

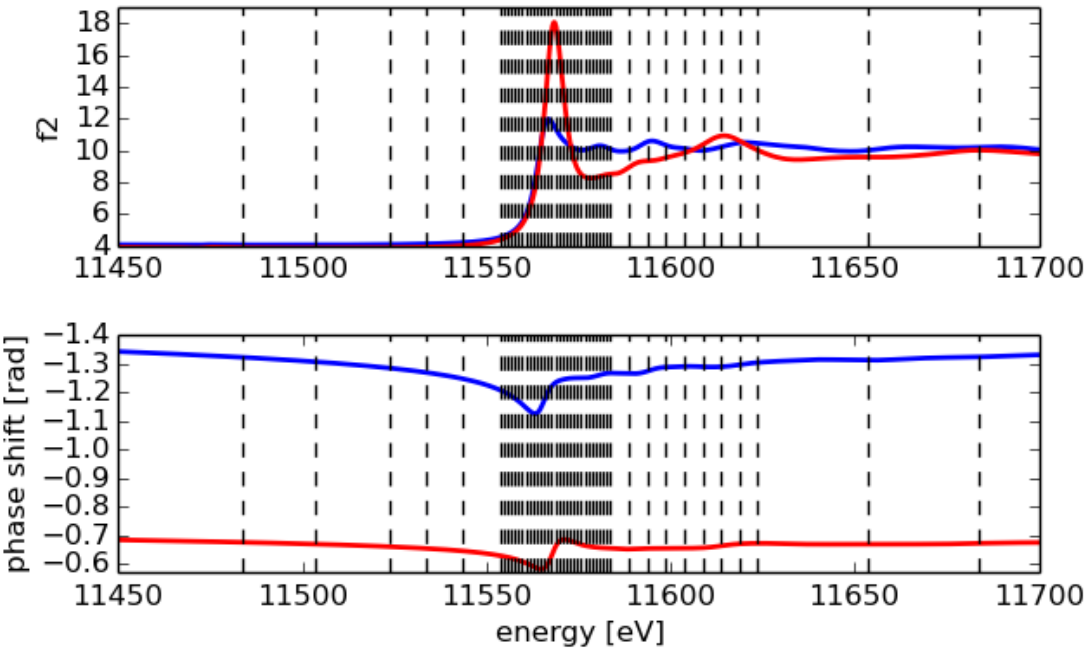

Figure 4.3.3: Phase Shift References for Platinum. Expected phase shift of Pt (blue) and PtO_2 (red) at the Pt-L_3 edge and the energies (vertical dashed lines) where ptychograms were recorded.

4.3.4 Ptychographic Reconstruction

The ptychographic reconstruction was performed using the ePIE algorithm[65]. Because of the enlarged size of one data set, a GPU-accelerated implementation in C++ was

used instead of the python implementation. This software package was developed by Hönig [2010] and Hoppe [2017].

A Gaussian-shaped probe function with a FWHM of 200 nm and a flat object function were used as the initial guess. The diffraction patterns were cropped to 512 px × 512 px resulting in a pixel size of approximately 6 nm in the ptychographic reconstruction, slightly varying with the photon energy. The error function converged after 50 iterations and the reconstructed probe intensity is about 1×10^8 Ph/s, the results are expemplarily shown for one scan at a photon energy of E = 11 600 eV in Fig. 4.3.5.

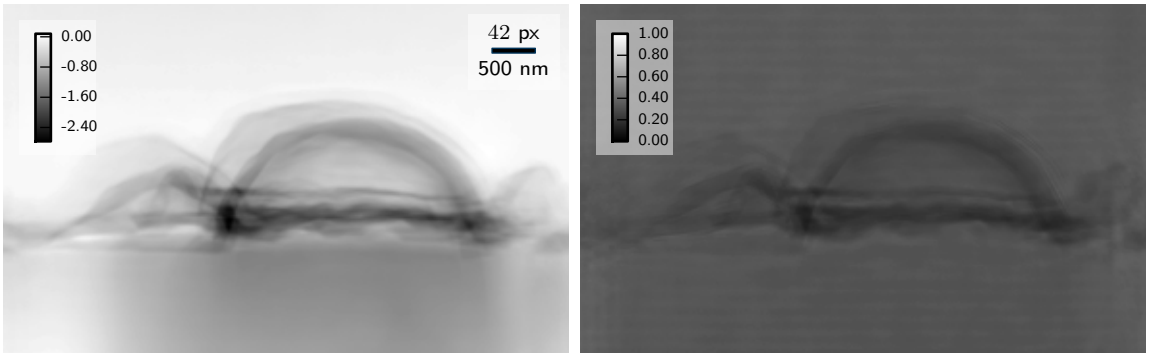

(a) Reconstructed phase and transmission of the Pt bubble.

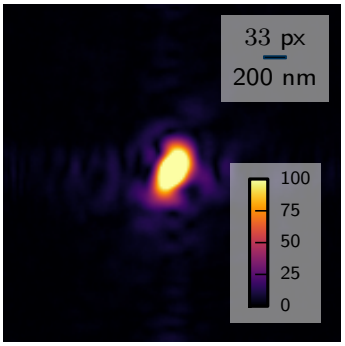

(b) Amplitude of the reconstructed probe function

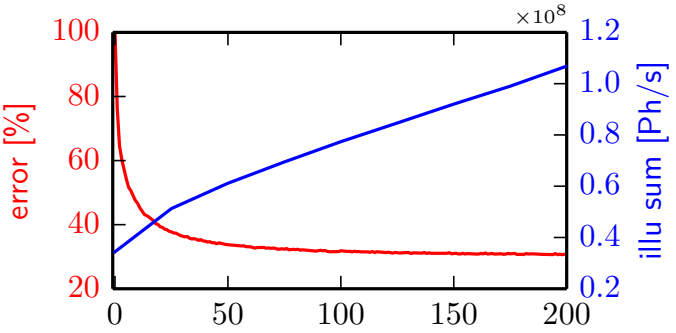

(c) Error function and probe intensity

Figure 4.3.4: Ptychographic reconstruction of the Pt bubble without constraints.

As seen in the reconstructions of the catalyst model sample in Sec. 4.2.3, the ptychographic algorithm is unable to find the real probe intensity, instead it is increasing Therefore, the probe constraint is set to normalise the total probe intensity to the photon flux of 4×10^7 Ph/s

resulting in the reconstruction shown in Fig. 4.3.5a. Again, the object phase reconstruction remains unaffected by a change in probe intensity but the object transmission varies significantly.

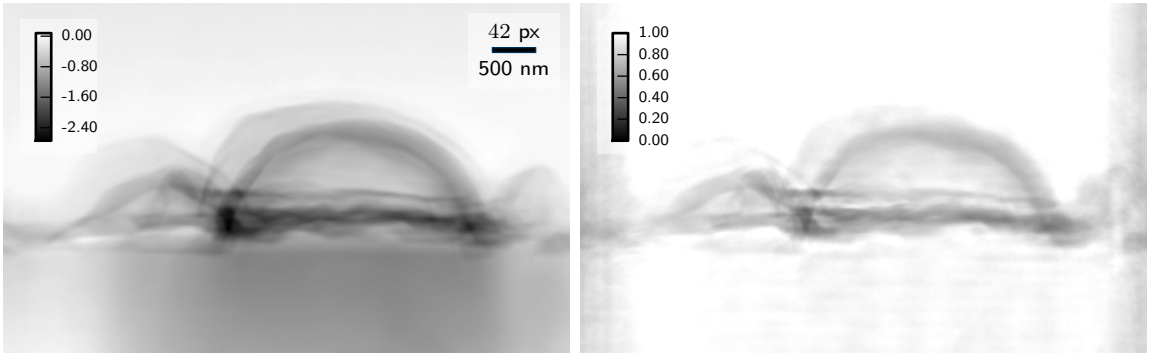

(a) Reconstructed phase and transmission of the Pt bubble.

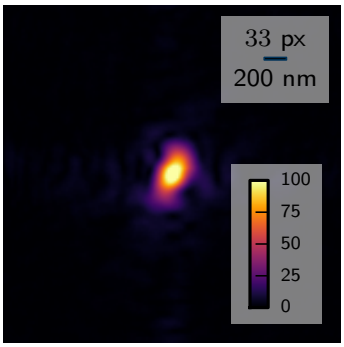

(b) Amplitude of the reconstructed probe function

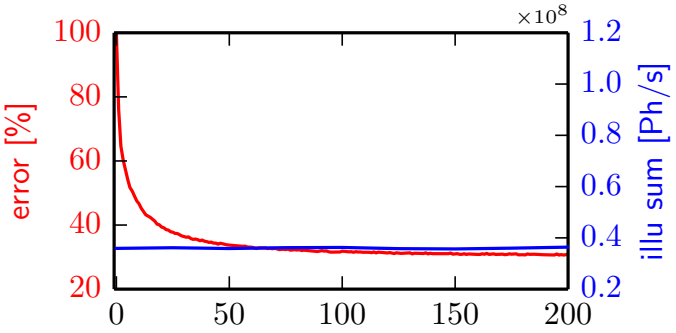

(c) Error function and probe intensity

Figure 4.3.5: Ptychographic reconstruction of the Pt bubble with probe constraint.

In comparison to the catalyst model sample, the Pt bubble is a strongly scattering sample. The sample features a large dynamic range concerning the scattering strength and phase shift of the features. In the lower area, the platinum layer is very thick leading to phase wrapping at off-resonance energies. On top of the bubble, the layer thickness is decreasing resulting in a much weaker phase contrast.

Tomographic Data Set

A detailed tomographic analysis was not part of this work. Here, the preliminary result of the tomographic reconstruction from 59 ptychographic projections is only briefly presented. The 3D view of the Pt bubble supports the understanding of what is actually seen in that particular projection measured at several energies to achieve the resonant data set. So far, it has not been possible to collect a tomographic resonant data set, simply due to beamtime restrictions. In future experiments, the duration of one ptychographic scan (one projection) should significantly be decreased to be able to record several tomograms at different energies. In Fig. 4.3.6, a cut through the 3D reconstruction of the Pt bubble is shown. Figure 4.3.7a shows a top view of the 3D reconstruction along with two projections in b) and c) that correspond to the planes marked in green and blue.

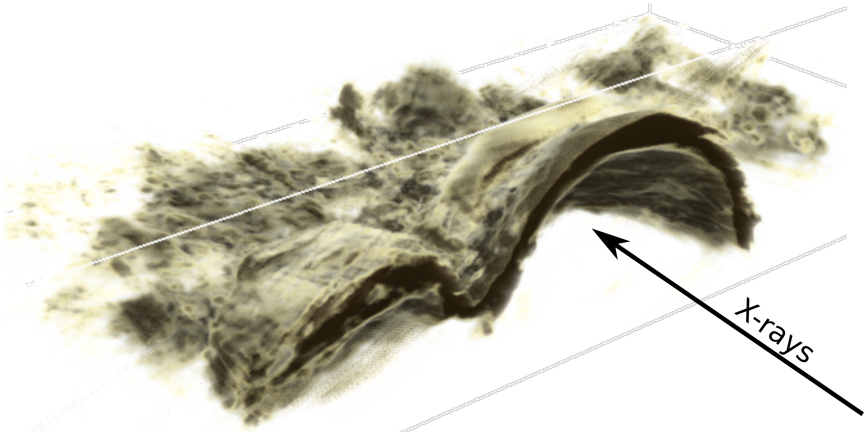

Figure 4.3.6: 3D reconstruction of the Pt bubble. Perpendicular to the X-ray beam, a cut into the 3D reconstruction offers a comparison to the 2D reconstruction.

Resonant Data Set

All 46 ptychographic data sets were reconstructed with the same parameters except from the energy and slight variations in the probe intensity. Since the focal length of the refractive lenses is energy-dependent, the sample position relative to the focal plane varied for the scans at the different energies. Thus, the probe size in the sample plane varies for the scans at different energies, as the sample position along the beam was not changed during the experiment. The entire range where the sample was positioned to the beam focus is illustrated in Fig.4.3.8. The FWHM (h x v) of the probe amplitude distribution ranges from $240\,\mathrm{nm} \times 260\,\mathrm{nm}$ to $290\,\mathrm{nm} \times 450\,\mathrm{nm}$ for sample positions in the focal plane and out of focus. Thanks to the small pixel size of $75\,\mu\mathrm{m}$ of the EIGER detector, a probe size up to $1.5\,\mu\mathrm{m}$ ensures correct sampling in the theoretical limit. Thus, even the enlarged probe size for the sample positions outside of the focal plane were handled without restrictions in the energy range around the Pt-L_3 edge. In fact, the larger probe sizes were advantageous concerning the redundancy in information achieved by sufficient overlap between the adjacent diffraction patterns. With the step size of $80\,\mathrm{nm}$ that was constant for all scans, the overlap between the diffraction patterns ranges from $66\,\%$ to $82\,\%$.

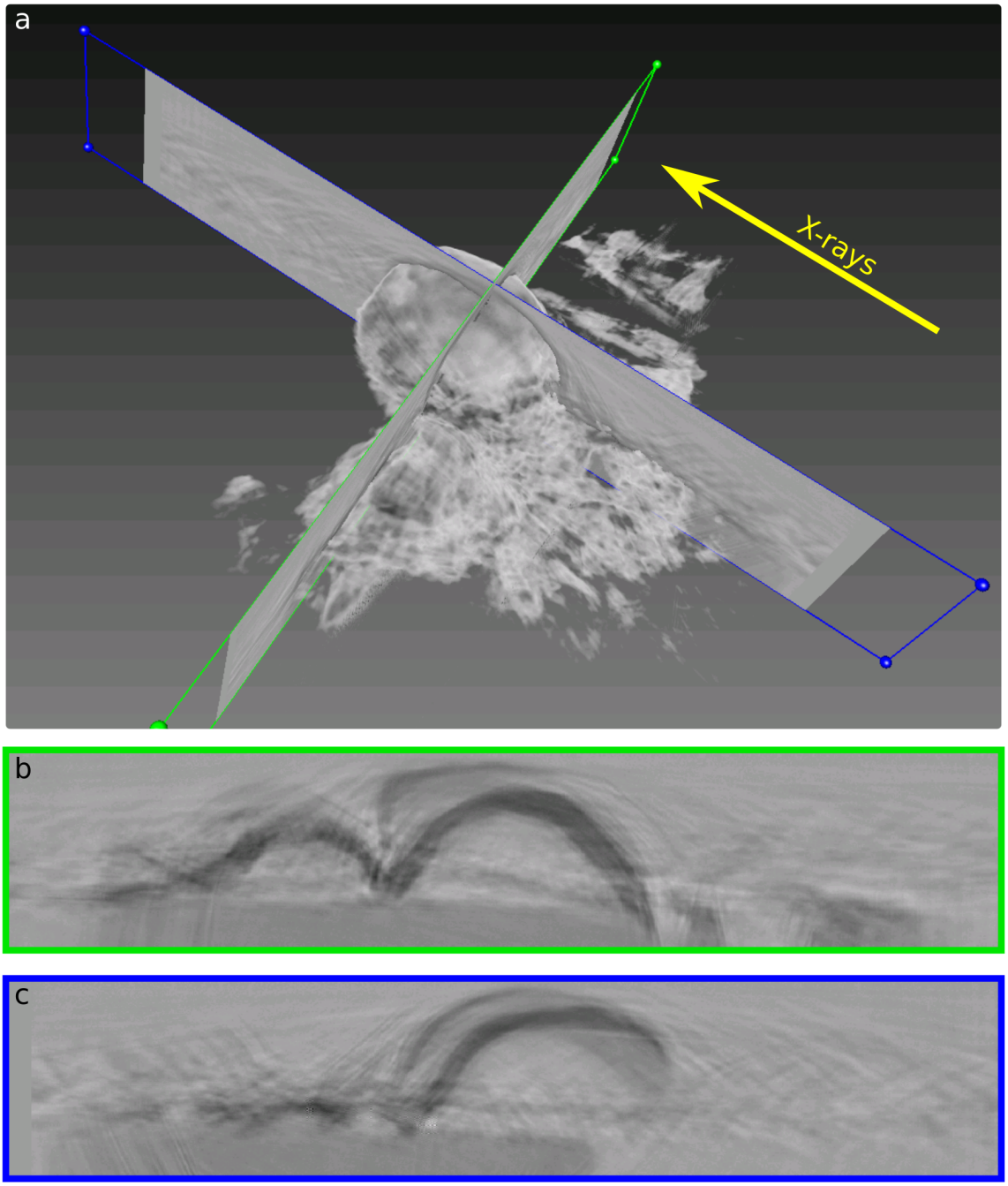

Figure 4.3.7: Different planes in the 3D reconstruction of the Pt bubble. c) shows a top view on the 3D reconstruction of the Pt bubble. b) shows the projection along to the X-ray beam as it is also seen in the 2D ptychographic reconstructions. c) shows the projection perpendicular to the X-ray beam.

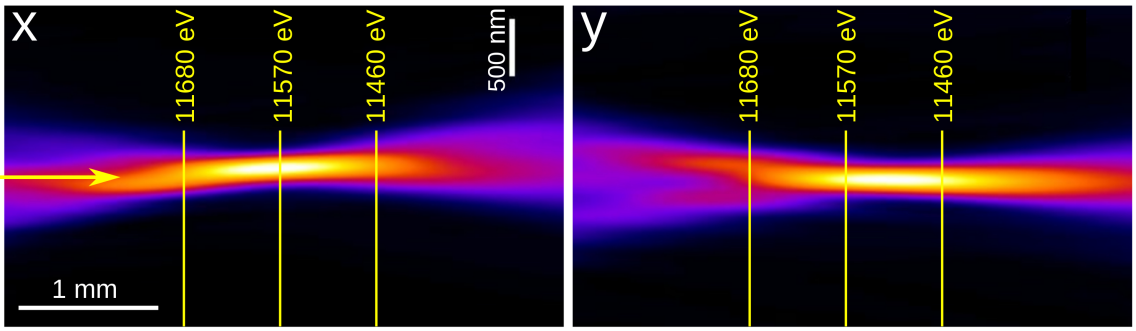

Figure 4.3.8: Propagation of the reconstructed probe in horizontal (x) and vertical (y) direction. The range of sample positions along the beam is marked for different energies by the yellow lines.

All reconstructions are considered successful, since the error function of all reconstruction processes converged in the range of 27 % to 37 % compared to the initial error value. Larger error residuals occurred for the scans at energies close to the Pt-L_3 where the sample scattering in the diffraction patterns is lower due to the resonance effect. Consequently the signal-to-background ratio which means that the background scattering is higher compared to the sample signal leading to a larger residual.

4.3.5 Sensitivity and Spatial Resolution

The quality of the results for the chemical analysis of the entire resonant data set depends on two different aspects: First, the spatial resolution and the sensitivity to small features in each individual scan determines the resolution and sensitivity maximal achievable for the entire data set. Second, the accuracy in the alignment and the background which can vary between the scans diminishes the final results of the chemical analysis. In this section both aspects are discussed.

Quality of a Single Reconstruction

In the Pt bubble reconstructions, linear phase ramps occurred as an artefact, cf. Section 2.1.5. These relatively large phase gradients in the range of 800 mrad along the entire phase reconstruction were removed in the post processing. Afterwards, the standard deviation in flat background areas (air) is approximately 3 mrad with a small remaining phase ramp in the range of 5 mrad to 10 mrad, cf. the plot of the orange line in Fig. 4.3.9b. This is similar for all reconstructions at the different energies.

In addition, phase shift oscillations in the form of vertical stripes appear as plotted in Fig. 4.3.9c related to the blue line in Fig. 4.3.9a. These stripes are probably caused by angular variations of the incident beam. Here, the influence on the object phase shift is minimal of about ± 1 mrad. Thus, even if these stripes occur at varying positions for the different scans, the influence on the entire resonant dataset is negligible.

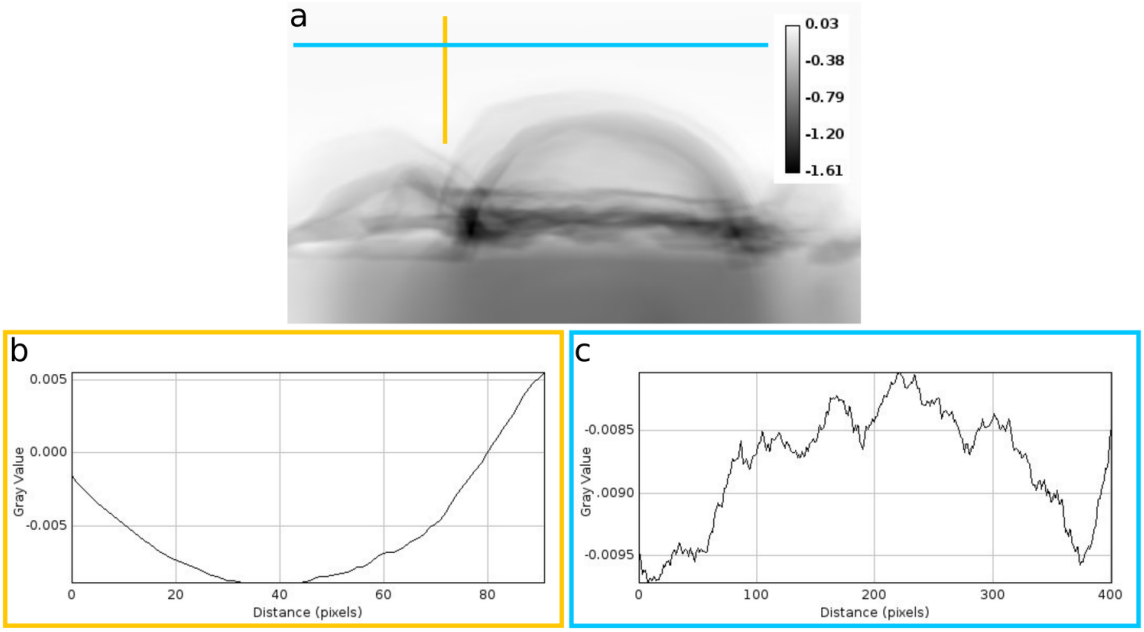

Figure 4.3.9: Phase variations in the background of the Pt bubble reconstruction. a) shows a ptychographic reconstruction of the phase shift of the Pt bubble and the lines corresponding to the plots in b) and c). The plot in b) shows the remaining phase ramp after the phase gradient correction was applied. c) shows the weak oscillations in the background due to variations of the incoming beam.

Spatial Resolution

The spatial resolution was estimated with the help of the FOURIER-Ring-Correlation, cf Section 2.4.2, using two reconstructions of slightly different energies (11 590 eV, 11 595 eV). Here, the FRC shows its weakness by correlating high-frequency artefacts. Therefore, a spatial filter (KAISER-BESSEL window, size = 3.5) was applied to the images to smooth this high-frequency noise. The plot in Fig. 4.3.10 shows large oscillations of the correlation despite the use of the KAISER-BESSEL window. If the second maximum is considered erroneous, the spatial resolution diminishes slightly resulting in a spatial resolution estimation in the range of 7 nm to 10 nm, depending on the zero-crossing. The spatial resolution in the reconstruction is very high and was achieved without the use of an opaque beamstop. One reason for the better resolution compared to the model sample is that the sample scatters much more due to its larger dimension. Therefore, less sensitivity is required and the signal is visible over background even in large scattering angles.

4.3.6 Position Correction and Alignment

As recognised during the analysis of the catalyst model sample, a proper alignment is crucial for the analysis of the chemical distribution. Similar to all previous results, the set of reconstructions of the Pt bubble is subject to inconsistencies due to positioning errors. Although each reconstruction consists only of one data set, positioning errors and drifts lead to distortions of the object shape for the different scans. Thus, the probe

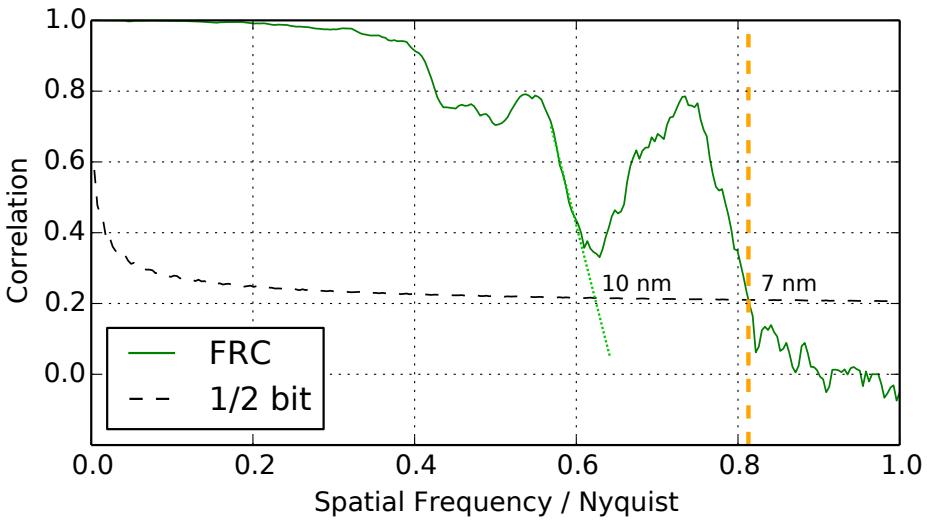

Figure 4.3.10: FRC plot to estimate the spatial resolution of the Pt bubble reconstructions. Despite larger oscillations in the correlation as function of spatial frequency, the limit of spatial resolution is estimated in the range of 10 nm.

ensemble algorithm, cf, Section 2.1.7, was applied, but did not work out as well as it did for the model sample. Because of this, a different approach had to be applied to prepare the reconstructions for the subsequent chemical imaging analysis. The so-called elastic or non-rigid alignment procedures, which are well established in medical imaging, were utilised, cf. Section 2.3. After a coarse alignment using a rigid transformation, the software package SimpleElastix[67] was furthermore used for a subsequent affine and b-spline alignment procedure. At first, the affine registration was applied using the default values for the parameter map. After this kind of registration, some deformations of the sample were still visible for the different scans. In a next step, the testing of different parameter map configurations led to a slightly modified default configuration, which was chosen for the b-spline alignment. For the purpose of reproducibility, the entire set of the parameters can be found in the Appendix A.

The alignment quality was determined by analysing and comparing the standard deviation for the initial rigid registration image stack, for the affine alignment and for the final b-spline alignment. Not only the misalignment for the entire stack of reconstructions, but also the differences for particular reconstructions at different energies were examined to figure out how error-prone the subsequent chemical analysis might be in terms of alignment errors. There is no trivial error measure, since the absolute phase shift in the reconstruction naturally changes for the different energies due the resonance effect. Consequently the standard deviation is never zero, but sharp features in the standard deviation indicate shifts and deformations between different energies, whereas smooth features mainly depict changes due the resonant effect of the phase shift which is physically correct. Figure 4.3.11 shows the overall improvement in the stack alignment: Whereas sharp lines are visible in the initial rigid alignment, in the final alignment mostly smooth features and significantly reduced sharp lines remain. This is confirmed by the line plots in Figure 4.3.11c1 and

4.3.11f1 related to the yellow line in Figure 4.3.11c and 4.3.11f, respectively. The standard deviation of the sharp features, which indicates misalignment, decreases by almost one order of magnitude from the rigid to the b-spline alignment. Further analysis revealed that remaining shifts and deformations between the reconstruction are maximal ± 1 px.

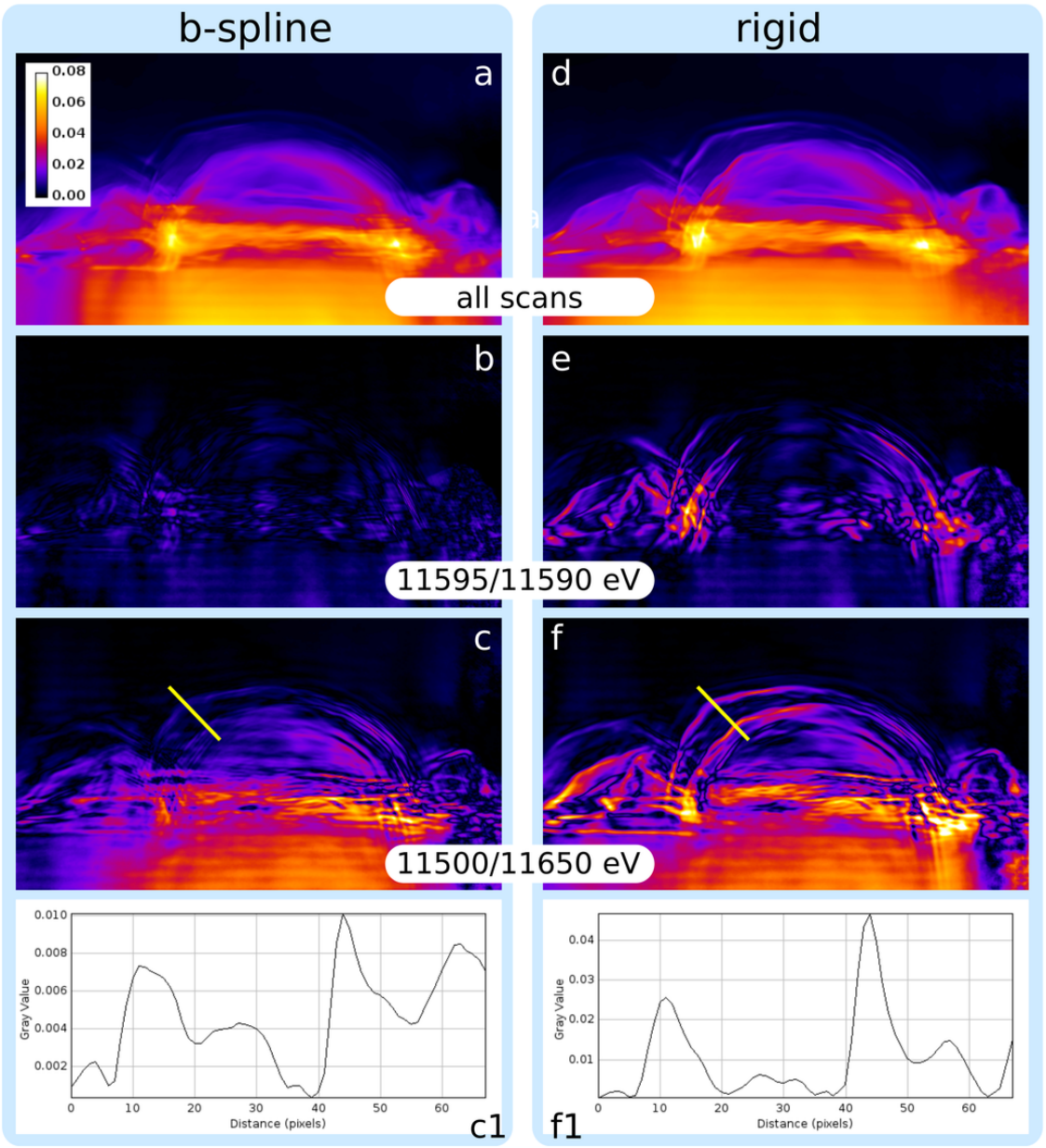

Figure 4.3.11: Comparison of the alignment quality. The best results were achieved by the b-spline algorithm (left column) subsequent to an affine (not shown) and initial rigid alignment (right column). a) and d) show the standard deviation of all scans. b) and e) show the standard deviation between two adjacent scans, where almost no resonance effect is expected. In this case, mainly misalignment influences the standard deviation. The same is true for c) and f) which show the difference between a pre- and a post-edge energy, expecting only a small resonant effect in the phase shift. The high standard deviation between those two scans, even in the area of the crystal depicts an offset in the phase shift, that is discussed later. c1 and f1) show the line plots from c) and f) illustrating the significant decrease of sharp features indicating an improved alignment.

4.3.7 Chemical Analysis

Up to now, all processing steps were required to prepare the chemical analysis of the sample. Only consistent reconstructions and a reasonable alignment allow to extract reliable chemical information from each pixel as function of energy. Similar to the catalyst model sample, first, 2D difference maps will show the general platinum distribution by the resonance effect at the Pt-L_2 edge. In addition, an advanced analysis tries to unravel the existence of oxidised platinum and its distribution in the 2D projection. Therefore, a simple fitting routine is introduced to model the phase shift data with reference curves from metallic and oxidised platinum.

Chemical Distribution in 2D Difference Maps

The first part of the chemical imaging procedure is the 2D visualization of the resonance effect at the Pt-L_3 edge similar to the analysis shown for the model sample in Section 4.2.5. For this purpose, the aligned phase shift reconstructions were used to create 2D difference maps. Fig. 4.3.12 shows such maps for the difference between several energies along the resonance edge. The reconstruction at an energy of $11\,504\,\mathrm{eV}$ served as reference. The 2D maps on the right in Fig. 4.3.12 depict the difference of the modulus of the phase shift between the reference and the energy indicated in the maps. In these difference images the platinum distribution is clearly visible, the brighter the color the thicker the sample and the stronger the resonance effect that increases until the maximum is reached at the edge energy. Actually, the crystal at the base of the sample should not show any resonance effect, instead this area also shows variations in the phase shift, which will be discussed later.

After this basic chemical analysis with the help of 2D difference maps, further evaluation is required to check for different oxidation states in the platinum layer.

Advanced Analysis of all Energies in the Spectrum

The basic chemical imaging with the help of the 2D difference maps only showed the platinum distribution in general. In order to localise different oxidation states in the platinum layer, an advanced analysis of the phase shift in each pixel is required. For this purpose, the phase shift values in the reconstructions of all energies are considered as a discrete spectrum in each pixel. The aim of a spectral analysis is now to determine the ratio between the metallic and oxidised parts in the sample.

In Chapter 1 Section 1.1.2, the complex atomic scattering factor was derived and it was found that it describes the *local* electronic structure in a sample. The scattering process of all atoms in a sample can be described by the structure factor which is the sum over all atoms taking part in the scattering process, cf. Equation 1.1.23. Consequently, a mixture of different oxidation states in the bulk material can be simply described by the superposition of all these different states weighted by their proportion.

In the specific case at hand, the phase shift values $\phi(E)$ in each pixel potentially depict a mixture. The phase shift depends on the length – the thickness of the sample – the wave passes through compared to a wave in vacuum. Here, it is not relevant whether a

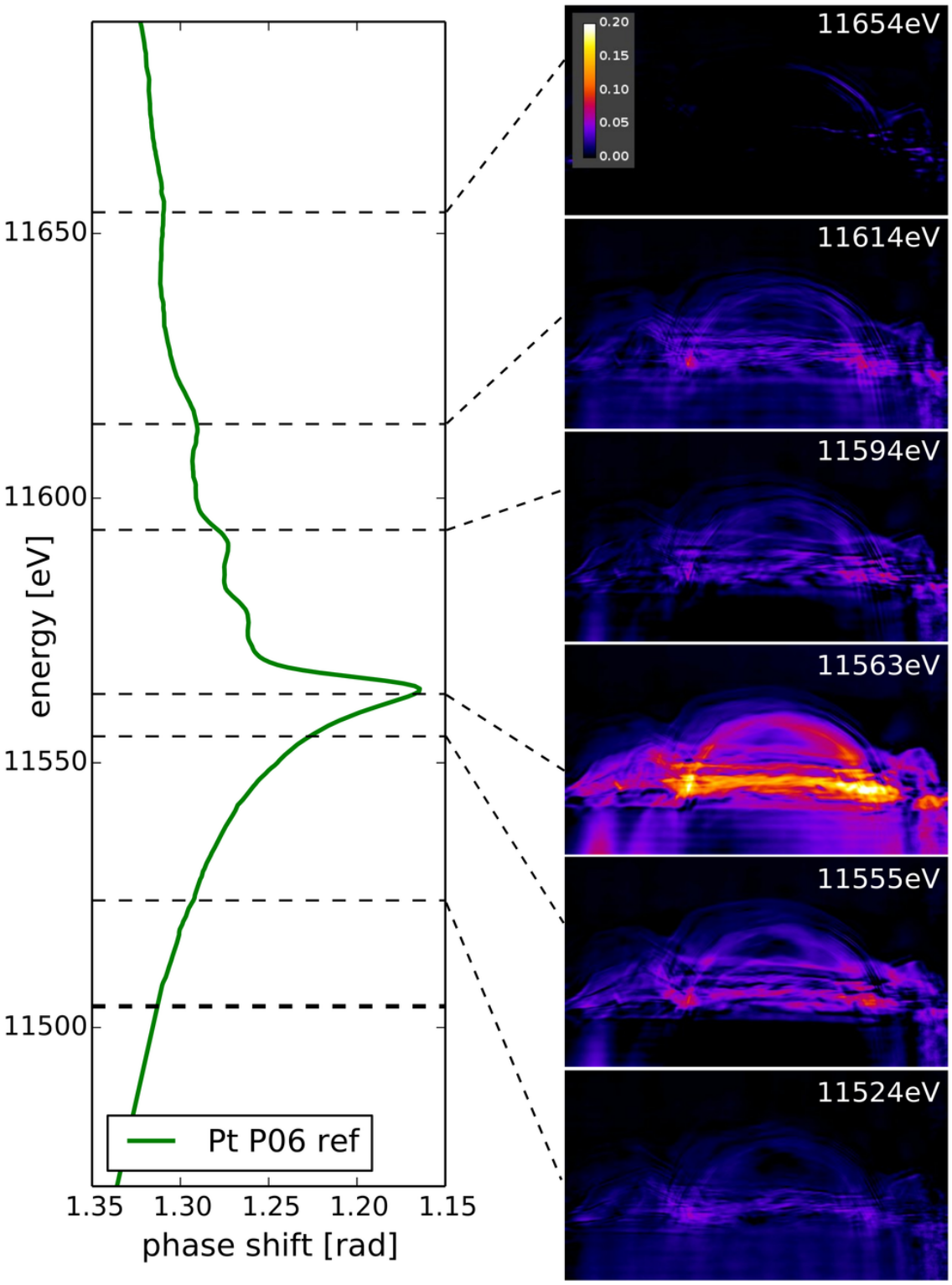

Figure 4.3.12: 2D Difference Maps for Chemical Imaging. The plot on the left shows a reference curve for metallic platinum at the Pt-L_3 edge. The horizontal lines mark the energies at which the 2D maps were created as difference to the reference. On the right, six 2D difference maps are shown exemplarily for different energies. The maximum of the resonance effect is clearly visible at an energy of $11\,563\,\mathrm{eV}$ compared to the reference.

material of a certain refractive index is solid or honeycombed with air or other materials, cf. Fig. 4.3.13. As a whole, only the actual thickness of each component in the projection

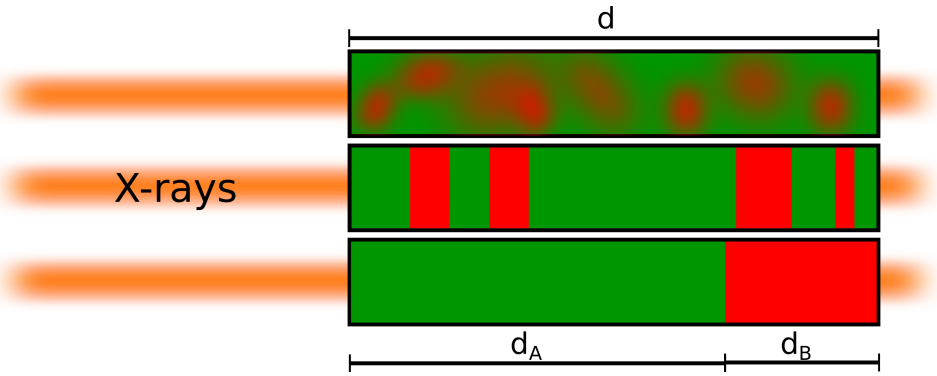

Figure 4.3.13: Scheme for the phase shift of a mixture. The phase shift caused by a mix of materials does not depend on the distribution along the projection direction. A homogeneous layer generates the same phase shift as several layers or a structured material of the same effective thickness.

direction contributes to the phase shift. Thus, the total phase shift $\phi(E)$ equals

$$\phi(E) \quad = \quad \underbrace{d_A \cdot A}_{=\phi_A} + \underbrace{d_B \cdot B}_{=\phi_B} + C, \tag{4.3.1}$$

where A and B are related to the real part δ of the refractive index, calculated from EXAFS reference measurements, given by δ_A for the metallic state or δ_B for the oxidised state, respectively:

$$A(E) = \frac{2\pi}{\lambda} \cdot \delta_A(E) \;\text{ and }\; B(E) = \frac{2\pi}{\lambda} \cdot \delta_B(E), \tag{4.3.2}$$

with λ as the wavelength corresponding to the photon energy E. In Equation (4.3.1), d_A and d_B represent the thickness of the metallic and the oxidised state, respectively, and C covers a potential non-resonant phase shift offset caused by other materials in the sample volume.

A superposition of spectra of the metallic state and oxidised state can be fit to the data points $\phi(E)$ in the spectrum of the phase shift reconstructions. In order to find the composition of metallic and oxidised platinum in the sample, the cost function F must be minimised,

$$F = \sum \left[\phi(E) - (d_A \cdot A + d_A \cdot B + C)\right] \;\rightarrow \text{min} \tag{4.3.3}$$

with d_A, d_B and C as optimisation parameters under the positivity constraint:

$$d_A, d_B, C \geq 0 \tag{4.3.4}$$

With the optimised output for d_A, d_B and C, the total thickness d of the sample along the projection direction as well as the percentages α and β for the metallic and oxidised state can be calculated. The offset C represents a phase shift and is in units of [rad], therefore it cannot be used to calculate the total thickness. If the phase shift offset in the fit is

orders of magnitude smaller than the phase shift values of the sample extracted from the reconstruction, it is negligible in the calculation of the total thickness.

$$d = d_A + d_B \tag{4.3.5}$$

$$\alpha = \frac{d_A}{d} \quad \text{and} \quad \beta = \frac{d_B}{d} \tag{4.3.6}$$

The method *least_squares*[86] included in the python library *scipy.optimize* was used to minimise F. This function requires an initial guess for the optimizing parameters, given as $d_A, d_B, C = 0$. The *Trust Region Reflective*[18] (trf) method was chosen as it allows for boundaries to the parameters, which where set to $[0, 1]$.

Fitting Each Pixel

The resonant data set provides a discrete spectrum $\phi(E_j)$ in each pixel. A fit to minimise the cost function, given in Equation (4.3.3), results in values for the thickness of the different states to approach the spectrum given by the phase shift values in the reconstructions. After this was done for each pixel of the reconstruction stack, Fig. 4.3.14a and 4.3.14c show the values d_A and d_B which were optimised via the least-squares fit indicating the amount of metallic and oxidised platinum in the sample. According to that, b) and d) depict the

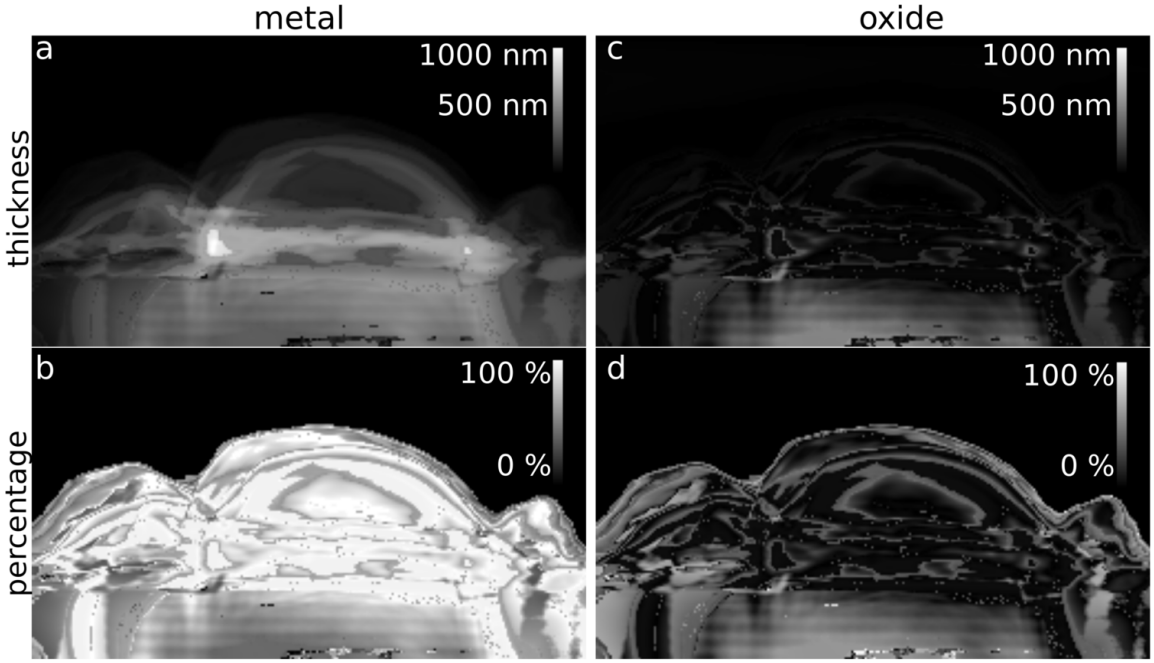

Figure 4.3.14: Thickness and percentage of the metallic and oxidised state as a result of the fit in each pixel. a) and c) illustrate the thickness of the metallic and oxidised state, respectively. In b) and d), the ratio of the metallic and oxidised material to the total sample thickness is shown as relative concentration α and β, respectively.

relative amount of each state in $\%$. As seen in Fig. 4.3.14d, areas of a significant amount of more than $20\,\%$ of the oxide phase can be localised. Since a ptychographic reconstruction is a 2D projection of the sample in the direction of the X-ray beam, it is most likely that each

pixel contains a mixture of metallic and oxidised platinum. A 3-dimensional resonant data set would allow for a more precise evaluation of the chemical distribution mainly limited by the effective voxel size. For comparison of the resulting distribution with the morphology of the sample, Fig. 4.3.15 shows a phase reconstruction with a red overlay that indicates areas with an amount of oxidised material in the projection larger than $20\,\%$.

Further analysis was required to check the reliability of the distribution obtained from the fit process. To do so, the phase shift as function of energy should be visualised together with the fit results. Based on the chemical distribution obtained by the fitting of all pixels as function of energy, cf. Fig. 4.3.15, different regions of interest (ROI) were selected in the ptychographic reconstruction.

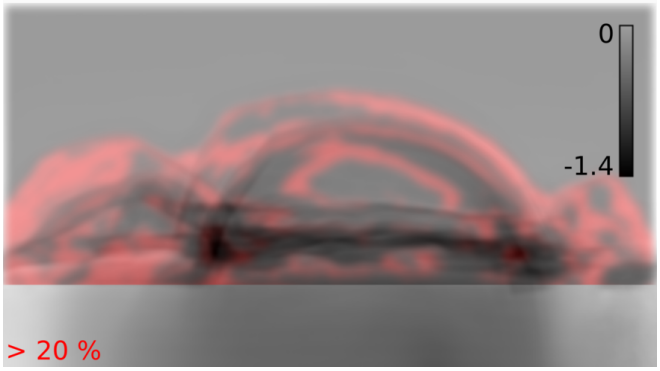

Figure 4.3.15: Ptychographic reconstruction of the platinum bubble. The red overlay indicates areas of oxidised material of more than $20\,\%$ according to the fit in each pixel. Calibration bar for the phase shift in [rad].

Different Regions-of-Interest

In each reconstruction, the values of the pixels in a ROI were averaged, which results in an average phase shift value as function of energy for each ROI. For 6 of these ROI, the phase shift curves as a function of energy are shown in Fig. 4.3.16. All ROI M plus a number indicate potential metallic areas and all ROI O plus a number indicate potential oxidised areas. The colours of the plots correspond to the colour that marks a ROI in the phase reconstruction. On the bottom left, the measurement in an area in the crystal marked in white is shown. This black curve demonstrates the variation of the phase shift as a general offset which is not caused by any resonance effect. Therefore, the values of the crystal were used for the normalisation of the phase shift values before the fitting procedure. This variation was already seen in Figure 4.3.12 and is considered as an artefact in the stack of ptychographic reconstructions. Despite the normalisation of the phase shift values, strong variations between adjacent scan points still occur in every ROI. A reason for that is probably the acquisition scheme of the ptychograms at different energies. During the experiment, the ptychographic scans of the resonant data set were not recorded along the increasing photon energy in a row, instead the data acquisition was split in three parts: First, ptychograms at the energies, marked by the green circles in the curves in Fig. 4.3.17 were recorded increasing the energy at a step size of $2\,\mathrm{eV}$. More scans were recorded, marked in red, to fill up ptychograms at missing energies to achieve better sampling.

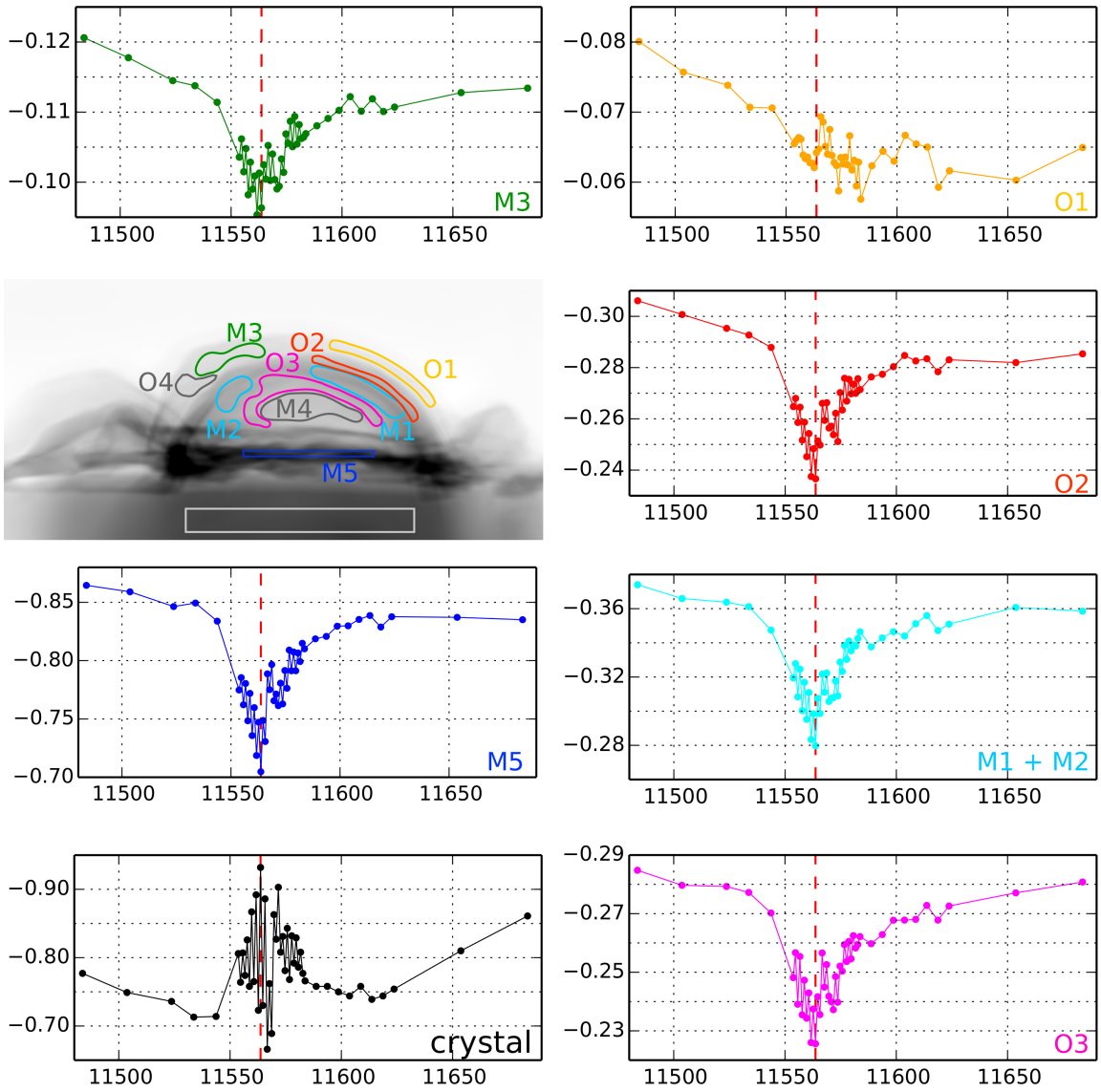

Figure 4.3.16: Different ROI are marked in the Pt bubble reconstruction and the corresponding phase shift values are plotted. The ROI were chosen based on the distribution gained by the fit of the spectrum in each pixel. M1 to M5 indicate areas where the metallic state is expected and O1 to O4 indicates areas with a potentially oxidised percentage larger than 20 %. The coloured plots show the normalised average phase shift in each ROI of the same color. The black curve shows the average phase shift in the area marked in white in the crystal area, that serves for normalization.

The energy was increasing using a step size of 2 eV until 11 582.7 eV and 5 eV afterwards. Finally, ptychograms at pre-edge energies were recorded as shown by the blue circles with decreasing energy. This course of action was chosen similarly to the *Golden Angle Principle* in tomography experiments, where the angles of the projections are chosen in a way that the maximum angular resolution could be achieved no matter when the scan must be stopped. Here, it was tried to first cover some energies around the edge and to improve the sampling if time permits. Unfortunately, it is most likely that the experimental conditions changed and that the scan points are subject to a varying phase shift offset. Two different

effects are considered to create these varying offset: First, the monochromator might not move perfectly. Consequently, the angular position is slightly different leading to a slightly different energy as well as to a different beam position. And second, a form of radiation damage was observed over the total experiment duration. This can be seen as an additional layer growing in the phase reconstructions from the first resonant ptychogram to the last one. Since, the experiment was performed in air atmosphere, it can be assumed, that this layer is made of carbon. In some areas of the sample this layer adds a phase shift of up to 50 mrad to the phase reconstruction. This modification of the sample massively impaired the analysis of the resonant data set. Due to this inconsistency in the data acquisition, the fitting procedure was performed including all energies as well as only including the energies of the first and the second sub-scan separately.

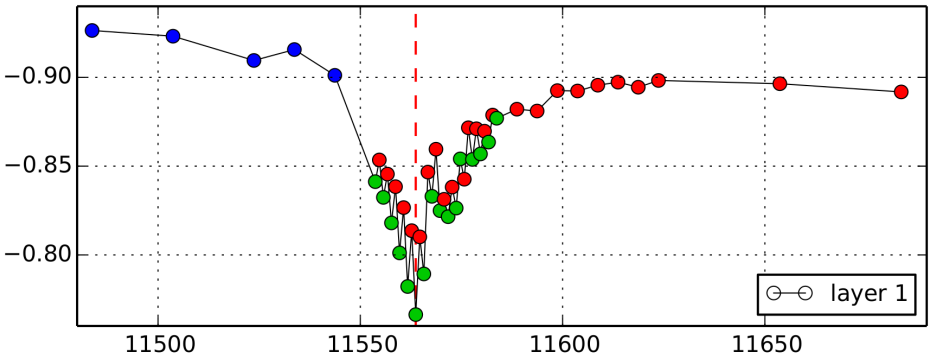

Figure 4.3.17: Correlation on phase shift variations and the scan order. First, ptychograms were recorded at the energies marked in green, increasing the energy in steps of 2 eV. Second, ptychograms at the energies marked in red were recorded with the same step size for increasing energy. Last, ptychograms at the energies marked by the blue circles were recorded with decreasing energy. This behaviour of the phase shift is similar for all regions in the scan.

In Table 4.3.2, the results for the amount of oxidised material are compared for the different ROI and for the three different fits considering *all scans*, only the *first set of scans* or only the *second set of scans*. No significant difference was found between the different fits. The thickness of metallic and oxidised material along the projection that was calculated using all energy scans are also given in this table.

4.3.8 Discussion of the Fit Results

The phase shift values measured in the different ROI are shown as a function of energy in Fig. 4.3.18, 4.3.19 and 4.3.20, together with the fit functions for a mixture (mix in orange) based on the calculated ratio of both states as well as with a purely metallic reference (metal in green) and a purely oxidised reference (oxi in red). As expected from the data quality, the fits show a large uncertainty especially in the energy range from 11 567 eV to 11 580 eV where the main difference between the pure metallic and pure oxidised reference is present in the curve profile.

In ROI $O1$, shown in Fig. 4.3.18, the sample is relatively thin with a low phase shift about

Table 4.3.2: Amount of the oxidised phase in % for the fits of the different half data sets and the thickness of the material in projection direction.

ROI	amount oxide (all scans)	amount oxide (first scans)	amount oxide (second scans)	thickness metal [nm]	thickness oxide [nm]
M1	5 %	5 %	5 %	260	13
M2	5 %	5 %	5 %	240	13
M3	9 %	6 %	9 %	80	7
M4	2 %	2 %	4 %	160	4
M5	2 %	0 %	3 %	640	13
O1	37 %	36 %	34 %	40	23
O2	37 %	39 %	38 %	170	97
O3	40 %	32 %	39 %	150	100
O4	42 %	45 %	40 %	80	58

80 mrad. In this range, the resonant effect of maximal 15 mrad is not visible since it is below the detection limit given by the phase shift variations. For this ROI, the deviation of the phase shift values from the fit are as large as ± 10 mrad. Thus, the fitting routine minimises the cost function but the result does not correspond to the physical resonance effect. For the ROI $O2$, shown in Fig. 4.3.19, the resonance effect of more than 40 mrad is clearly visible and the different fit functions are reasonable. Close to the absorption edge, the deviation of the phase shift values from the fit are in the range of up to ± 10 mrad. The maximum phase shift differences for either a metallic or a fully oxidised platinum layer, i.e., the maximal difference between green and red reference curve, is approximately 15 mrad. Since the phase shift values are an average along the projection direction it is very unlikely that a fully oxidised layer can be seen and the expected maximum phase shift difference is even lower. Thus, the variance in the phase shift values is still so large that the significance of the fits for an oxidised percentage is doubtful. For comparison, Fig. 4.3.20 shows the phase shift values of the ROI $M5$, which depicts a metallic area. Here, a similar phase shift curve is seen as for the potentially oxidised ROI. With this, it becomes clear that better data quality is required in order to make a reliable statement on the chemical distribution of the sample. Since no further significant differences are present in other ROI, the phase shift curves and fit results of those ROI are not shown here, but can be found in the Appendix B.

Based on the fits in the different ROI, the chemical distribution that was initially achieved by fitting each pixel in the stack of reconstructions, illustrated in Figure 4.3.15, should be reviewed: The existence of multiple oxidised and metallic layers on top of each other cannot be approved, since the outer layers are to thin resulting in a phase shift too low to show a resonance effect with detectable differences between the metallic and the oxidised state.

In conclusion, it is found, that a precise determination of the amount of oxidised material is not possible regarding the large variations in the data set and the resulting error-proneness of the fitting routine. Nevertheless, the incidence of locally connected areas where the fit results show a larger amount of oxidised platinum confirms the results achieved from the electron microscopy images. Thus, the analysis of the resonant ptychography supports the assumption of the existence of different oxidation states in platinum layer.

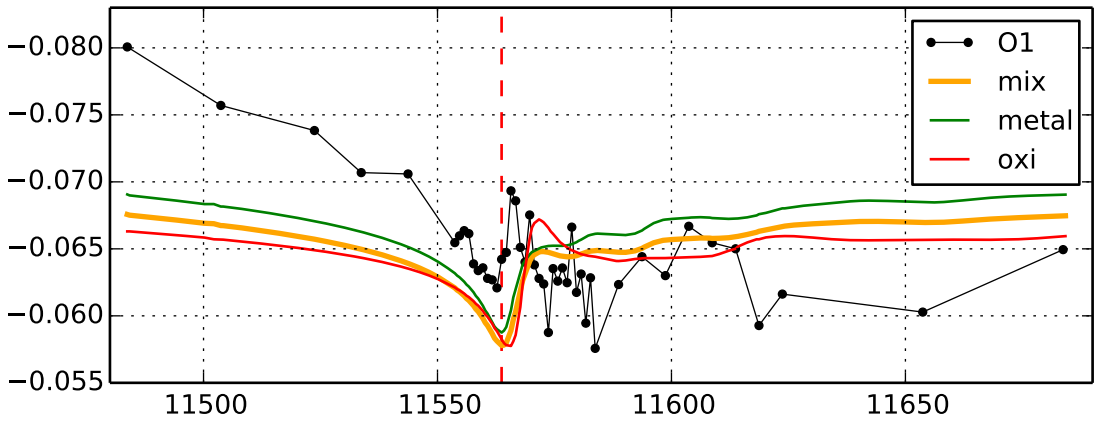

(a) all scan points

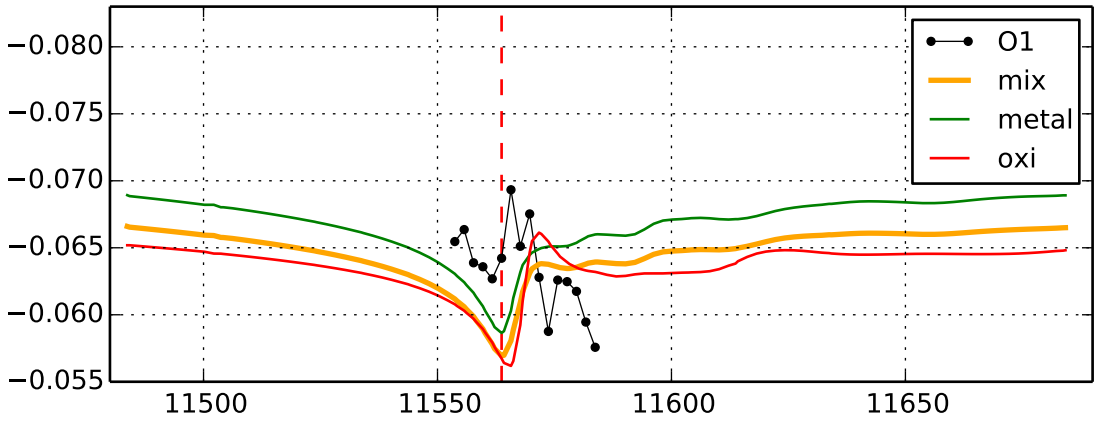

(b) first scan set

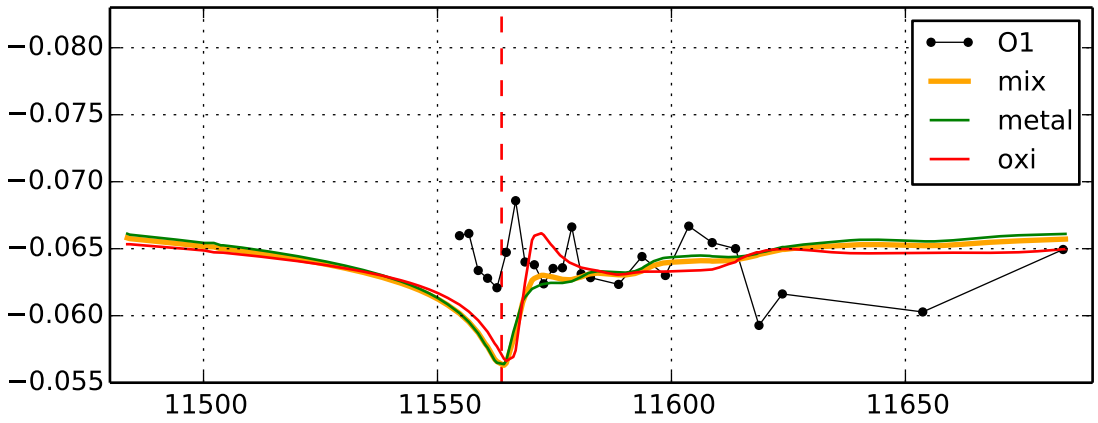

(c) second scan set

Figure 4.3.18: **Fit for the ROI *O1*, for all scans and for the first and second scan set separately.** The phase shift in the outer shell of the Pt bubble covered by the ROI *O1* is comparatively weak down to less than 60 mrad consequently the resonant effect cannot be detected over the deviations of the phase shift values.

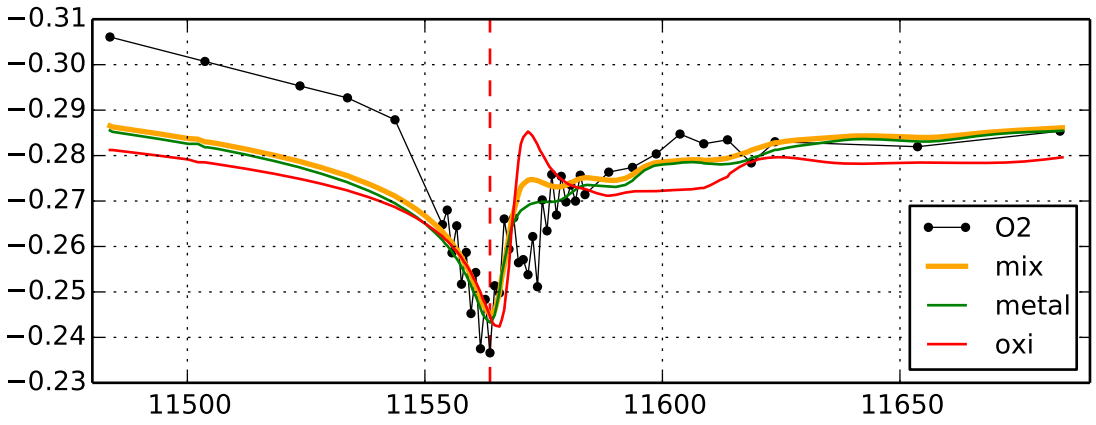

(a) all scan points

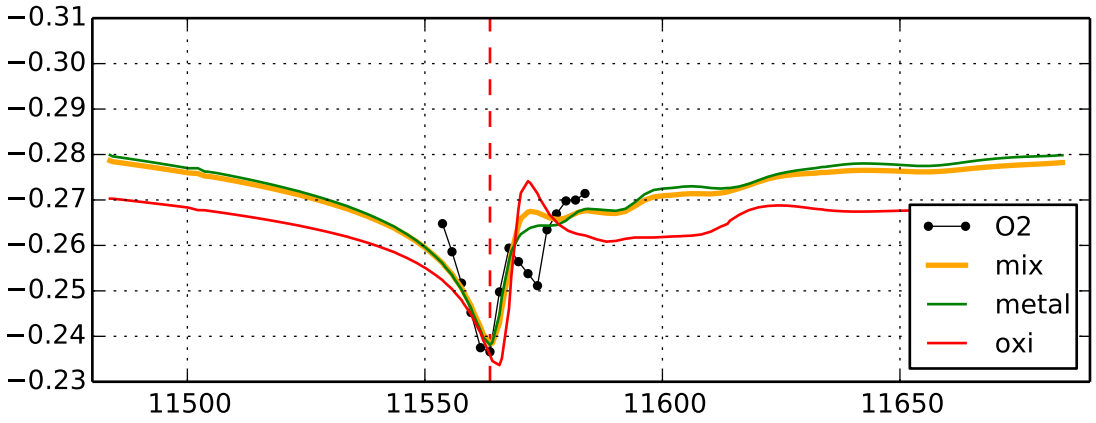

(b) first scan set

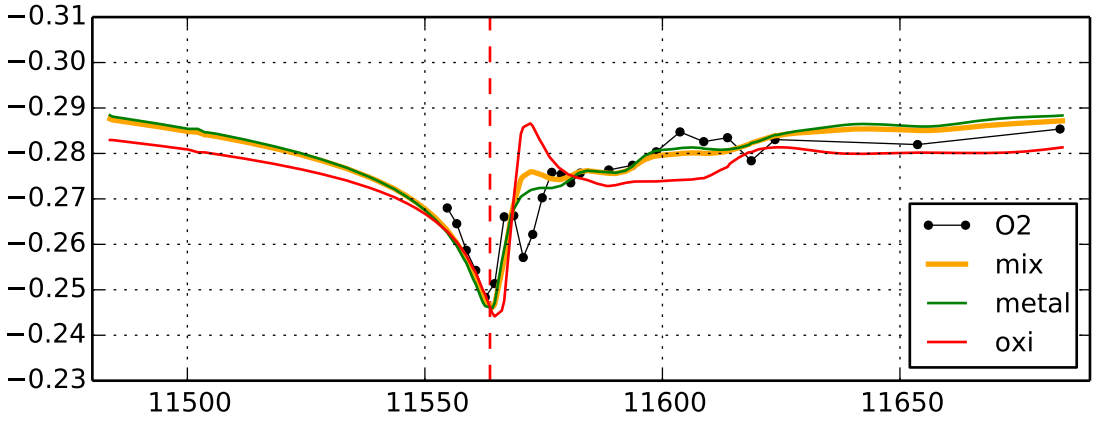

(c) second scan set

Figure 4.3.19: Fit for the ROI *O2*, for all scans and for the first and second scan set separately. For a stronger phase shift in the ROI *O2*, the resonance effect is detectable. Nevertheless, the difference between the reference fits and the data points is still high, which diminishes the reliability on the chemical composition obtained by the fits.

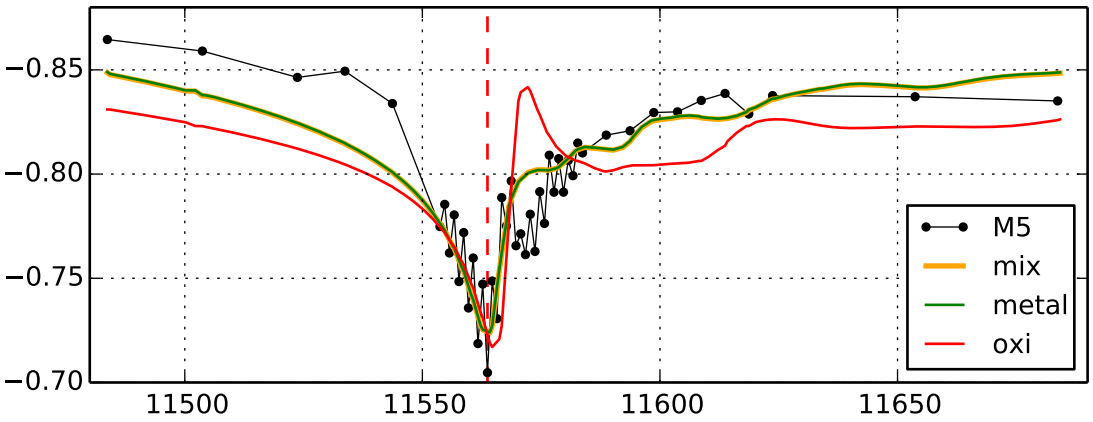

(a) all scan points

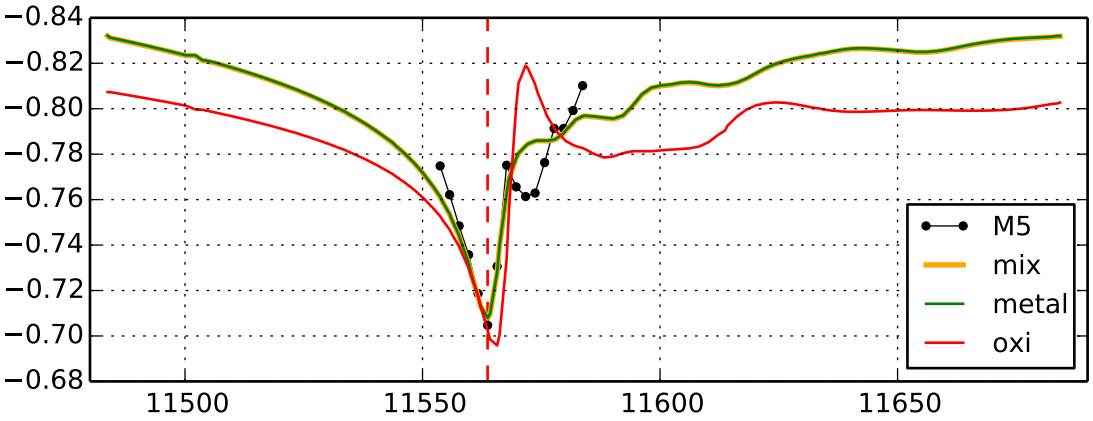

(b) first scan set

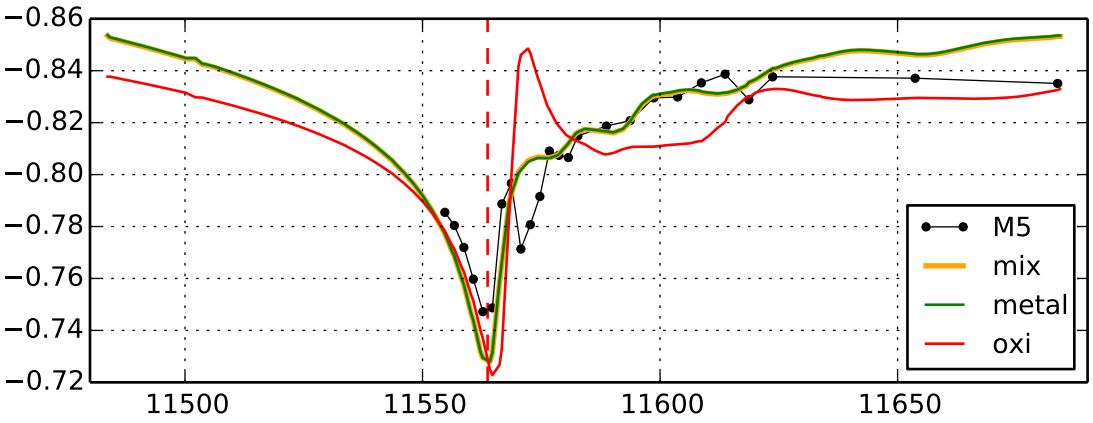

(c) second scan set

Figure 4.3.20: Fit for the ROI *M2*, for all scans and for the first and second scan set separately. For a stronger phase shift in the ROI *M2*, the resonance effect is detectable. However, the difference between the reference fits and the data points is similarly large as in the fits for ROI $O2$, which diminishes the reliability on the chemical composition obtained by the fits.

5 Conclusion and Outlook

Using resonant ptychography as a tool for chemical imaging, not only demands high spatial resolution and sensitivity especially for nano materials, but also requires reliable quantitative reconstructions. In this work, the opportunities and limitations of resonant hard X-ray ptychography for quantitative chemical imaging of nano materials were investigated.

Since ptychography has been established as a high-resolution imaging tool in recent years, it was expected to provide quantitative information on any kind of sample with high spatial resolution if only the photon dose was sufficient. Instead, the more complex the sample and experimental conditions get, the more challenges occurred, even with strongly scattering samples. Besides the limitation in spatial resolution by the photon flux, the reconstruction quality is also influenced by the stability of the experimental setup as well as by parasitic scattering from air, windows and the detector material itself. Whereas ideal data sets (simulations) usually lead to perfect reconstruction results without further constraints to the object or probe function, real data sets do not necessarily fulfil all the assumption of the basic ptychographic model. Potential deviations from the model are limited redundancy in the scattering information due to poor sampling and incoherent background, a non-constant incident probe function, vibrating objects and other varying experimental conditions.

In a first step of this work, the standard resolution chart, the Siemens star, served as a strongly scattering sample. Here, it became already apparent, that quantitative imaging demands more information than only the diffraction patterns and the corresponding scan positions. A critical analysis of the reconstruction process uncovered ambiguities in the basic ptychographic algorithm: The intensity of the probe function did not converge but decreased with the number of iterations, thus leading to an incorrect reconstruction of the object function. This issue could be solved by providing the intensity of the incident beam as a constraint to the reconstructed probe function. Preferably, the intensity should be measured by a PIN diode directly upstream of the sample. If this is not applicable, flat field diffraction patterns of the scan itself can be used to extract this constraint value of the probe function. This observation emphasises that the ptychographic reconstruction algorithm is not as robust as expected and requires additional a-priori information to achieve quantitative results out of real data sets. Here, the incident probe turned out to be the critical point in the ptychographic model, as precise knowledge of the incoming beam is important for a reliable reconstruction even of strongly scattering samples like the Siemens star. The normalisation of diffraction patterns was not sufficient, thus, a consistent reconstruction with a reasonable probe function depends on additional constraints to the probe right from the start. Furthermore, it was recognised that only the convergence of the error function does not guarantee a reliable reconstruction result. The awareness of these potential ambiguities in the reconstruction was important for the subsequent analysis as the modifications of the algorithm were directly applied to the catalyst model sample leading to quantitative results.

One of the main aims of this work was the enhancement of the spatial resolution and the sensitivity to weakly scattering samples with regard to chemical imaging. An essential aspect for high-resolution imaging using coherent diffraction is the detection of signal in high scattering angles over noise and over background scattering. To improve the data quality in terms of the signal-to-background ratio, an opaque beamstop was implemented into the experimental setup to suppress parasitic background scattering. Together with the application of a dual-exposure scheme and the simultaneous ptychographic reconstruction of two datasets – one with and one without an opaque beamstop – quantitative images of the weakly scattering sample were achieved with high spatial resolution better than $15\,\mathrm{nm}$ and high sensitivity to less than 10^5 atoms as published in Reinhardt et al. [2017]. It was shown, that high-resolution reconstructions necessitate the enhancement of the signal-to-background ratio by suppressing the background instead of just increasing the photon flux which leads to an overall increased scattering including the parasitic scattering. However, the results of the combined reconstruction were still not applicable for the chemical analysis as the reconstructions at different energies were subject to positioning errors and drifts between the scans. With the simultaneous reconstructions of two scans, the importance of precise knowledge of the scan positions became clearer than ever before. Only with the use of the position correction algorithm, cf. Schroer [2017], could the reconstruction be brought to a consistent level that was useful for further chemical analysis. After the removal of the positioning errors, the initial aim to extract the information about the chemical distribution of gold and platinum in the sample from the resonant data set succeeded.

Resonant ptychography found another application in the investigation of different oxidations states of the platinum bubble. In comparison to the catalyst model sample, the platinum bubble is a strongly scattering sample producing a relatively strong contrast in phase shift. Thus, the general platinum distribution could easily be determined due to the large resonance effect. The distinction between different oxidation states, however, requires very high data quality and phase shift sensitivity, since the difference in the phase shift between a metallic state and a mixed metallic-oxidised state is minor. All knowledge gained from the previous experiments was exploited to optimize the results of the chemical analysis. Again, the importance of precise positioning was confirmed during the Pt bubble analysis. The reconstructions measured at different energies showed distortions due to erroneous positions and sample drifts. These distortions obstructed the chemical imaging analysis. For the Pt bubble, the position correction algorithm did not work out as well as it did for the catalyst model sample. Therefore, in the post-processing, alignment procedures from medical imaging were used to achieve a reasonably aligned data stack for the different energies around the platinum resonance edge. Additionally, variations in the phase shift between the reconstructions at different energies complicated the determination of different oxidation states in the sample. The origin of these variation was not completely uncovered but inconsistent photon energies as well as radiation damage by carbon deposition are most likely. As a consequence, the least-square fits were hardly able to handle the major differences in phase shift, which were not due to the actual resonance effect. Finally, even though the actual distribution of oxidised platinum could not be proven with certainty, the analysis of the resonant data set supports the assumptions for an oxidised layer as found by the preceding electron microscopy investigations.

In future experiments, consistent experimental conditions are essential: The ptychographic reconstruction at different energies have to be recorded in sequence to avoid discrepancies originating from erroneous monochromator positions. In addition, potential carbon deposition and other kinds of radiation damage should be avoided. For this purpose, a sample environment in an inert gas atmosphere such as helium or nitrogen is conceivable. In order to ensure a correct normalisation and quantitative values in the reconstruction, a calibrated intensity detector should be placed directly upstream of the sample to continuously monitor the beam intensity. Besides the monitoring of the beam intensity, beam position monitors would facilitate even more control of the experimental conditions that are essential for consistent results. Furthermore, the positions of the sample during the ptychographic scans will be controlled by an interferometer system. Such a system has recently been installed at beamline P06. Future work, should also extent the resonant data set to tomographic measurement to achieve the chemical information in three dimensions. With all these improvements, an investigation of different oxidation states in heterogeneous specimen will become more reliable.
In brief, the key findings of this work are:

- Setting physical constraints to the ptychographic algorithm is necessary in order to achieve reliable quantitative results. Especially the intensity and position of the incoming beam should be continuously monitored.
- High-resolution and high-sensitivity reconstructions can be achieved by suppressing parasitic background scattering using an opaque beamstop and a double-exposure scheme.
- The knowledge and control of the actual scan positions are crucial in order to achieve highest spatial resolution without artificial distortions.

List of Figures

Bibliography

[1] Abbe, E. (1873). Beiträge zur Theorie des Mikroskops und der mikroskopischen Wahrnehmung. *Archiv für mikroskopische Anatomie*, 9:413 – 468. (Cited on page 1.)

[2] Als-Nielsen, J. and McMorrow, D. (2011). *Elements of Modern X-ray Physics*. Wiley. (Cited on pages 5, 11, 13, 17 and 22.)

[3] Attwood, D. (2007). *Soft X-Rays and Extreme Ultraviolet Radiation: Principles and Applications*. Cambridge University Press. (Cited on pages 5, 13, 16 and 51.)

[4] Baier, S., Damsgaard, C. D., Scholz, M., Benzi, F., Rochet, A., Hoppe, R., Scherer, T., Shi, J., Wittstock, A., Burghammer, M., Wagner, J. B., Schroer, C. G., and Grunwaldt, J.-D. (2016). *In situ* ptychography of heterogeneous catalysts using hard X-rays: high resolution imaging at ambient pressure and elevated temperature. *Microsc. Micoanal.*, 22(1):178 – 188. (Cited on page 2.)

[5] Banterle, N., Bui, K. H., Lemke, E. A., and Beck, M. (2013). Fourier ring correlation as a resolution criterion for super-resolution microscopy. *Journal of Structural Biology*, 183(3):363 – 367. (Cited on page 43.)

[6] Barty, A., Marchesini, S., Chapman, H. N., Cui, C., Howells, M. R., Shapiro, D. A., Minor, A. M., Spence, J. C. H., Weierstall, U., Ilavsky, J., Noy, A., Hau-Riege, S. P., Artyukhin, A. B., Baumann, T., Willey, T., Stolken, J., van Buuren, T., and Kinney, J. H. (2008). Three-dimensional coherent x-ray diffraction imaging of a ceramic nanofoam: Determination of structural deformation mechanisms. *Phys. Rev. Lett.*, 101:055501. (Cited on page 2.)

[7] Baruchel, J. (1994). *Neutron and synchrotron radiation for condensed matter studies: Applications to solid state physics and chemistry*. Neutron and Synchrotron Radiation for Condensed Matter Studies. Springer-Verlag. (Cited on page 51.)

[8] Beckers, M., Senkbeil, T., Gorniak, T., Reese, M., Giewekemeyer, K., Gleber, S.-C., Salditt, T., and Rosenhahn, A. (2011). Chemical contrast in soft x-ray ptychography. *Phys. Rev. Lett.*, 107(20):208101. (Cited on page 2.)

[9] Beckhoff, B., Kanngießer, B., Langhoff, N., Wedell, R., and Wolff, H. (2007). *Handbook of Practical X-Ray Fluorescence Analysis*. Springer ebook collection / Chemistry and Materials Science 2005-2008. Springer Berlin Heidelberg. (Cited on page 55.)

[10] Bergevin, F. D. and Brunel, M. (1972). Observation of magnetic superlattice peaks by X-ray diffraction on an antiferromagnetic NiO crystal. *Physics Letters A*, 39(2):141 – 142. (Cited on page 5.)

[11] Biggs, F. and Lighthill, R. (1988). Analytical approximations for X-ray cross sections III. *Sand87-0070:*. (Cited on page 41.)

[12] Bogan, M. J., Benner, W. H., Boutet, S., Rohner, U., Frank, M., Barty, A., Seibert, M. M., Maia, F., Marchesini, S., Bajt, S., Woods, B., Riot, V., Hau-Riege, S. P., Svenda, M., Marklund, E., Spiller, E., Hajdu, J., and Chapman, H. N. (2008). Single particle x-ray diffractive imaging. *Nano Lett.*, 8(1):310–316. (Cited on page 2.)

[13] Bohr, J. (1990). Magnetic x-ray scattering: A new tool for magnetic structure investigations. *Journal of Magnetism and Magnetic Materials*, 83(1):530 – 534. (Cited on page 5.)

[14] Bohren, C. F. (2010). What did Kramers and Kronig do and how did they do it? *European Journal of Physics*, 31(3):573. (Cited on page 16.)

[15] Born, M. and Wolf, E. (1999). *Principles of Optics*. Cambridge University Press, Cambridge. (Cited on page 18.)

[16] Bunk, O., Dierolf, M., Kynde, S., Johnson, I., Marti, O., and Pfeiffer, F. (2008). Influcence of the overlap parameter on the convergence of the ptychographical iterative engine. *Ultramicroscopy*, 108(5):481–487. (Cited on page 34.)

[17] Center for X-ray Optics (2014). CXRO: X-ray interactions with matter. http://henke.lbl.gov/optical_constants/. (Cited on page 41.)

[18] Conn, A., Gould, N., and Toint, P. (2000). *Trust Region Methods*. MPS-SIAM Series on Optimization. Society for Industrial and Applied Mathematics. (Cited on page 89.)

[19] de L. Kronig, R. (1926). On the theory of dispersion of x-rays. *J. Opt. Soc. Am.*, 12(6):547–557. (Cited on page 16.)

[20] Dectris (Accessed January 16, 2017a). EIGER 4M. https://www.dectris.com/EIGER_X_Specifications.html. (Cited on page 56.)

[21] Dectris (Accessed January 16, 2017b). Pilatus 300k. https://www.dectris.com/tl_files/root/news/20111122/Pilatus_300K_20Hz_web_a4.pdf. 1. Generation. (Cited on page 56.)

[22] Deng, J., Vine, D. J., Chen, S., Nashed, Y. S. G., Jin, Q., Phillips, N. W., Peterka, T., Ross, R., Vogt, S., and Jacobsen, C. J. (2015). Simultaneous cryo x-ray ptychographic and fluorescence microscopy of green algae. *Proceedings of the National Academy of Sciences*, 112(8):2314–2319. (Cited on page 2.)

[23] Dierolf, M., Thibault, P., Menzel, A., Kewish, C. M., Jefimovs, K., Schlichting, I., von König, K., Bunk, O., and Pfeiffer, F. (2010). Ptychographic coherent diffractive imaging of weakly scattering specimens. *New Journal of Physics*, 12(3):035017. (Cited on page 2.)

[24] Donnelly, C., Guizar-Sicairos, M., Scagnoli, V., Holler, M., Huthwelker, T., Menzel, A., Vartiainen, I., Müller, E., Kirk, E., Gliga, S., Raabe, J., and Heyderman, L. J. (2015). Element-specific x-ray phase tomography of 3d structures at the nanoscale. *Phys. Rev. Lett.*, 114:115501. (Cited on page 2.)

[25] Donnelly, C., Scagnoli, V., Guizar-Sicairos, M., Holler, M., Wilhelm, F., Guillou, F., Rogalev, A., Detlefs, C., Menzel, A., Raabe, J., and Heyderman, L. J. (2016). High-resolution hard x-ray magnetic imaging with dichroic ptychography. *Phys. Rev. B*, 94:064421. (Cited on page 2.)

[26] Enders, B., Dierolf, M., Cloetens, P., Stockmar, M., Pfeiffer, F., and Thibault, P. (2014). Ptychography with broad-bandwidth radiation. *Appl. Phys. Lett.*, 104(17):171104. (Cited on page 37.)

[27] Faulkner, H. M. L. and Rodenburg, J. M. (2004). Movable aperture lensless transmission microscopy: A novel phase retrieval algorithm. *Phys. Rev. Lett.*, 93:023903. (Cited on page 2.)

[28] Giewekemeyer, K., Thibault, P., Kalbfleisch, S., Beerlink, A., Kewish, C. M., Dierolf, M., Pfeiffer, F., and Salditt, T. (2010). Quantitative biological imaging by ptychographic x-ray diffraction microscopy. *P. Natl. Acad. Sci. USA*, 107(2):529–534. (Cited on page 2.)

[29] Gorelick, S., Vila-Comamala, J., Guzenko, V. A., Barrett, R., Salomé, M., and David, C. (2011). High-efficiency Fresnel zone plates for hard X-rays by 100 keV e-beam lithography and electroplating. *Journal of Synchrotron Radiation*, 18(Pt 3):442–446. (Cited on page 53.)

[30] Grunwaldt, J.-D. and Baiker, A. (2005). In situ spectroscopic investigation of heterogeneous catalysts and reaction media at high pressure. *Phys. Chem. Chem. Phys.*, 7:3526–3539. (Cited on page 47.)

[31] Grunwaldt, J.-D. and Schroer, C. G. (2010). Hard and soft x-ray microscopy and tomography in catalysis: Bridging the different time and length scales. *Chem. Soc. Rev.*, 39:4741. (Cited on page 39.)

[32] Hamamatsu (Accessed January 23, 2017). Photo Diode without Scintillator (not available anymore). http://www.hamamatsu.com. (Cited on page 55.)

[33] Hansen, T. and Wagner, J. (2015). *Controlled Atmosphere Transmission Electron Microscopy: Principles and Practice*. Springer International Publishing. (Cited on page 1.)

[34] Hecht, E. (2002). *Optics*. Addison-Wesley. (Cited on pages 5 and 53.)

[35] Hegerl, R. and Hoppe, W. (1970). Dynamische Theorie der Kristallstrukturanalyse durch Elektronenbeugung im inhomogenen Primärstrahlwellenfeld. *Ber. Bunsen-Ges. Phys. Chem.*, 74:1148. (Cited on page 2.)

[36] Hell, S. W. (2003). Toward fluorescence nanoscopy. *Nat Biotech*, 21(11):1347–1355. (Cited on page 1.)

[37] Henke, B. L., Gullikson, E. M., and Davis, J. C. (1993). X-ray interactions: photoabsorption, scattering, transmission, and reflection at E=50-30000 eV, Z=1-92. Atomic Data and Nuclear Data Tables. Vol. 54 (no.2), 181-342. (Cited on pages 21 and 41.)

[38] Hippert, F., Geissler, E., Hodeau, J. L., Lelièvre-Berna, E., and Regnard, J.-R., editors (2006). *Neutron and X-ray Spectroscopy*. Springer Netherlands. (Cited on pages 10, 38 and 39.)

[39] Hitachi High-Technologies (Accessed January 18, 2017). Vortex®-EM. http://www.hitachi-hightech.com/hhs-us/product_detail/?pn=ana-vortex-em. (Cited on page 55.)

[40] Hofmann, G. H. (2015). *Development of Methods and Devices for Spatially and TeTemporal Resolved X-Ray Microscopy for Characterization in Heterogeneous Catalysis*. PhD thesis, Fakultät für Chemie und Biowissenschaften, Karlsruher Institut für Technologie (KIT). (Cited on page 67.)

[41] Hönig, W. (2010). Portierung einer Ptychographie-Anwendung auf das CUDA GPU-Modell. Großer Beleg - TU Dresden Fakultät, Informatik, Institut für Technische Informatik. (Cited on page 80.)

[42] Hoppe, R. (2017). . PhD thesis, Technische Universität Dresden. (Cited on page 80.)

[43] Hoppe, R., Reinhardt, J., Hofmann, G., Patommel, J., Grunwaldt, J.-D., Damsgaard, C. D., Wellenreuther, G., Falkenberg, G., and Schroer, C. G. (2013). High-resolution chemical imaging of gold nanoparticles using hard x-ray ptychography. *Appl. Phys. Lett.*, 102(20):203104. (Cited on pages 2 and 77.)

[44] Huang, X., Yan, H., Harder, R., Hwu, Y., Robinson, I. K., and Chu, Y. S. (2014). Optimization of overlap uniformness for ptychography. *Opt. Express*, 22(10):12634–12644. (Cited on page 34.)

[45] Huang, X., Yan, H., Nazaretski, E., Conley, R., Bouet, N., Zhou, J., Lauer, K., Li, L., Eom, D., Legnini, D., Harder, R., Robinson, I. K., and Chu, Y. S. (2013). 11 nm hard x-ray focus from a large-aperture multilayer laue lens. *Scientific Reports*, 3:3562–. (Cited on page 1.)

[46] Hura, G. L., Menon, A. L., Hammel, M., Rambo, R. P., Poole II, F. L., Tsutakawa, S. E., Jenney Jr., F. E., Classen, S., Frankel, K. A., Hopkins, R. C., jae Yand, S., Scott, J. W., Dillard, B. D., Adams, M. W. W., and Tainer, J. A. (2009). Robust, high-throughput solution structural analyses by small angle X-ray scattering (SAXS). *Nature Methods*, 6(8):606–612. (Cited on page 1.)

[47] Jefimovs, K., Vila-Comamala, J., Pilvi, T., Raabe, J., Ritala, M., and David, C. (2007). Zone-doubling technique to produce ultrahigh-resolution x-ray optics. *Phys. Rev. Lett.*, 99:264801. (Cited on page 1.)

[48] Jones, M. W. M., Elgass, K., Junker, M. D., Luu, M. B., Ryan, M. T., Peele, A. G., and van Riessen, G. A. (2014). Mapping biological composition through quantitative phase and absorption X-ray ptychography. *Scientific Reports*, 4:6796–. (Cited on page 2.)

[49] Keyence (Accessed December 11, 2016). Optical microscope. http://www.keyence.com/products/microscope/digital-microscope/vhx-900/models/vh-z100ur/index.jsp. (Cited on page 54.)

[50] Kisielowski, C., Freitag, B., Bischoff, M., van Lin, H., Lazar, S., Knippels, G., Tiemeijer, P., van der Stam, M., von Harrach, S., Stekelenburg, M., Haider, M., Uhlemann, S., Müller, H., Hartel, P., Kabius, B., Miller, D., Petrov, I., Olson, E., Donchev, T., Kenik, E., Lupini, A., Bentley, J., Pennycook, S., Anderson, I., Minor, A., Schmid, A., Duden, T., Radmilovic, V., Ramasse, Q., Watanabe, M., Erni, R., Stach, E., Denes, P., and Dahmen, U. (2008). Detection of Single Atoms and Buried Defects in Three Dimensions by Aberration-Corrected Electron Microscope with 0.5-Å Information Limit. *Microscopy and Microanalysis*, 14(5):469–477. (Cited on page 1.)

[51] Klar, T. A., Jakobs, S., Dyba, M., Egner, A., and Hell, S. W. (2000). Fluorescence microscopy with diffraction resolution barrier broken by stimulated emission. *Proceedings of the National Academy of Sciences*, 97(15):8206–8210. (Cited on page 1.)

[52] Klein, S. and Staring, M. (2015). *elastix - the manual*. (Cited on page 50.)

[53] Klein, S., Staring, M., Murphy, K., Viergever, M. A., and Pluim, J. P. (2010). elastix: a toolbox for intensity-based medical image registration. *IEEE Transactions on Medical Imaging*, 29(1):196 – 205. (Cited on page 42.)

[54] Kramers, H. (1927). La diffusion de la lumière par les atomes. *Atti del Congresso Internationale dei Fisici*, Como, 2:545–557. (Cited on page 16.)

[55] Kuo, F. and Kaiser, J. (1966). *System analysis by digital computer*. Wiley. (Cited on page 44.)

[56] Lachance, G. and Claisse, F. (1995). *Quantitative X-ray fluorescence analysis: theory and application*. Wiley. (Cited on page 55.)

[57] Lee, P. A., Citrin, P. H., Eisenberger, P., and Kincaid, B. M. (1981). Extended x-ray absorption fine structure – its strengths and limitations as a structural tool. *Rev. Mod. Phys.*, 53:769–806. (Cited on page 1.)

[58] Lengeler, B., Schroer, C., Tümmler, J., Benner, B., Richwin, M., Snigirev, A., Snigireva, I., and Drakopoulos, M. (1999a). Imaging by parabolic refractive lenses in the hard x-ray range. *J. Synchrotron Rad.*, 6:1153–1167. (Cited on page 53.)

[59] Lengeler, B., Schroer, C. G., Kuhlmann, M., Benner, B., Günzler, T. F., Kurapova, O., Zontone, F., Snigirev, A., and Snigireva, I. (2005). Refractive x-ray lenses. *J. Phys. D: Appl. Phys.*, 38:A218–A222. (Cited on page 53.)

[60] Lengeler, B., Schroer, C. G., Richwin, M., Tümmler, J., Drakopoulos, M., Snigirev, A., and Snigireva, I. (1999b). A microscope for hard x-rays based on parabolic compound refractive lenses. *Appl. Phys. Lett.*, 74(26):3924–3926. Times cited: 213. (Cited on page 53.)

[61] Lester, H. and Arridge, S. R. (1999). A survey of hierarchical non-linear medical image registration. *Pattern Recognition*, 32(1):129 – 149. (Cited on page 42.)

[62] López-Gándara, C., Ramos, F. M., and Cirera, A. (2009). YSZ-Based Oxygen Sensors and the Use of Nanomaterials: A Review from Classical Models to Current Trends. *Journal of Sensors*, 2009:15. (Cited on page 79.)

[63] Lowekamp, B., gabehart, Blezek, D., Ibanez, L., McCormick, M., Chen, D., Mueller, D., Cole, D., Johnson, H., Marstal, K., Beare, R., Gelas, A., Williams, K., Doria, D., and King, B. (2015). Simpleelastix: Simpleelastix v0.9.0. (Cited on page 42.)

[64] Maiden, A. M., Humphry, M. J., Sarahan, M. C., Kraus, B., and Rodenburg, J. M. (2012). An annealing algorithm to correct positioning errors in ptychography. *Ultramicroscopy*, 120:64–72. (Cited on pages 3 and 37.)

[65] Maiden, A. M. and Rodenburg, J. M. (2009). An improved ptychographical phase retrieval algorithm for diffractive imaging. *Ultramicroscopy*, 109(10):1256–1262. (Cited on pages 32, 33 and 80.)

[66] Maintz, J. and Viergever, M. A. (1998). A survey of medical image registration. *Medical Image Analysis*, 2(1):1 – 36. (Cited on page 42.)

[67] Marstal, K. (2015). SimpleElastix. https://simpleelastix.readthedocs.io/index.html. (Cited on pages 42 and 85.)

[68] Marstal, K., Berendsen, F., Staring, M., and Klein, S. (2016). SimpleElastix: A user-friendly, multi-lingual library for medical image registration. International Workshop on Biomedical Image Registration (WBIR), Las Vegas, Nevada, USA. (Cited on page 42.)

[69] Miao, J., Charalambous, P., Kirz, J., and Sayre, D. (1999). Extending the methodology of X-ray crystallography to allow imaging of micrometre-sized non-crystalline specimens. *Nature*, 400:342–344. (Cited on page 1.)

[70] Mimura, H., Handa, S., Kimura, T., Yumoto, H., Yamakawa, D., Yokoyama, H., Matsuyama, S., Inagaki, K., Yamamura, K., Sano, Y., Tamasaku, K., Nishino, Y., Yabashi, M., Ishikawa, T., and Yamauchi, K. (2010). Breaking the $10\ \mathrm{nm}$ barrier in hard-X-ray focusing. *Nature Physics*, 6:122–125. (Cited on page 1.)

[71] Nandi, S. (2002). *Magnetic X-Ray Scattering*. John Wiley & Sons, Inc. (Cited on page 5.)

[72] Nashed, Y. S. G., Vine, D. J., Peterka, T., Deng, J., Ross, R., and Jacobsen, C. (2014). Parallel ptychographic reconstruction. *Opt. Express*, 22(26):32082–32097. (Cited on page 33.)

[73] NTT Advanced Technology Corporation (Accessed November 4, 2016). X-ray chart. http://www.ntt-at.com/product/x-ray_chart/. (Cited on page 61.)

[74] Optique Peter (Accessed December 11, 2016). X-ray imaging microscopes. http://www.optiquepeter.com/. (Cited on page 53.)

[75] PCO (Accessed December 11, 2016). pco.4000 camera. https://www.pco.de/sensitive-cameras/pco4000/. (Cited on page 54.)

[76] Ramamoorthy, R., Dutta, P. K., and Akbar, S. A. (2003). Oxygen sensors: Materials, methods, designs and applications. *Journal of Materials Science*, 38(21):4271–4282. (Cited on page 79.)

[77] Reinhardt, J., Hoppe, R., Hofmann, G., Damsgaard, C. D., Patommel, J., Baumbach, C., Baier, S., Rochet, A., Grunwaldt, J.-D., Falkenberg, G., and Schroer, C. G. (2017). Beamstop-based low-background ptychography to image weakly scattering objects. *Ultramicroscopy*, 173:52 – 57. (Cited on pages 3, 45, 76 and 120.)

[78] Ruffoni, M., Pettifer, R., Pascarelli, S., Trapananti, A., and Mathon, O. (2007). Probing atomic displacements with thermal differential EXAFS. *Journal of synchrotron radiation*, 14(Pt 5):421– 425. (Cited on page 40.)

[79] Sakdinawat, A. and Attwood, D. (2010). Nanoscale x-ray imaging. *Nat Photon*, 4(12):840–848. (Cited on page 39.)

[80] Schneider, C. A., Rasband, W. S., and Eliceiri, K. W. (2012). NIH Image to ImageJ: 25 years of image analysis. *Nat Meth*, 9(7):671–675. (Cited on page 42.)

[81] Schroer, C. (2017). Coherent x-ray nano imaging despite locally incoherent illumination. in preparation. (Cited on pages 38 and 120.)

[82] Schroer, C., Baumbach, C., Döhrmann, R., Klare, S., Hoppe, R., Kahnt, M., Patommel, J., Reinhardt, J., Ritter, S., Samberg, D., Scholz, M., Schropp, A., Seiboth, F., Seyrich, M., Wittwer, F., and Falkenberg, G. (2016). Hard x-ray nanoprobe of beamline P06 at PETRA III. *Proceeding of the 12th International Conference on Synchrotron Radiation Instrumentation*. (Cited on page 51.)

[83] Schroer, C. G., Lengeler, B., Benner, B., Günzler, T. F., Kuhlmann, M., Simionovici, A. S., Bohic, S., Drakopoulos, M., Snigirev, A., Snigireva, I., and Schröder, W. H. (2001). Microbeam production using compound refractive lenses: beam characterization and applications. In McNulty, I., editor, *X-Ray Micro- and Nano-Focusing: Applications and Techniques II*, volume 4499 of *Proceedings of the SPIE*, pages 52–63, Bellingham, WA. SPIE. (Cited on page 53.)

[84] Schropp, A., Hoppe, R., Patommel, J., Samberg, D., Seiboth, F., Stephan, S., Wellenreuther, G., Falkenberg, G., and Schroer, C. G. (2012). Hard x-ray scanning microscopy with coherent radiation: Beyond the resolution of conventional x-ray microscopes. *Appl. Phys. Lett.*, 100:253112. (Cited on page 2.)

[85] Schropp, A. and Schroer, C. G. (2010). Dose requirements for resolving a given feature in an object by coherent x-ray diffraction imaging. *New J. Phys.*, 12:035016. (Cited on page 2.)

[86] Scipy.org – SciPy v0.18.1 Reference Guide (Accessed January 16, 2017). scipy.optimize.least_squares. https://docs.scipy.org/doc/scipy-0.18.1/reference/generated/scipy.optimize.least_squares.html. (Cited on page 89.)

[87] Seiboth, F., Schropp, A., Hoppe, R., Meier, V., Patommel, J., Lee, H. J., Nagler, B., Galtier, E. C., Arnold, B., Zastrau, U., Hastings, J. B., Nilsson, D., Uhlén, F., Vogt, U., Hertz, H. M., and Schroer, C. G. (2014). Focusing XFEL SASE pulses by rotationally parabolic refractive x-ray lenses. *J. Phys. Conf. Ser.*, 499:012004. (Cited on page 53.)

[88] Shamonin, D. P., Bron, E. E., Lelieveldt, B. P., Smits, M., Klein, S., and Staring, M. (2014). Fast Parallel Image Registration on CPU and GPU for Diagnostic Classification of Alzheimer's Disease. *Frontiers in Neuroinformatics*, 7(50):1–15. (Cited on page 42.)

[89] Shapiro, D. A., Yu, Y.-S., Tyliszczak, T., Cabana, J., Celestre, R., Chao, W., Kaznatcheev, K., David, K. L., Maia, F., Marchesini, S., Meng, Y. S., Warwick, T., Yang, L. L., and Padmore, H. A. (2014). Chemical composition mapping with nanometre resolution by soft x-ray microscopy. *Nat Photon*, 8(10):765–769. (Cited on page 2.)

[90] Smith, S. W. (1997). *The Scientist and Engineer's Guide to Digital Signal Processing*. California Technical Publishing, San Diego, CA, USA. (Cited on page 43.)

[91] Snigirev, A., Kohn, V., Snigireva, I., and Lengeler, B. (1996). A compound refractive lens for focusing high energy x-rays. *Nature (London)*, 384:49. (Cited on page 1.)

[92] Stöhr, J. (1992). *NEXAFS Spectroscopy*. Springer Series in Surface Sciences. Springer. (Cited on page 39.)

[93] Suzuki, A., Furutaku, S., Shimomura, K., Yamauchi, K., Kohmura, Y., Ishikawa, T., and Takahashi, Y. (2014). High-resolution multislice x-ray ptychography of extended thick objects. *Phys. Rev. Lett.*, 112(5):053903. (Cited on page 37.)

[94] Takayama, Y. and Yonekura, K. (2016). Cryogenic coherent X-ray diffraction imaging of biological samples at SACLA: a correlative approach with cryo-electron and light microscopy. *Acta Crystallographica Section A*, 72(2):179–189. (Cited on page 2.)

[95] Tektronix (Accessed January 31, 2017). Keithley. http://www.tek.com/keithley-low-level-sensitive-and-specialty-instruments/keithley-series-6400-picoammeters. (Cited on page 55.)

[96] Thevenaz, P., Ruttimann, U. E., and Unser, M. (1998). A pyramid approach to subpixel registration based on intensity. *IEEE Transactions on Image Processing*, 7(1):27–41. (Cited on page 42.)

[97] Thibault, P., Dierolf, M., Bunk, O., Menzel, A., and Pfeiffer, F. (2009). Probe retrieval in ptychographic coherent diffractive imaging. *Ultramicroscopy*, 109(4):338–343. (Cited on page 32.)

[98] Thibault, P., Dierolf, M., Menzel, A., Bunk, O., David, C., and Pfeiffer, F. (2008). High-resolution scanning x-ray diffraction microscopy. *Science*, 321(5887):379–382. (Cited on page 2.)

[99] Thibault, P. and Menzel, A. (2013). Reconstructing state mixtures from diffraction measurements. *Nature (London)*, 494:68–71. (Cited on pages 37 and 38.)

[100] Thomas, J. M. and Hernandez-Garrido, J.-C. (2009). Probing solid catalysts under operating conditions: Electrons or x-rays? *Angew. Chem. Int. Ed.*, 48(22):3904–3907. (Cited on page 1.)

[101] Träger, F. (2012). *Springer Handbook of Lasers and Optics*. Springer Handbooks. Springer Berlin Heidelberg. (Cited on page 53.)

[102] van Heel, M. and Schatz, M. (2005). Fourier shell correlation threshold criteria. *Journal of Structural Biology*, 151(3):250 – 262. (Cited on pages 44 and 75.)

[103] Volkov, S., Vonk, V., Khorshidi, N., Franz, D., Kubicek, M., Kilic, V., Felici, R., Huber, T. M., Navickas, E., Rupp, G. M., Fleig, J., and Stierle, A. (2016). Operando x-ray investigation of electrode/electrolyte interfaces in model solid oxide fuel cells. *Chemistry of Materials*, 28(11):3727–3733. (Cited on page 79.)

[104] Vonk, V., Khorshidi, N., Stierle, A., and Dosch, H. (2013). Atomic structure and composition of the yttria-stabilized zirconia (111) surface. *Surface Science*, 612:69–76. (Cited on page 79.)

[105] Warwick, T., Franck, K., Kortright, J. B., Meigs, G., Moronne, M., Myneni, S., Rotenberg, E., Seal, S., Steele, W. F., Ade, H., Garcia, A., Cerasari, S., Denlinger, J., Hayakawa, S., Hitchcock, A. P., Tyliszczak, T., Kikuma, J., Rightor, E. G., Shin, H.-J., and Tonner, B. P. (1998). A scanning transmission x-ray microscope for materials science spectromicroscopy at the advanced light source. *Review of Scientific Instruments*, 69(8):2964–2973. (Cited on page 39.)

[106] Watts, B. (2014). Calculation of the Kramers-Kronig transform of X-ray spectra by a piecewise Laurent polynomial method. *Opt. Express*, 22(19):23628–23639. (Cited on page 41.)

[107] Wiedemann, H. (2003). *Synchrotron Radiation*. Advanced Texts in Physics. Springer. (Cited on page 51.)

[108] Yoshida, H., Kuwauchi, Y., Jinschek, J. R., Sun, K., Tanaka, S., Kohyama, M., Shimada, S., Haruta, M., and Takeda, S. (2012). Visualizing gas molecules interacting with supported nanoparticulate catalysts at reaction conditions. *Science*, 335(6066):317–319. (Cited on page 1.)

[109] Zhang, F., Peterson, I., Vila-Comamala, J., Diaz, A., Berenguer, F., Bean, R., Chen, B., Menzel, A., Robinson, I. K., and Rodenburg, J. M. (2013). Translation position determination in ptychographic coherent diffraction imaging. *Opt. Express*, 21(11):13592–13606. (Cited on page 3.)

[110] Zitová, B. and Flusser, J. (2003). Image registration methods: a survey. *Image and Vision Computing*, 21(11):977 – 1000. (Cited on page 42.)

List of Publications

- J. Reinhardt, R. Hoppe, G. Hofmann, C. D. Damsgaard, J. Patommel, C. Baumbach, J.-D. Grunwaldt, G. Falkenberg, and C. G. Schroer. *Beamstop-Based Low-Background Ptychography to Image Weakly Scattering Objects.* Ultramicroscopy, 173: 52-57, February 2017
- S. Baier, C. D. Damsgaard, M. Klumpp, Z. Balogh, J. Reinhardt, T. Kasama, T. Sheppard, F. Benzi, J. B. Wagner, W. Schwieger, C. G. Schroer, and J.-D. Grunwaldt. *Stability of a bifunctional Cu-based core@zeolite shell catalyst for DME synthesis under redox conditions studied by ETEM and in situ ptychography.* Microscopy and Microanalysis, 23(3): 501-512, 2017
- C. Schroer, C. Baumbach, R. Döhrmann, S. Klare, R. Hoppe, M. Kahnt, J. Patommel, J. Reinhardt, S. Ritter, D. Samberg, M. Scholz, A. Schropp, F. Seiboth, M. Seyrich, F. Wittwer, and G. Falkenberg. *Hard x-ray nanoprobe of beamline P06 at PETRA III.* Proceedings of the 12th International Conference on Synchrotron Radiation Instrumentation, January 2016
- S. Baier, A. Wittstock, C. D. Damsgaard, A. Diaz, J. Reinhardt, F. Benzi, J. Shi, T. Scherer, D. Wang, C. Kübel, C. G. Schroer, and J.-D. Grunwaldt. *Influence of gas atmosphere and ceria on the stability of nanoporous gold studied by environmental electron microscopy and in situ ptychography.* RSC Advances, 6: 83031-83043, 2016
- C. Y.J. Hémennot, J. Reinhardt, O. Saldahna, J. Patommel, R. Graceffa, B. Weinhausen, M. Burgahammer, Schroer C. G, and S. Koester. *X-rays reveal the interal structure of keratin bundles in whole cells.* ACS Nano, 10(3): 3553-3561, February 2016
- T. Stankevic, D. Dzhigaev, Z. Bi, M. Rose, A. Shabalin, J. Reinhardt, A. Mikkelsen, L. Samuelson, G. Falkenberg, I. A. Vartanyants, and R. Feidenhans'l. *Nanofocused x-ray beams applied for mapping strain in core-shell nanowires.* volume 9592 of Proc. SPIE, pages 95920D-95920D-7, 2015
- T. Stankevic, D. Dzhigaev, Z. Bi, M. Rose, A. Shabalin, J. Reinhardt, A. Mikkelsen, L. Samuelson, G. Falkenberg, I. A. Vartanyants, and R. Feidenhans'l. *Strain mapping in an InGaN/GaN nanowire using a nano-focused x-ray beam.* Applied Physics Letters, 107(10), 2015
- H. F. Dam, T. R. Andersen, E. B. L. Pedersen, K. T. S. Thydén, M. Helgesen, J. C. Carlé, P. S. Jørgensen, J. Reinhardt, R. R. Søndergaard, M. Jørgensen, E. Bundgaard, F. C. Krebs, and J. W. Andreasen. Enabling Flexible *Polymer Tandem Solar Cells by 3D Ptychographic Imaging.* Advanced Energy Materials, 1400736, 2014

- F. Seiboth, M. Scholz, J. Patommel, R. Hoppe, F. Wittwer, J. Reinhardt, J. Seidel, M. Knaut, A. Jahn, K. Richter, J. W. Bartha, G. Falkenberg, and C. G. Schroer. *Hard x-ray nanofocusing by refractive lenses of constant thickness.* Appl. Phys. Lett., 105(13):131110, 2014

- R. Hoppe, J. Reinhardt, G. Hofmann, J. Patommel, J.-D. Grunwaldt, C. D. Damsgaard, G. Wellenreuther, G. Falkenberg, and C. G. Schroer. *High-Resolution Chemical Imaging of Gold Nanoparticles Using Hard X-Ray Ptychography.* Appl. Phys. Lett., 102(20):203104, 2013

- C. G. Schroer, F.-E. Brack, R. Brendler, S. Hönig, R. Hoppe, J. Patommel, S. Ritter, M. Scholz, A. Schropp, F. Seiboth, D. Nilsson, J. Rahomäki, F. Uhlén, U. Vogt, J. Reinhardt, and G. Falkenberg. *Hard x-ray nanofocusing with refractive x-ray optics: full beam characterization by ptychographic imaging.* Proc. SPIE, 8848:884807, 2013

Appendix A

Parameter map "affine"

```
(AutomaticParameterEstimation "true")
(CheckNumberOfSamples "true")
(DefaultPixelValue 0)
(FinalBSplineInterpolationOrder 3)
(FixedImagePyramid "FixedSmoothingImagePyramid")
(ImageSampler "RandomCoordinate")
(Interpolator "LinearInterpolator")
(MaximumNumberOfIterations 256)
(MaximumNumberOfSamplingAttempts 8)
(Metric "AdvancedMattesMutualInformation")
(MovingImagePyramid "MovingSmoothingImagePyramid")
(NewSamplesEveryIteration "true")
(NumberOfResolutions 4)
(NumberOfSamplesForExactGradient 4096)
(NumberOfSpatialSamples 2048)
(Optimizer "AdaptiveStochasticGradientDescent")
(Registration "MultiResolutionRegistration")
(ResampleInterpolator "FinalBSplineInterpolator")
(Resampler "DefaultResampler")
(ResultImageFormat "nii")
(Transform "AffineTransform")
(WriteResultImage "true")
```

Parameter map "bspline"

```
(AutomaticParameterEstimation "true")
(CheckNumberOfSamples "true")
(DefaultPixelValue 0)
(FinalBSplineInterpolationOrder 3)
(FinalGridSpacingInPhysicalUnits 8)
(FixedImagePyramid "FixedSmoothingImagePyramid")
(GridSpacingSchedule 2.80322 1.9881 1.41 1)
(ImageSampler "RandomCoordinate")
(Interpolator "LinearInterpolator")
(MaximumNumberOfIterations 512)
(MaximumNumberOfSamplingAttempts 8)
(Metric "AdvancedMattesMutualInformation" "TransformBendingEnergyPenalty")
(Metric0Weight 1)
(Metric1Weight 10000)
(MovingImagePyramid "MovingSmoothingImagePyramid")
(NewSamplesEveryIteration "true")
(NumberOfResolutions 4)
```

```
(NumberOfSamplesForExactGradient 4096)
(NumberOfSpatialSamples 3000)
(Optimizer "AdaptiveStochasticGradientDescent")
(Registration "MultiMetricMultiResolutionRegistration")
(ResampleInterpolator "FinalBSplineInterpolator")
(Resampler "DefaultResampler")
(ResultImageFormat "nii")
(Transform "BSplineTransform")
(WriteResultImage "true")
```

Appendix B

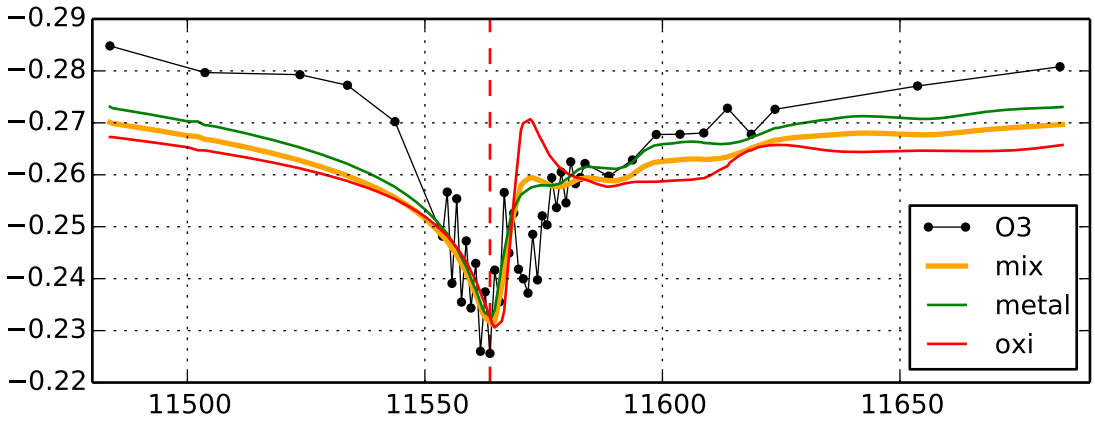

(a) all scan points

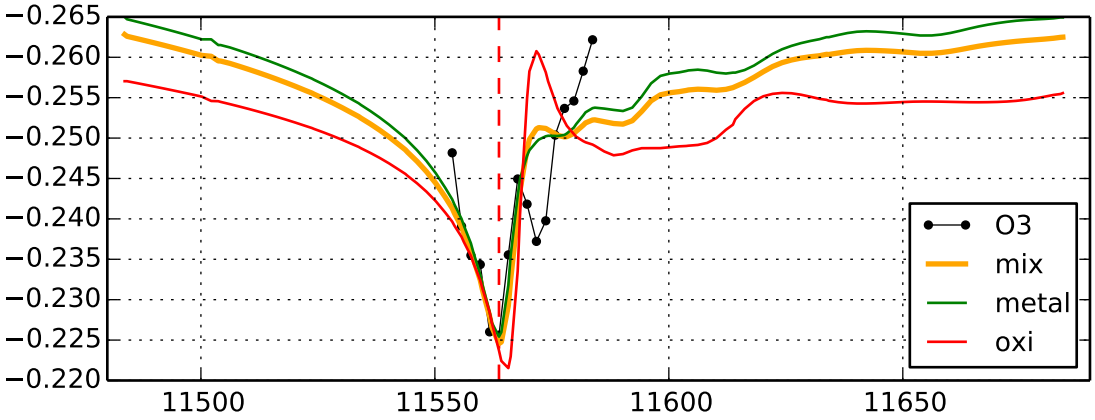

(b) first scan set

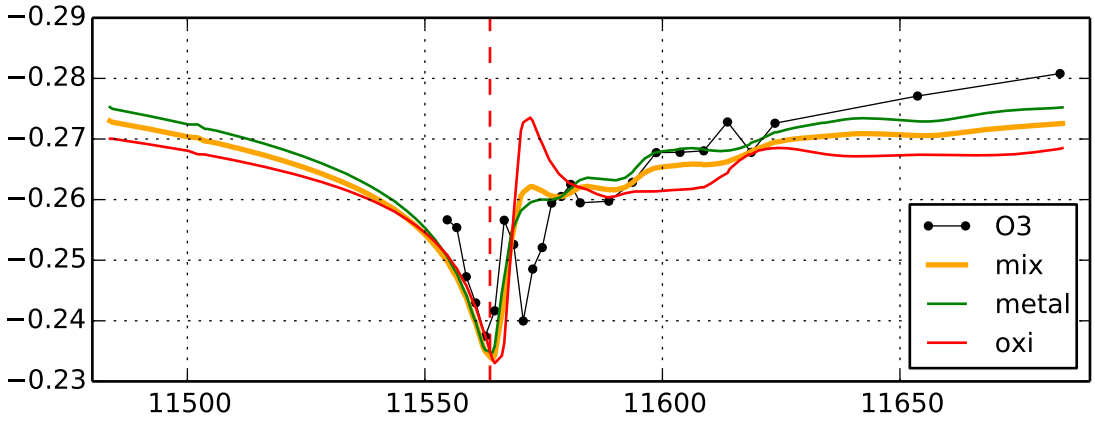

(c) second scan set

Fit for the ROI *O3*

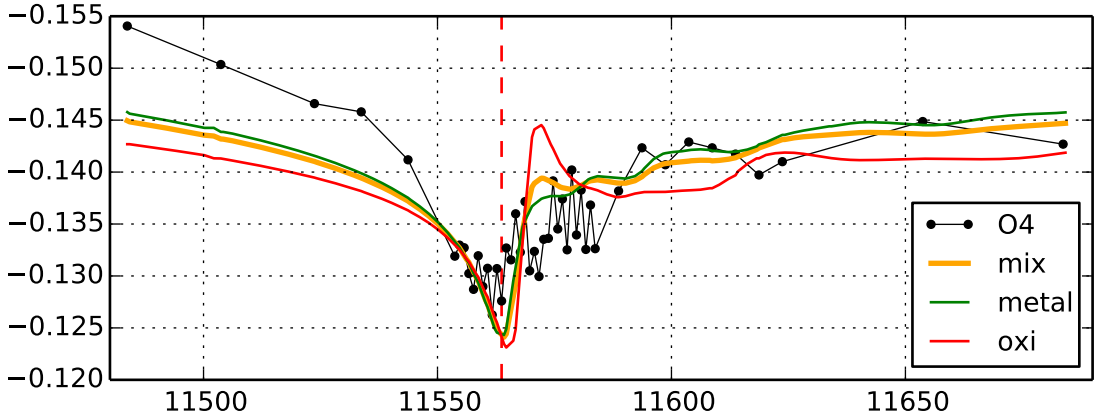

(a) all scan points

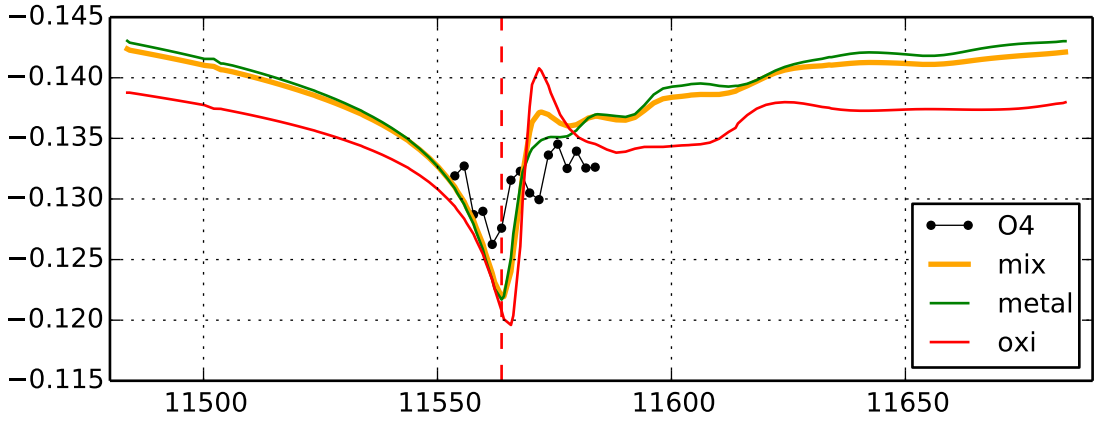

(b) first scan set

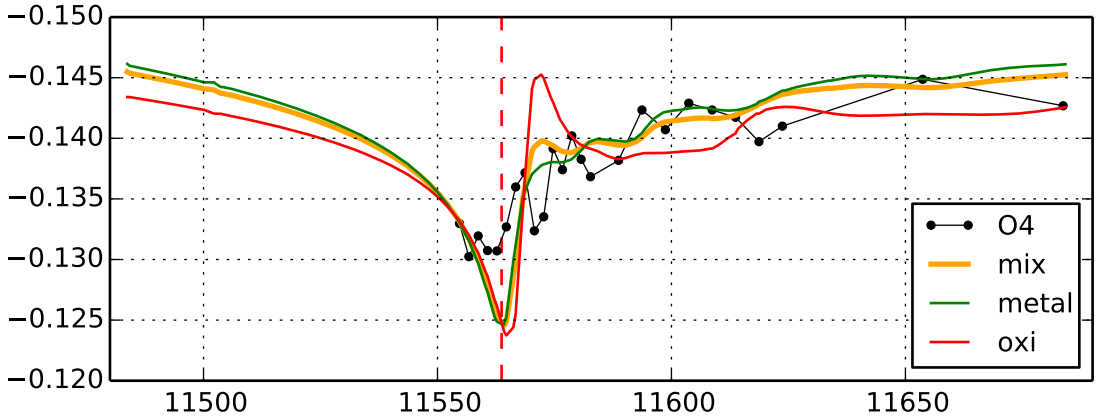

(c) second scan set

Fit for the ROI *O4*

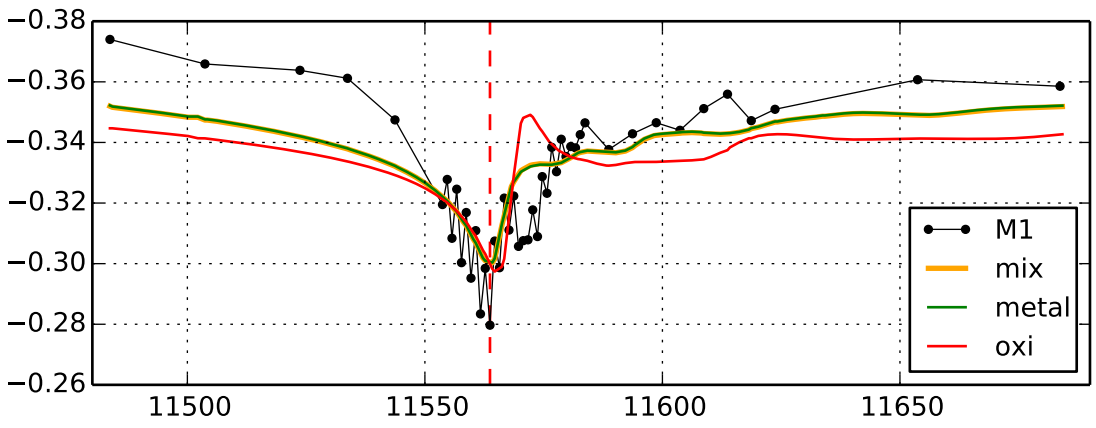

(a) all scan points

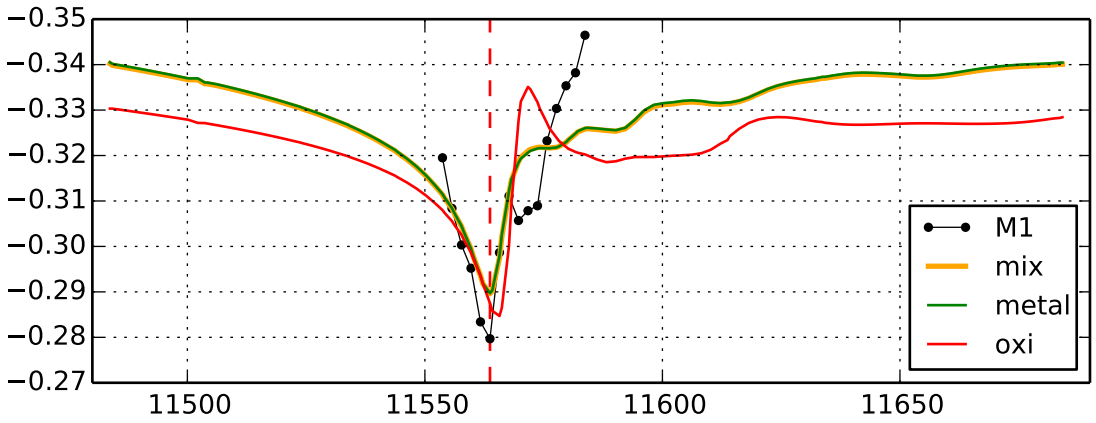

(b) first scan set

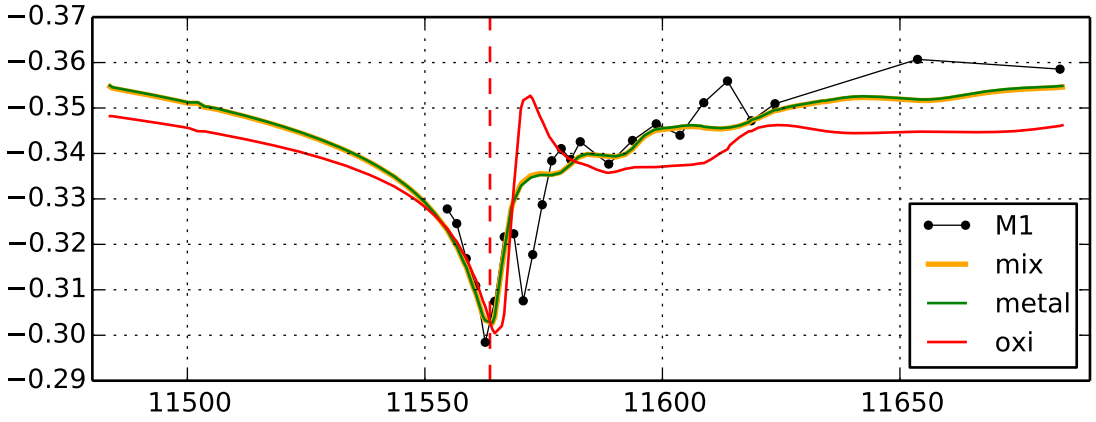

(c) second scan set

Fit for the ROI *M1*

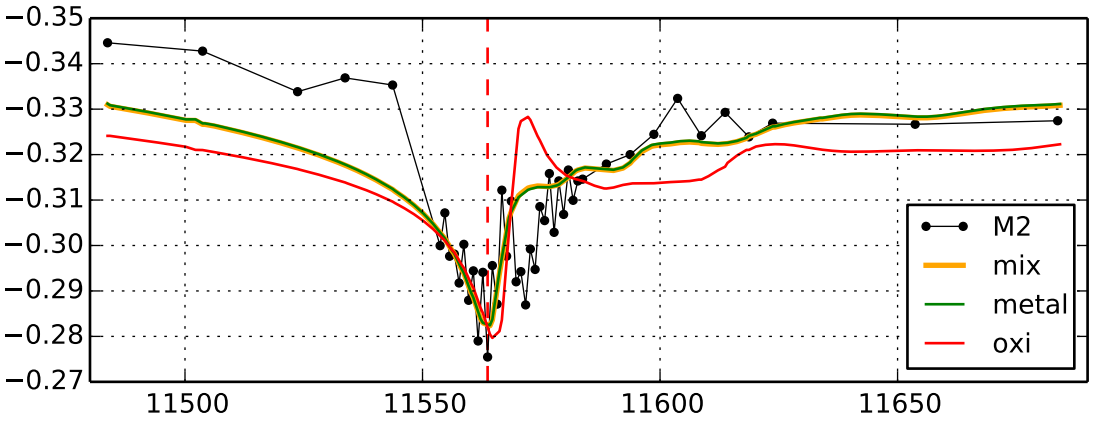

(a) all scan points

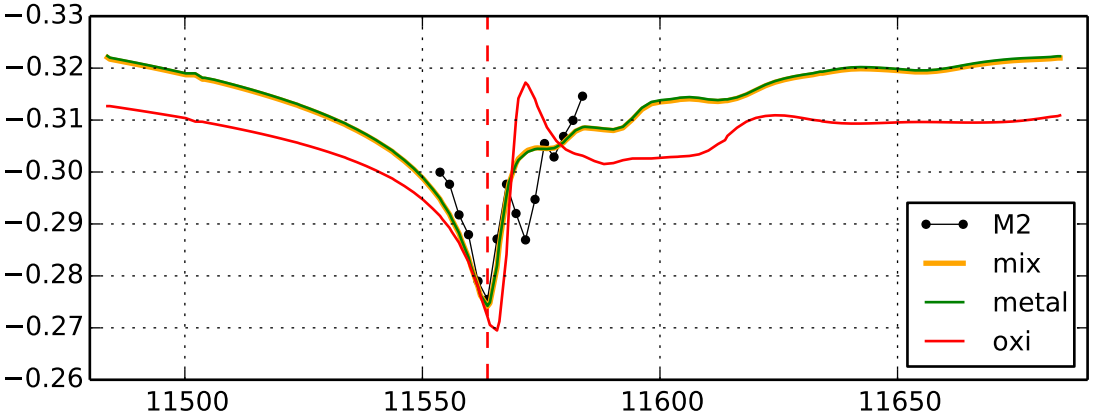

(b) first scan set

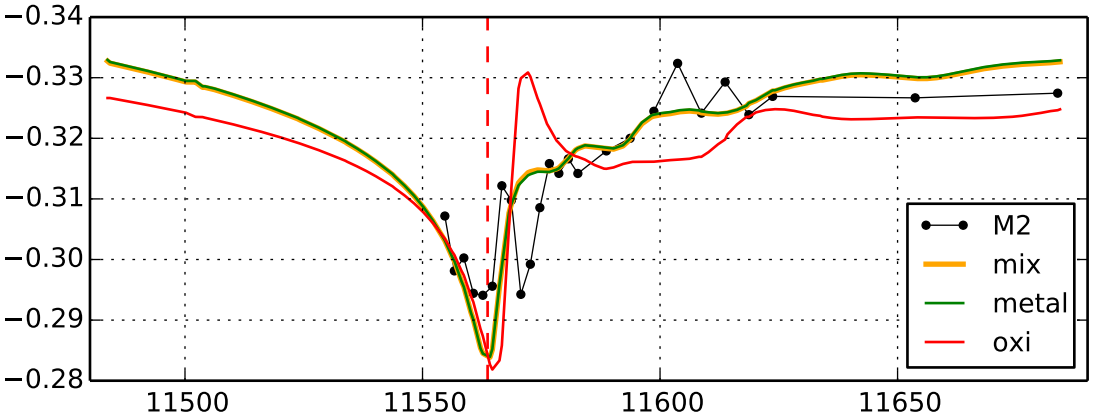

(c) second scan set

Fit for the ROI *M2*

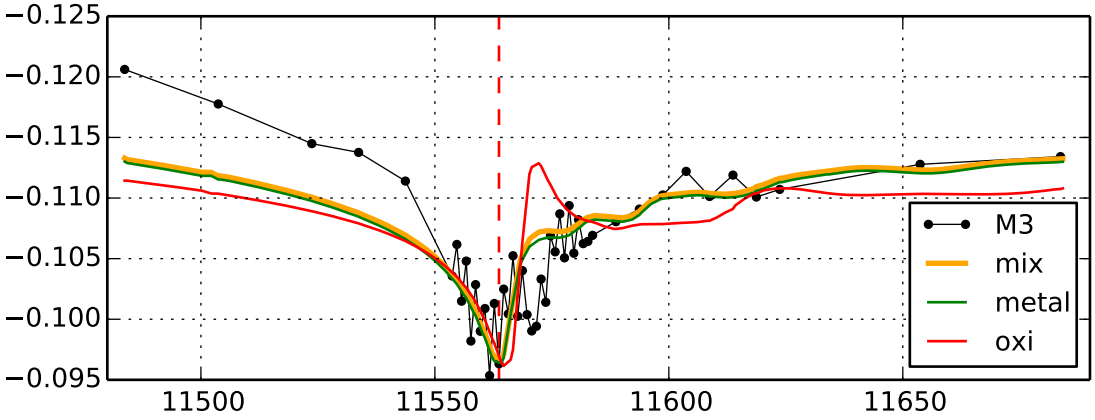

(a) all scan points

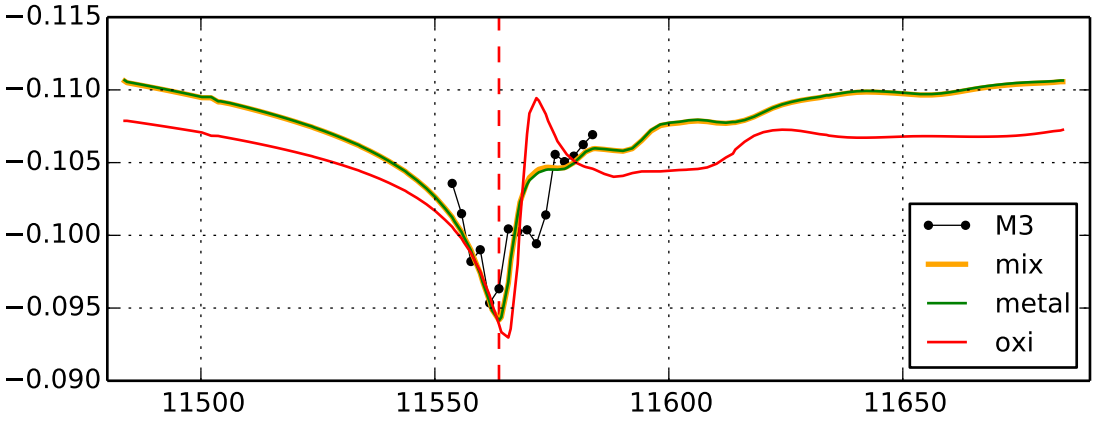

(b) first scan set

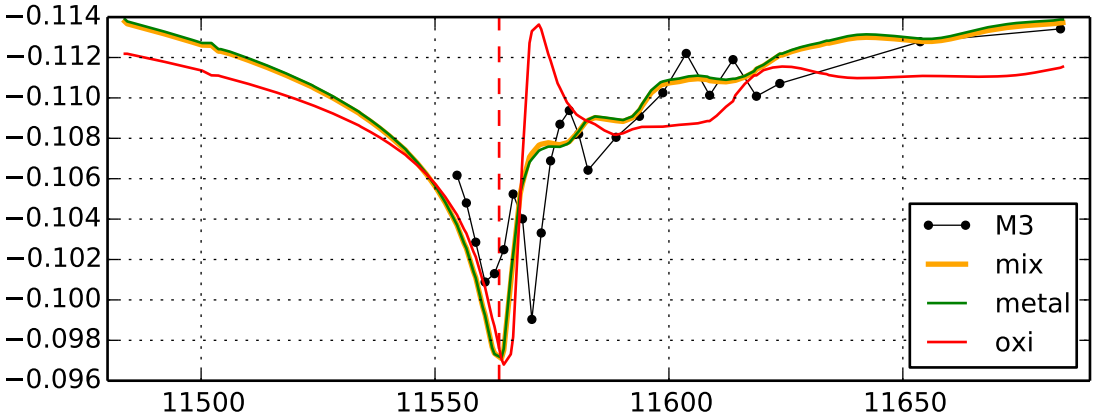

(c) second scan set

Fit for the ROI *M3*

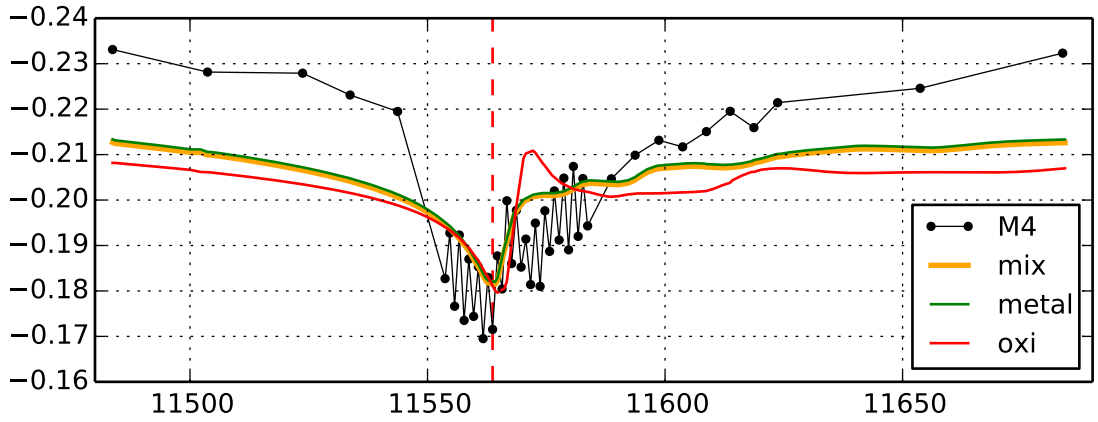

(a) all scan points

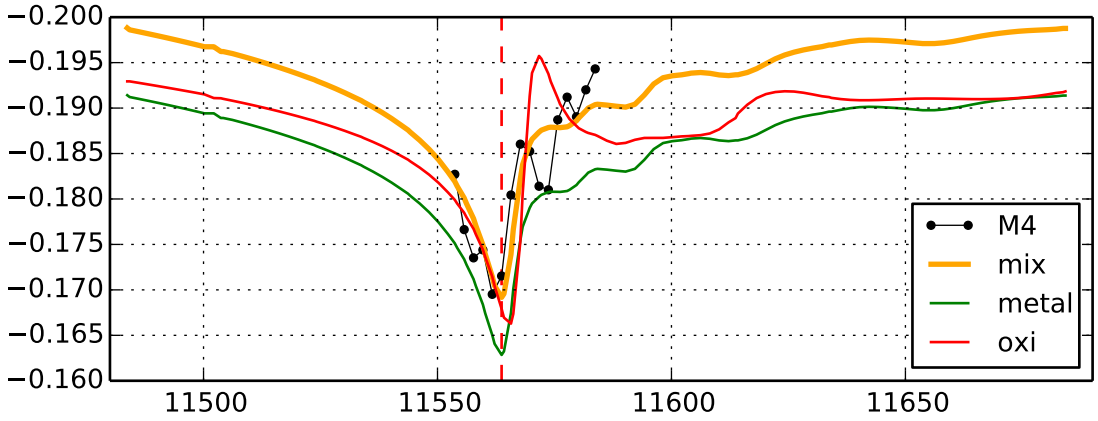

(b) first scan set

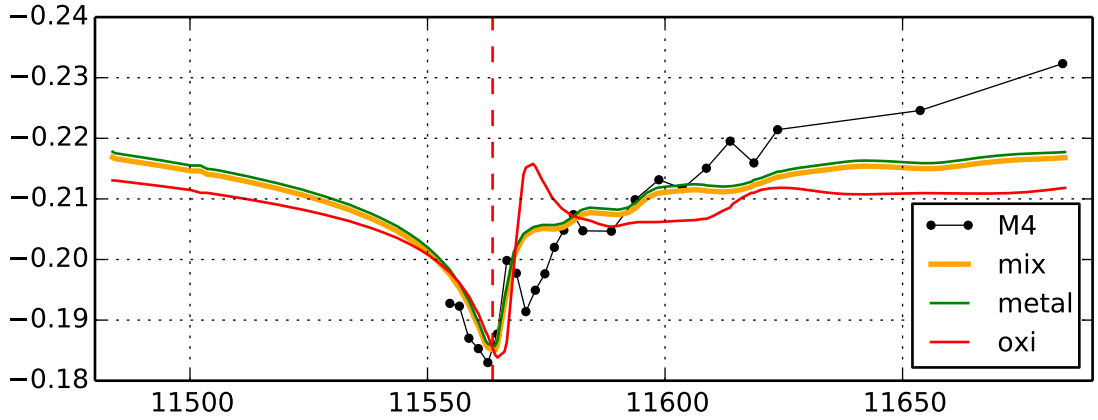

(c) second scan set

Fit for the ROI *M4*

Danksagung – Acknowledgement

Während der vergangenen vier Jahre kreuzten viele interessante Menschen meinen Weg und begleiteten diesen zum Teil mehrere Jahre. Etliche von Ihnen trugen zum Gelingen dieser Arbeit bei und sorgten für eine wunderbare Zeit.

Zunächst bedanke ich mich bei meinem Doktorvater Prof. Dr. Christian G. Schroer, dessen froehliche und positive Art mich stets neu zu motivieren vermochte. Christians fachliche Kompetenz in Kombination mit seinem Enthusiasmus dient als Vorbild und trotz eines vollen Terminkalenders fand er stets Zeit für Diskussion über die Herausforderungen der Arbeit.

Meinem zweiten Gutachter, Prof. Dr. Andreas Stierle, danke ich nicht nur für die Übernahme des Zweitgutachtens, sondern auch für die neuen und spannenden Einblicke in die Nanowissenschaften fernab der Ptychographie. Vom DESY NanoLab danke ich insbesondere auch Thomas Keller für die Bereitstellung der Elektronenmikrsokopieaufnahmen sowie die für fachliche Unterstützung bei Fragen zur spezifischen Anwendung der Proben.

Bereits seit meiner Diplomarbeit besteht ein reger Austausch mit der Arbeitsgruppe von Jan-Dierk Grunwaldt vom Institut für Technische Chemie und Polymerchemie des KIT, Karlsruhe. Ich danke Jan-Dierk Grunwaldt und Sina Baier für die ausdauernde Zusammenarbeit um der Ptychographie ein Anwendungsgebiet der chemischen Bildgebung bei der Erforschung von Katalysatoren zu geben. Ein ganz besonderer Dank geht an Georg Hofmann für die unermüdliche Unterstützung bei der Probenpräparation sowie bei Planung und Durchführung von Messzeiten und anschliessender Auswertung. Bezüglich der Probenpräparation bedanke ich mich ebenfalls bei Christan Damsgaard von der DTU, Copenhagen. Thank you Christian for your time and effort at the electron microscope and your ideas for tackling difficult data evaluation.

Zu Beginn meiner Doktorarbeit gehörte ich direkt dem Team der Beamline P06 an. In dieser Zeit habe ich mehr denn je gelernt, was es heisst am Experiment zu arbeiten, dieses zu warten und einzurichten und andere Forschungsgruppen zu unterstützen. Ich danke Gerald Falkenberg für das entgegengesetzte Vertrauen und die kritischen Diskussionen, zu meiner Arbeit, über die Funktionsweise verschiedener Komponenten und vielem mehr. Allen anderen (ehemaligen) Mitgliedern der Beamline, Preety Bhargava, Thorsten Claussen, Martin Doering, Matthias Alfeld, Philipp Alraun und Kathryn Spiers danke ich für die Unterstützung bei Planung und Durchführung von Messzeiten und Auswertung. Ulrike Boesenberg danke ich für ihren ausdauernden Einsatz und die Weitergabe ihrer langjährigen Erfahrung, welche mir insbesondere in der Anfangszeit sehr geholfen hat. Gerade die letzten Experimente wären ohne die großartige Unterstützung von Jan Garrevoet nicht durchführbar gewesen. Thank you so very much, Jan.

Weiterhin danke ich Florian Meirer und Sam Kalirai für spannende Messzeiten an echten Proben.

Die Verbindung zur Dresdner Arbeitsgruppe aus Diplomarbeitszeiten brach auch während meiner Tätigkeit am DESY nicht ab und ich danke etlichen (ehemaligen) Mitgliedern dieser Arbeitsgruppe für die gute Zusammenarbeit zwischen Dresden und Hamburg und die Unterstützung bei Messzeiten. Vielen Dank an Susanne Klare, Florian Brack, Jacob Seifert und allen anderen Master- und Bachelorstudenten. Ein spezieller Dank richtet sich an Jens Patommel für die Unterstützung in Softwarefragen rund um *ACcontrol* und *tomo*, sowie an Robert Hoppe und Christoph Baumbach für die lehrreiche Zeit in Bezug auf das Programmieren von PtychoCode. Stephan Ritter danke sehr ich für seine Hilfsbereitschaft, die ihn sogar spontan in einen Zug von Dresden nach Hamburg steigen lässt!

Meinen Kollegen der stetig wachsenden Arbeitsgruppe FS-PETRA, Andreas Schropp, Mikhail Lyubomirskiy, Martin Seyrich, Maik Kahnt, Frank Seiboth, Dennis Brückner, Valerija Music, Lukas Grothe, Felix Wittwer und Maria Scholz danke ich für eine wunderbare Atmosphäre mit aufreibenden Diskussion, durchgemachten Nächten an der Beamline, gelegentlichen Kickerspielen und vielen weiteren witzigen Aktivitäten inner- und auch außerhalb des DESY Campus. Maria, Felix, Martin und Andreas gilt mein besonderer Dank für das gründliche Korrekturlesen meiner Dissertation. Außerdem ist Maria die beste Bürokollegin, die ich mir vorstellen kann.

Keines der Experimente hätte ohne die herroragende Arbeit unserer Ingenieure funktioniert. Tatkräftige Unterstützung leisteten erst Dirk Samberg aus Dresden und anschließend auch Ralph Döhrmann, Stefan Botta und Hendrik Lindemann mit kreativen Ideen und stimmiger Umsetzung, oft auch auf den letzen Drücker. Vielen Dank, auch an die fleißigen Arbeiter der DESY Werkstatt. An einer so komplexen Arbeitsstelle wie einer Beamline, jedoch auch am eigenen Büro-PC ist der Soft- und Hardware Support nicht zu unterschätzen. Ich bedanke mich beim gesamten FS-EC Team für alle Hilfe bei Server, Soft- und Hardwareproblemen. Insbesondere André Rothkirch hatte immer ein offenes Ohr und eine zeitnahe Lösung bei allen Problemen und trug somit erheblich zu einem angehnemen Arbeitsablauf bei. Auch Markus Fleck war stets zur Stelle, wenn ich mal wieder diverse Teile meines PCs in die Knie gezwungen hatte oder Upgrades einforderte. Ich danke Euch!

Zwischen all dem wissenschaftlichen Austausch am DESY findet man auch Freunde für die Zeit darüberhinaus. Ich danke Andrey Saveliev, Thomas Gaumnitz und Marie Rehders für tolle Zeiten und Zuspruch in schwierigen Momenten. Neben den vielen wisssenschaftlichen und nicht-wissenschaftlichen Diskussion danke ich Carsten Richter für die Beantwortung aller meiner Fragen zu Python und Kramers-Kronig Rechnungen.

Influenced by all the non-native English speakers, the weekly English class was the most helpful occasion to improve my English. I thank Louise Kennedy for supporting me to get along with lots of tiny little details and major challenges in the English language by persistently explaining grammar and tweaking our texts in terms of cohesion and style. Mein Dank gilt auch der PIER Graduate School für das Angebot vieler Kurse sowie für die finanzielle Unterstützung zur Teilnahme an Konferenzen. In diesem Sinne, vielen Dank an Maren Arnold-Vargen, Stefanie Tepass, Mirko Siemssen und Gabriele Keidel.

Zu guter Letzt danke ich von Herzen meiner Familie, meinem Freund Björn Enders und allen langjährigen Freunden für ihr Vertrauen in mich und für die perfekte Mischung aus Unterstützung wann immer nötig und Laissez-faire wann immer möglich. Vielen lieben Dank Euch allen!

Eidesstattliche Versicherung – Declaration on oath

Hiermit erkläre ich an Eides statt, dass ich die vorliegende Dissertationsschrift selbst verfasst und keine anderen als die angegebenen Quellen und Hilfsmittel benutzt habe.

I hereby declare, on oath, that I have written the present dissertation by my own and have not used other than the acknowledged resources and aids.

Juliane Reinhardt
Hamburg, 31. Januar, 2017